TRIPLE OXYGEN ISOTOPES OF BIOMINERALS:

A NEW PROXY FOR RECONSTRUCTING PALEOARIDITY,

PALEOECOPHYSIOLOGY AND PALEO-CARBON-CYCLING

by
Huanting Hu

A dissertation submitted to Johns Hopkins University in conformity with the requirements for the degree of Doctor of Philosophy

Baltimore, Maryland
September 2016

ABSTRACT

Over the past two decades, it has become widely recognized that triple oxygen isotope anomalies ($\Delta'^{17}O$) in terrestrial materials have great significance in studying Earth surface processes. Of specific relevance to this dissertation, it has been shown that the $\Delta'^{17}O$ of water records environmental information related to aridity, and the $\Delta'^{17}O$ of atmospheric O_2 is related to stratospheric photochemistry, the partial pressure of atmospheric CO_2 (pCO_2), and global primary productivity (GPP). Vertebrates incorporate the $\Delta'^{17}O$ signal of input water (drinking water, free food water, etc.) and atmospheric O_2 into body water, and this signal is then preserved in the isotopic composition of biominerals. Hence, $\Delta'^{17}O$ of biominerals is an appealing tracer of paleoaridity and paleo-carbon-cycling. The major objective of this dissertation is to develop approaches to fully realize the potential of biomineral $\Delta'^{17}O$ in paleoclimate studies. To enable these studies, I contributed to the development of a new high-precision (±0.01‰, 1σ) method for $\Delta'^{17}O$ analysis of carbonates that allows subtle triple oxygen isotope variations to be resolved with unprecedented detail (Passey et al., 2014). In this dissertation, I develop a triple oxygen isotope mass balance body water model, examine the influence on animal body water $\Delta'^{17}O$ of numerous climatic, ecological, and isotopic variables, and evaluate the model against triple oxygen isotope data from modern and fossil animals. I then apply the analytical method to fossil dinosaurian eggshell of Jurassic and Cretaceous age, use the body water model to interpret the relationships between $\Delta'^{17}O$ of dinosaur body water and $\Delta'^{17}O$ of atmospheric O_2 [$\Delta'^{17}O(O_2)$], and reconstruct the $\Delta'^{17}O$ of paleo-atmospheric O_2. Cretaceous fossil samples indicate slightly lower or similar $\Delta'^{17}O(O_2)$ values relative to modern days, pointing to slightly higher pCO_2 or similar to slightly lower GPP. Late

Jurassic samples indicate anomalously low $\Delta'^{17}O$ values, pointing to pCO_2 several times higher than present (1490±780 ppm, when assuming present day GPP), reduced GPP, or a combination of both. In summary, this dissertation provides a fundamental triple oxygen isotope body water model for interpreting environmental and physiological influences, and a unique approach of using $\Delta'^{17}O$ to investigate pCO_2 and carbon cycling of the past.

Advisor:

Benjamin H. Passey, PhD, *Department of Earth and Planetary Sciences*

Second Reader:

Dimitri A. Sverjensky, PhD, *Department of Earth and Planetary Sciences*

ACKNOWLEDGEMENTS

I would like to thank my advisory committee: Ben Passey, Dimitri Sverjensky, Naomi Levin and John Ferry. First and foremost, Ben has been an incredible academic mentor, editor, and teacher over the past five years, helping me find my own way on academia. I admire Ben's spirit and passion for his research, his high standards on science, and his patience on teaching me from a "fool". He teaches me to pursue good sciences, with an aim of solving unknown scientific problems, and helps me grow from a girl who knows nothing about isotopes to a geochemist who can think independently. I can still remember the time when he first handed a drill to me in the lab. This moment starts my career as a scientist and shapes my dream of building my own lab in the future. I want to thank Naomi Levin, who is always so generous in helping me when I have questions or feel confused. I would also like to acknowledge Dimitri Sverjensky, who always encourages me with his gentle smile and welcomes me to work in his lab during the past three months. Lastly, I would like to thank John Ferry, who is my academic committee member, for his advice and guideline during review meetings.

In addition, my collaborators have also contributed a lot on this research. Thank Beverly Johnson, Shaena Montanari, Karen Chin, Xiaolin Wang, and Qiang Wang for providing samples, and Alberto Pérez-Huertaa for making EBSD measurements. I also want to acknowledge the financial support from the Earth and Planetary Sciences department of Johns Hopkins University. I thank the donors of the American Chemical Society, Petroleum Research Fund for partial support of this work.

To Sophie Lehmann, Fang Huang, Greg Henkes, Haoyuan Ji, Shuning Li, Dana Brenner, Jihua Hao, Sara Rivero, Saleh Satti, and all of my other fellow EPS graduate students, I am thankful for the friendships that we have forged over many academic headaches and fun times. I look forward to remaining lifelong colleagues. I want to especially thank Sophie Lehmann, who is my first American friend and my closest sisters in arms during my PhD life, and Fang Huang, who has been my bosom friend since college. I cannot thank the two of them enough for their support and understanding ranging from research and life.

Lastly, I thank family for their consistent support and patience for my doctoral education. My parents Dezhi Hu and Qingmei Yuan have offered continuous support and encouragement for my education, from elementary through graduate school. My fiancé Xiao Yan has always been so patient and thoughtful, especially when I am weak and depressed. It is definitely not easy for both of us to hold on to a long distance relationship for so many years. I feel grateful and blessed to have you as my life-long partner. I must also give my acknowledgements to my favorite band Mayday, for comforting me when I am downcast, for strengthening me when I am weak, and for guiding me when I am lost. Without their respect and support, I may have never been able to pursue my passion in this field.

TABLE OF CONTENTS

LIST OF TABLES

LIST OF FIGURES

CHAPTER 1: INTRODUCTION

The oxygen isotope compositions of atmospheric gases, meteoric waters, polar ice, biogenic minerals, and other natural materials record information about atmospheric chemistry, the hydrological cycle, past climates, and biogeochemical processes (Urey, 1952; Francey and Tans, 1987; Gat, 1996; Zachos et al., 2001; Kohn and Cerling, 2002). In addition, the oxygen isotope compositions of biominerals such as eggshell carbonates and tooth enamel apatite have been widely used for paleoclimate reconstructions, including reconstructing paleo-water composition, paleo-aridity, and paleo-temperature (Luz and Kolodny, 1985; Lécuyer et al., 1996; Picard et al., 1998; Wenzel et al., 2000; Dettman et al., 2001). All of these studies have focused on $^{18}O/^{16}O$, and largely or completely ignored variations in $^{17}O/^{16}O$. It was long believed that $^{17}O/^{16}O$ strictly follows a slope of ~ 0.52 relative to $^{18}O/^{16}O$ during mass dependent fractionations (MDF) at Earth surface temperatures, and hence little additional information would come from measuring $^{17}O/^{16}O$. Moreover, the lack of high precision analytical methods for measuring $^{17}O/^{16}O$ in CO_2 has served as a major roadblock to developing the study of $^{17}O/^{16}O$ in carbonates and biominerals.

Within the past two decades, the assumption of a fixed relationship between ^{17}O and ^{18}O has been conclusively shown to be incorrect following on the development of high precision methods for triple oxygen isotope analysis (Meijer and Li, 1998; Angert et al., 2004; Barkan and Luz, 2007; Rumble et al., 2007; Luz and Barkan, 2010; Levin et al., 2014; Pack and Herwartz, 2014; Passey et al., 2014), and following on refinement of theory (Matsuhisa et al., 1978; Young et al., 2002; Barkan and Luz, 2007; Cao and Liu, 2011). For background, the mass dependent relationship (MDF) can be represented as:

$\delta'^{17}O = \theta \times \delta'^{18}O$, where $\delta' = \ln(\delta + 1) = \ln(R_{sa}/R_{st})$, and R_{sa} and R_{st} refer to $^{x}O/^{16}O$ ratios of samples and standards, respectively (Hulston and Thode, 1965; Mook, 2000; Young et al., 2002). Variations in the fractionation exponent θ will cause anomalies in ^{17}O relative to a reference $^{17}O - ^{18}O$ line. Here we define the ^{17}O-anomalies as: $\Delta'^{17}O = \delta'^{17}O - \lambda_{ref} \times \delta'^{18}O$, in which we choose $\lambda_{ref} = 0.528$, the slope of global meteoric water line (Meijer and Li, 1998; Luz and Barkan, 2010) as reference in this study. (Note that θ and λ are mathematically equivalent, but that θ is generally used for simple processes, like fractionations between two phases, whereas λ is generally used for the regression $\delta'^{17}O$ vs. $\delta'^{18}O$ trend of numerous related samples.) Variations in θ values for different MDF processes may lead to variation in $\Delta'^{17}O$ values of oxygen bearing materials. Measureable $\Delta'^{17}O$ variations have been observed from various materials, such as seawater and meteoric waters (Luz and Barkan, 2010), leaf waters (Landais et al., 2006), snow and ice (Landais et al., 2012), and rocks and minerals (Levin et al., 2014; Pack and Herwartz, 2014; Passey et al., 2014). For hydrological cycle studies, $\Delta'^{17}O$ has been used to distinguish kinetic (non-equilibrium) fractionations. Theoretical and empirical studies indicate that kinetic fractionation reactions often have lower θ values than equilibrium fractionation reactions (Young et al., 2002; Angert et al., 2004; Landais et al., 2006; Barkan and Luz, 2007; Uemura et al., 2010; Cao and Liu, 2011). For instance, equilibrium fractionation between liquid water and water vapor follows a slope of $\theta_{equil} \approx 0.529$ (Barkan and Luz, 2005), while diffusion of water vapor follows a slope of $\theta_{diff} \approx 0.518$ (Barkan and Luz, 2007). Therefore, waters affected by evaporation should have lower $\Delta'^{17}O$ values than nonevaporated waters, and hence $\Delta'^{17}O$ is potentially a good tracer of hydrological and ecophysiological fluxes that involving evaporation.

In terms of the actual analysis of $\Delta'^{17}O$ in CO_2, carbonates, and biominerals, precise measurement has been impeded because the ^{17}O CO_2 isotopologue, $^{12}C^{17}O^{16}O$, has the same nominal mass as the ^{13}C isotopologue, $^{13}C^{16}O^{16}O$, and therefore cannot be uniquely resolved by conventional isotope-ratio mass spectrometers. Previous analytical methods for CO_2 have been limited in low precision (Brenninkmeijer and Röckmann, 1998; Assonov and Brenninkmeijer, 2001; Mahata et al., 2012), requiring excessively large samples (Hofmann and Pack, 2010), or in involving complex analytical procedures (Barkan and Luz, 2012). In our laboratory, we have developed a new method for analysis of CO_2 and carbonates, and have achieved a precision of $\Delta'^{17}O \sim 0.010‰$ (1σ) for analysis of 10^1-10^2 μmol quantities of CO_2 and carbonates (Passey et al., 2014). The efficient and relatively safe procedure consists of an acid digestion ($2H^+ + CO_3^{2-} \xrightarrow{100\%H_3PO_4,90°C} CO_2 + H_2O$), a reduction reaction ($CO_2 + 4H_2 \xrightarrow{Fe,560°C} CH_4 + 2H_2O$), and a fluorination reaction ($2H_2O + 4CoF_3 \xrightarrow{350°C} 4CoF_2 + O_2 + 4HF$). Finally, the product O_2 is appropriate for mass spectrometry analysis, as there are no interfering isobars. Compared to other methods, this method not only has high precision for $\Delta'^{17}O$, but also has a relatively small sample size requirement, and is rapid and fairly simple. Establishment of this method makes further applications of triple oxygen isotope research in carbonates possible.

The triple oxygen isotope composition of biominerals, such as eggshell carbonate and tooth enamel apatite, should primarily reflect the triple oxygen isotope compositions of their parent waters (body water). Body water isotopic compositions are closely related to relative humidity, animal physiology and diet, the isotopic compositions of drinking water (surface water) and atmospheric O_2, and many other factors. Atmospheric O_2 is an

isotopically unique oxygen source for animal body water, as it has significantly lower $\Delta'^{17}O$ values relative to other oxygen sources (Barkan and Luz, 2011; Young et al., 2014). The $\Delta'^{17}O$ signatures of atmospheric O_2 originating from the mass independent photochemical reactions in the stratosphere are modified by photosynthesis and respiration, and hence carry a signature of global primary productivity (GPP) and the partial pressure of CO_2 (pCO_2) (Yung et al., 1991; Luz et al., 1999; Bao et al., 2008; Cao and Bao, 2013; Young et al., 2014). Several $\Delta'^{17}O$ budget models of atmospheric O_2 have been built to predict the numerical relationship among $\Delta'^{17}O(O_2) - pCO_2 -$ GPP (Cao and Bao, 2013; Young et al., 2014). Meanwhile, atmospheric O_2 is incorporated into body water by respiration, represented by equations such as $CH_2O + O_2 \rightarrow CO_2 + H_2O$. This means that the oxygen isotope compositions of fossil biominerals record information of $\Delta'^{17}O$ of paleo-atmospheric O_2, and can be used to reconstruct partial pressure of CO_2 of the past (Pack et al., 2013; Gehler et al., 2016).

Although there are several mass balance models considering $^{18}O/^{16}O$ influxes and effluxes through the animal to understand the influences of climate and physiological factors on animal body water compositions (Luz and Kolodny, 1985; Bryant and Froelich, 1995; Kohn, 1996), information from $^{17}O/^{16}O$ is still crucial in order to better constrain environmental conditions and animal physiological characters, and to predict the relative proportion of atmospheric O_2 input to other oxygen sources. Pack et al. (2013) developed a triple oxygen isotope model based on the steady-state mass balance $^{18}O/^{16}O$ model of Bryant and Froelich (1995), which assumes that different oxygen fluxes scale with animal body mass. They used the mass-dependent scaling relationships to predict the relative proportions of atmospheric O_2 inputs, then calculated $\Delta'^{17}O(O_2)$ values of the past

from $\Delta'^{17}O$ data of fossil mammal samples, and hence reconstructed pCO_2 of the past. However, the scaling assumption commonly has poor predictive powder as it overlooks many specific physiological and taxon-level effects on animal water flux rate. The $^{18}O/^{16}O$ body water model of Kohn (1996) suggests that the oxygen influxes and effluxes of animal body water should be calculated by accounting for specific conditions, including diet, behavior, physiology, and environmental conditions. Especially for triple oxygen isotope studies, variations in body water $\Delta'^{17}O$ are not only caused by variations in $\Delta'^{17}O$ of atmospheric O_2, but also by $\Delta'^{17}O$ variations in meteoric waters and food waters (*e.g.*, leaf water and stem water) resulting from evaporation. Therefore, more accurate triple oxygen isotope body water models are essential in order to determine the influence of environmental and physiological effects on animal body water compositions, and to better interpret the degree of dilution of the atmospheric O_2 signal in total animal body water by other sources of oxygen.

In this thesis, I will first present a ^{17}O-enabled body water model based on the $^{18}O/^{16}O$ of Kohn's 1996 model (Chapter 2) for interpreting variations in body water triple oxygen isotope compositions to effects from diet, physiology and environmental conditions. I also explore the sensitivity of the model to climate and physiology variations, examine general predictions of the model with data from bird eggshells and mammal teeth, and present a case study of applying this model to climate and physiology studies. In Chapter 3, I present a triple oxygen isotope dataset of 71 dinosaurian eggshell carbonates ranging in age from Late Jurassic to Late Cretaceous. Then, I use the body water model of Chapter 2 to model the isotopic relationships between atmospheric O_2 and animal body water, and hence constrain the past $\Delta'^{17}O$ of atmospheric O_2. Finally, I infer

aspects of Mesozoic carbon cycling, including pCO_2 and GPP, using the reconstructed $\Delta'^{17}O$ of O_2 and the $\Delta'^{17}O$ budget model of Cao and Bao (2013). The combined outcome of these studies should lead to breakthroughs in using triple oxygen isotope for paleoclimate reconstructions, especially for paleo-carbon-cycling reconstructions.

CHAPTER 2:MODELING AND INTERPRETING TRIPLE OXYGEN ISOTOPE VARIATIONS IN ANIMAL BODY WATER

Abstract

The $^{18}O/^{16}O$ ratios of biominerals have been widely used for reconstructing ecophysiology and climatic settings of modern and extinct animals. However, the $^{18}O/^{16}O$ ratios of body water, which largely determine the $^{18}O/^{16}O$ ratios of biominerals, are influenced by a host of competing factors. Regional climate and local hydrology are dominant controls on water isotopic composition before water is consumed by an animal. Behaviorial and physiological factors, modified by local climate, also have a strong influence on body water compositions. The addition of a third isotope, ^{17}O (expressed as $\Delta'^{17}O$) potentially allows for further resolution of these factors. Here we construct a triple oxygen isotope mass balance body water model and examine the influence on animal body water $\Delta'^{17}O$ of numerous climatic, ecological, and isotopic variables. We evaluate the model against new and previously published triple oxygen isotope data from modern and fossil animals. The model predicts that animals from arid environments will have wider ranges and lower minimum values of body water $\Delta'^{17}O$ than animals living in humid environments. Leaf water consumers are more sensitive to variations in relative humidity and have lower $\Delta'^{17}O$ than surface water consumers, which more closely track meteoric water compositions. Factors such as body mass and relative proportions of evaporative versus nonevaporative effluxes from the animal have a lesser influence on animal $\Delta'^{17}O$. If $\delta'^{18}O$ of meteoric water is invariant, body water isotopic compositions will form approximately linear arrays in $\Delta'^{17}O$ versus $\delta'^{18}O$ space with slopes of ~0.52. Study of $\Delta'^{17}O$ becomes most useful when $\delta'^{18}O$ of meteoric water is variable or unknown

(as is generally the case for fossil animals); in this case $\delta'^{18}O$ of body water responds more strongly to changes in isotopic composition of meteoric water, whereas $\Delta'^{17}O$ of body water responds more strongly to changes in relative humidity and evaporated water inputs. These predictions are generally supported by observations of $\Delta'^{17}O$ for modern animals, and suggest that $\Delta'^{17}O$ analysis of animal tissues has great potential as a paleo-aridiy proxy in continental environments, as a proxy for learning about the water balance ecology of modern and extinct animals, and as a basis for reconstructing the $\Delta'^{17}O$ of ancient atmospheric O_2.

2.1. INTRODUCTION

The oxygen isotope composition of animal body water is closely related to animal physiology, diet, habitat, and climate (Longinelli, 1984; Luz et al., 1984; Luz and Kolodny, 1985; Levin et al., 2006; Daux et al., 2008; Chenery et al., 2010). Biominerals such as eggshell carbonate or tooth enamel bioapatite inherit their oxygen isotope compositions from animal body water. In aquatic invertebrates, $^{18}O/^{16}O$ compositions of biominerals depend mainly on their parent water compositions (continental surface waters or seawater) and mineralization temperature, and hence can be used for reconstructing both paleo-water compositions and paleo-temperature (Luz and Kolodny, 1985; Lécuyer et al., 1996; Picard et al., 1998; Wenzel et al., 2000). But for terrestrial vertebrate biominerals, $^{18}O/^{16}O$ compositions are strongly influenced by relative humidity, diet, isotopic composition of atmospheric O_2, and many other factors (Longinelli, 1984; Ayliffe and Chivas, 1990; Luz et al., 1990; Ayliffe et al., 1992; Fricke et al., 1998b; Levin et al., 2006; Clementz et al., 2008). Many terrestrial animals are endothermic or

otherwise maintain a narrow range of body temperatures, meaning that variation in $^{18}O/^{16}O$ ratios of biominerals largely reflects variation in $^{18}O/^{16}O$ ratios of body water.

In order to understand the influence on animal body water isotopes of climate, animal physiology and dietary selectivity, several mass balance models of oxygen isotope fluxes through the animal have been built (Luz and Kolodny, 1985; Luz et al., 1990; Bryant and Froelich, 1995; Kohn, 1996; Podlesak et al., 2008; Pack et al., 2013). However, with the exception of the pioneering study by Pack et al. (2013), these models consider only $^{18}O/^{16}O$ and not the third oxygen isotope, ^{17}O. Study of $^{17}O/^{16}O$ has been limited in part because of a belief that little additional information would come from $^{17}O/^{16}O$, as the three oxygen isotopes have been demonstrated to follow mass dependent fractionation (MDF) laws during isotope exchange processes, that is, fractionation in $^{17}O/^{16}O$ is approximately half of fractionation in $^{18}O/^{16}O$. In other words, there has been little motivation to measure $^{17}O/^{16}O$ because it was thought that its value could be predicted based on the much more easily measured ratio $^{18}O/^{16}O$. Moreover, high precision measurement of $^{17}O/^{16}O$ in carbon dioxide (as may be liberated from biogenic carbonates and bioapatites by phosphoric acid digestion) has only recently been realized (Barkan and Luz, 2012; Passey et al., 2014; Barkan et al., 2015; Mahata et al., 2016).

The assumption of a fixed relationship between $^{17}O/^{16}O$ and $^{18}O/^{16}O$ is only valid to the first order, and analytical precision is now sufficient to resolve subtle variations in the mass dependent relationship, that is, variations in the 2nd and 3rd decimal place in the fractionation exponent θ. (For a complete explanation of triple oxygen isotope nomenclature specifically used in this paper, we refer the reader to Section 1 of Passey et al., 2014, and references therein). The MDF law can be written as: $\alpha^{17}_{A\text{-}B} = \left(\alpha^{18}_{A\text{-}B}\right)^{\theta_{A\text{-}B}}$ (Mook

and Rozanski, 2000), where $\theta_{A\text{-}B}$ is the specific MDF exponent between phases A and B, approximately equal to 0.52 for physical and chemical processes at Earth surface temperatures (Matsuhisa et al., 1978; Clayton and Mayeda, 1996; Miller, 2002; Young et al., 2002; Rumble et al., 2007), and $\alpha^{x}_{A\text{-}B}$ is fractionation factor ($\alpha^{x}_{A\text{-}B} = {}^{x}R_{A} / {}^{x}R_{B}$) between phase A and phase B, where ${}^{x}R$ refers to isotopic ratios ${}^{x}O/{}^{16}O$ (x = 17 or 18). Oxygen isotope compositions in different materials are expressed in δ and δ'-notations: $\delta^{x}O = 10^{3}({}^{x}R_{sa} / {}^{x}R_{st} - 1)$ and $\delta'^{x}O = 10^{3} \ln({}^{x}R_{sa} / {}^{x}R_{st})$. Finally, we can calculate the deviation of ${}^{17}O/{}^{16}O$ from an expected relationship with ${}^{18}O/{}^{16}O$ as:

$$\Delta'^{17}O = \delta'^{17}O - \lambda_{ref} \times \delta'^{18}O \quad (1)$$

Here we use $\lambda_{ref} = 0.528$, the slope of the global meteoric water line (Meijer and Li, 1998; Luz and Barkan, 2010), and we follow the recommendation of Young et al. (2014) to include a 'prime' symbol after Δ to more clearly indicate that it is calculated from δ' ("delta-prime") values.

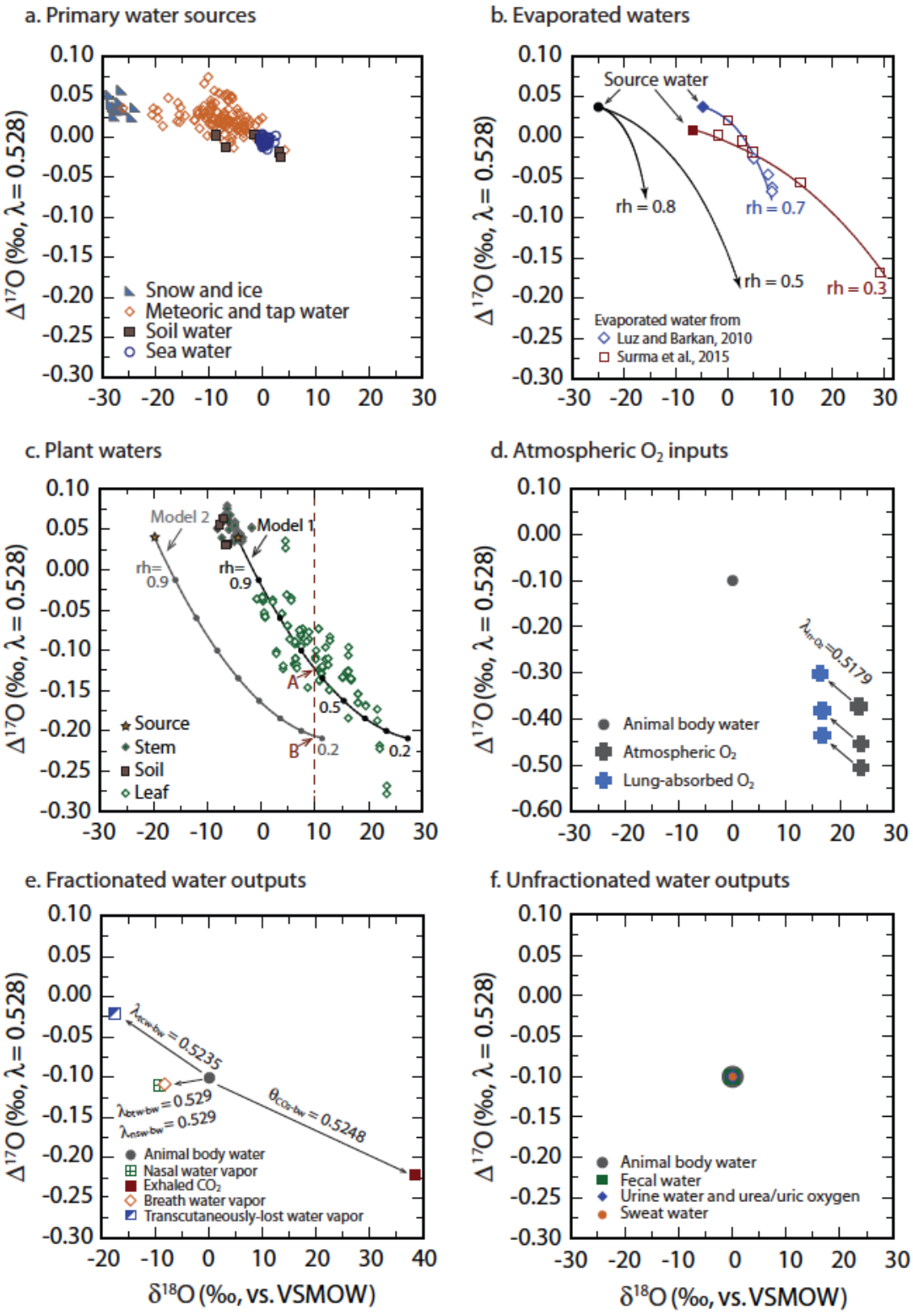

Figure 2-1. Measured, modeled and schematic triple oxygen isotope compositions of natural waters, evaporated waters, plant waters, atmospheric oxygen, animal body water and inputs and outputs for the

animal body water. Note that the axis scales are uniform except for Figure 2-1d and 2-1e. (a) Primary oxygen sources, including sea water (Luz and Barkan, 2010), meteoric water (Landais et al., 2010; Luz and Barkan, 2010) and tap water (Li et al., 2015), snow and ice (Landais et al., 2008; Landais et al., 2012a; Landais et al., 2012b; Steig et al., 2013; Schoenemann et al., 2014), and soil water reconstructed from soil carbonates (Passey et al., 2014). (b) Isotopic evolution of water bodies through simple pan evaporation. Filled diamond, square and circle are initial waters of different isotopic composition. The open diamonds show results for evaporation of water in a laboratory (Luz and Barkan, 2010); the open squares show trend of evaporation for Helmand River System waters (Surma et al., 2015). The solid lines show modeled evolution of evaporating waters with different initial compositions for evaporation under rh = 0.7 (blue line), rh = 0.3 (red line) and rh = 0.8 and 0.5 (black lines). The fractions of remaining initial water masses decrease from top to bottom. The models are based on equations 4.35a–c of Criss (1999), using fractionation factors reported in Friedman and O'Neil (1977), Barkan and Luz (2005), and Barkan and Luz (2007), and assuming that atmospheric water vapor is in isotopic equilibrium with waters of the initial isotopic composition. (c) Plant water compositions and leaf water models. Measured isotopic compositions of soil, stem and leaf waters are from Landais et al. (2006). We also modeled evolutions of leaf waters based on the $^{18}O/^{16}O$ leaf water model of Roden and Ehleringer (1999) and use the humidity related *l* values from Landais et al. (2006) to calculate the $\Delta'^{17}O$ values for leaf water. Model outputs with two different water sources (stars) are shown in two solid lines. Filled dots indicate relative humidity, which decreases from top to bottom. (d) Different measurements of atmospheric O_2 isotopic compositions (Barkan and Luz, 2005, 2011; Young et al., 2014) and calculated isotopic compositions of lung absorbed O_2. We use a fractionation exponent between lung absorbed O_2 and atmospheric O_2 is 0.5179 (Luz and Barkan, 2005) and a $^{18}O/^{16}O$ fractionation factor of 0.9930 (following Kohn, 1996). The filled circle is a schematic body water composition for comparison. (e) Fractionated oxygen effluxes of an animal. Isotopic compositions of all effluxes are calculated based on a schematic body water composition shown in grey filled circle. Fractionation exponents and factors are shown in detail in Table 2-4. (f) Unfractionated oxygen effluxes of an animal. Oxygen effluxes shown in this figure are unfractionated waters of body water, and hence have the same isotopic compositions as animal body water.

Because different fractionation processes have different θ values, oxygen isotope compositions may deviate from a single $\delta'^{17}O$ - $\delta'^{18}O$ reference line (*i.e.*, they may have variable $\Delta'^{17}O$ values). Of relevance to the global water cycle, including water in plants and animals, studies show that kinetic processes often have relatively low θ values [*e.g.*, θ_{diff} = 0.519 for diffusion of H_2O vapor through air; Barkan and Luz (2007), Young et al. (2002)], while equilibrium processes typically have higher θ values [*e.g.*, θ_{eq} = 0.529 for equilibrium fractionation between liquid and vapor water; Barkan and Luz (2005)]. At Earth surface temperatures, these θ values appear to be relatively insensitive to temperature change (*e.g.*, Cao and Liu (2011); Hofmann et al. (2012)).

Because of the differences in θ values between kinetic and equilibrium processes, $\Delta'^{17}O$ is potentially a good tracer of hydrological and ecophysiological fluxes involving evaporation (which has a strong kinetic component, especially at low relative humidity) versus those involving condensation and advection, such as dominates in Rayleigh distillation of atmospheric water masses (quasi-equilibrium condensation and advection), or in nonevaporating transfers of waters (advection). The slope of the triple oxygen isotope global meteoric water line (GMWL), λ_{ref} = 0.528, reflects this dominance of equilibrium processes (θ_{eq} = 0.529; see Luz and Barkan (2010) for a detailed explanation of how the slightly lower GMWL slope of 0.528 arises). Because the fractionation exponent for diffusion of water vapor through air is lower (θ_{diff} = 0.519) than the GMWL slope, waters affected by evaporation, although enriched in $^{17}O/^{16}O$, have a deficit in $^{17}O/^{16}O$ relative to $^{18}O/^{16}O$, and hence will have low $\Delta'^{17}O$ compared to nonevaporated waters.

Several studies have examined triple oxygen isotope compositions of natural waters, including polar snow and ice (Landais et al., 2008; Landais et al., 2012a; Landais et al., 2012b; Schoenemann et al., 2014), relatively unevaporated surface waters and tap waters (Luz and Barkan, 2010; Li et al., 2015), evaporated surface waters (Surma et al., 2015), and leaf waters (Landais et al., 2006). Figure 2-1a shows the triple oxygen isotope compositions of relatively unevaporated meteoric waters, while Figure 2-1b shows evaporated waters and Figure 2-1c shows measured and modeled leaf water compositions with two different source water compositions. With decreasing relative humidity, evaporated waters and leaf waters tend to have higher $\delta'^{18}O$ and lower $\Delta'^{17}O$ values. In Figure 2-1c, the points labeled A and B are schematic leaf waters with identical $\delta'^{18}O$ compositions, but from different environmental conditions and with different source water compositions. These two scenarios would be indistinguishable in studies measuring only $\delta'^{18}O$. By introducing $\Delta'^{17}O$, it becomes possible to gain additional aridity and source water information.

Atmospheric O_2 is a significant oxygen source to animal body water, and it carries a highly anomalous $\Delta'^{17}O$ value (Fig. 2-1d) related to mass dependent fractionation associated with the Dole effect (that is, the steady-state enrichment in heavy isotopologues of O_2 related to isotopic discrimination during respiration by Earth's biota; Dole, 1935; Young et al., 2002; 2014) and mass-independent fractionations (MIF) in the stratosphere. Note that all of the fractionation processes discussed above are mass dependent fractionations (MDF). In contrast, MIF is independent of the mass differences between isotopes, and can lead to large $\Delta'^{17}O$ values. These processes commonly follow a relationship of $\alpha^{17} \approx \alpha^{18}$ (Thiemens and Heidenreich, 1983; Thiemens et al., 1995). The

origin of mass-independent ^{17}O anomalies in the atmosphere is photochemical reactions among oxygen-bearing gases in the stratosphere, leading to an extremely ^{17}O-enriched O_3 and CO_2, and ^{17}O-depleted O_2. Following transport into the troposphere, the anomalous $\Delta'^{17}O$ of CO_2 and O_2 is sequestered to the hydrosphere by the action of photosynthesis and respiration. Hence the $\Delta'^{17}O$ of atmospheric CO_2 and O_2 is controlled by a 'tug of war' (Yung et al., 1991) between isotope anomaly production in the stratosphere and isotope anomaly sequestration to the hydrosphere (which contains vastly more O than the atmosphere and hence can be approximated as an infinite sink). As a consequence, the $\Delta'^{17}O$ of atmospheric CO_2 and O_2 carries a signature of gross primary productivity (GPP) and the atmospheric O_2/CO_2 ratio. (Yung et al., 1991; Luz et al., 1999; Bao et al., 2008; Cao and Bao, 2013; Young et al., 2014). Although there is some disagreement as to its exact isotopic composition, it is clear that tropospheric O_2 (Fig. 2-1d) is very low in $\Delta'^{17}O$ (Barkan and Luz, 2005, 2011; Young et al., 2014). Thus, O_2 and CO_2 are good tracers for studying stratospheric photochemical reactions and the global carbon cycle. Animals incorporate O_2 through oxidation of reduced carbon ($CH_2O + O_2 \rightarrow CO_2 + H_2O$) and thereby partly inherit the anomalous $\Delta'^{17}O$ signal of O_2. Therefore, biominerals forming in equilibrium with body water also track the isotopic composition of atmospheric O_2 and can be used to reconstruct $\Delta'^{17}O$ of ancient atmospheric O_2 (Pack et al., 2013).

Detailed and accurate triple oxygen isotope body water models are essential for determining the influence of environmental and physiological effects on animal body water compositions, and for determining the degree of dilution of the atmospheric O_2 signal in total animal body water by other sources of oxygen. Pack et al. (2013) developed a triple oxygen isotope model based on the steady-state mass balance $^{18}O/^{16}O$

model of Bryant and Froelich (1995), which assumes that different oxygen fluxes scale with animal body mass. For example, the model assumes that the relative proportion of 'drinking water' (that is, water ingested by drinking from streams, rivers, puddles, ponds, and lakes) scales directly with body mass, with larger animals consuming proportionally more drinking water than smaller animals. However, the body mass-dependent scaling relationships commonly have poor predictive power (*i.e.*, R^2 values are low for regressions between specific variables and body mass), and they overlook many specific physiological and taxon-level effects on animal water flux rate. Water flux rates vary between field and captive animals (Nagy, 1988), between juvenile and adult animals (Williams et al., 1993), and between desert-adapted animals and non-desert-adapted animals (Nagy, 2004), and cannot be precisely scaled by body mass. We describe an alternative ^{17}O-enabled body water model based on the steady-state mass balance $^{18}O/^{16}O$ body water model of Kohn (1996), which does not assign relative oxygen fluxes based on mass, but rather uses specific information about diet, behavior, physiology, and environmental conditions to calculate relative fluxes.

In this paper, we present the ^{17}O-enabled adaptation of Kohn's 1996 model, and then we explore the sensitivity of the model to parameter variation. We then examine general predictions of the model in the context of new and previously published data from bird eggshells and mammal teeth data. We present a case-study of recent Emu (*Dromaius*) based on modern eggshell samples collected from across Australia, and we conclude with a summary of the main findings of the present work.

2.2. MATERIALS AND METHODS

2.2.1. Materials

We assembled and analyzed a variety of modern bird eggshell and mammalian tooth enamel samples, including wild emu eggshell from Australia (×15), wild bird eggshell from Baltimore, USA (×7), and wild mammal tooth enamel from Kenya and Utah (×3). We combined isotopic data from these new samples with the modern eggshell and tooth enamel data reported in Passey et al. (2014). We also discuss briefly the tooth enamel data presented by Pack et al. (2013), which was generated using a different analytical method targeting the phosphate component of tooth enamel. Sample information is summarized in Table 2-1.

Table 2-1. Sample Information

Sample ID	Species/taxon/description	Location/Formation	Latitude	Longitude	Elevation	T (°C)[a]	Rh (%)[a]
Australian emu eggshell							
BC 608	Emu, *Dromaius*	Dulkanina, SA	29.0 S	138.5 E	29 m	13.7	50.3
BC 609	Emu, *Dromaius*	Roseberth, QLD	26.0 S	139.5 E	51 m	15.4	42.6
BC 611	Emu, *Dromaius*	Marion Downs, QLD	23.3 S	139.4 E	131 m	16.9	37.5
BC 612	Emu, *Dromaius*	Carpentaria Downs, QLD	18.5 S	144.2 E	474 m	19.4	54.2
BC 613	Emu, *Dromaius*	Millungera, QLD	20.0 S	141.5 E	96 m	20.3	39.7
BC 615	Emu, *Dromaius*	Millungera, QLD	20.0 S	141.5 E	96 m	20.3	39.7
BC 616	Emu, *Dromaius*	Olga Downs, QLD	20.5 S	143.2 E	209 m	18.8	44.0
BC 623	Emu, *Dromaius*	Wirrona, NSW	30.2 S	147.3 E	124 m	13.0	58.6
BC 628	Emu, *Dromaius*	Glenormiston, QLD	23.0 S	139.0 E	155 m	16.9	37.1
BC 629	Emu, *Dromaius*	North Simpson, VIC	38.5 S	143.2 E	159 m	10.0	74.8
BC 630	Emu, *Dromaius*	Wilpoorinna, SA	30.0 S	138.3 E	82 m	12.6	53.2
BC 894	Emu, *Dromaius*	Mildura, NSW	34.2 S	142.2 E	56 m	11.1	67.9
BC 975	Emu, *Dromaius*	Muloorina, SA	29.2 S	138.0 E	65 m	13.6	50.7
BC 977	Emu, *Dromaius*	Muloorina, SA	29.2 S	138.0 E	65 m	13.6	50.7
BC 1035	Emu, *Dromaius*	Cuddie Springs, NSW	31.0 S	146 E	220 m	11.7	58.5
Baltimore bird eggshell							
USABAL-Bird-2	Unknown; ~2 cm[b], white	Baltimore, USA	39.3 N	76.6 W	50 m	12.2	61.9
USABAL-Bird-3	Unknown; ~1 cm[b], light blue	Baltimore, USA	39.3 N	76.6 W	50 m	12.2	61.9
USABAL-Bird-4	Unknown; ~2 cm[b], teal	Baltimore, USA	39.3 N	76.6 W	50 m	12.2	61.9
USABAL-Bird-5	Unknown; ~1.5 cm[b], light blue	Baltimore, USA	39.3 N	76.6 W	50 m	12.2	61.9
USABAL-Bird-6	Unknown; ~1.5 cm[b], dark blue	Baltimore, USA	39.3 N	76.6 W	50 m	12.2	61.9
USABAL-Bird-7	Unknown; ~1.5 cm[b], white	Baltimore, USA	39.3 N	76.6 W	50 m	12.2	61.9
USABAL-Bird-8	Unknown; ~1.5 cm[b], grey	Baltimore, USA	39.3 N	76.6 W	50 m	12.2	61.9
Mammalian tooth enamel							
K00-TSV-113	Giraffe, *G. camelopardalis*	Tsavo West NP, Kenya	2.8 S	38.8 E	–	26.0	63.3
UT-deer	White tailed deer, *O. virginianus*	Parowan, UT, USA	37.8 E	113.0 W	1864 m	8.1	46.8
AIJB-B3-T4-DP4	Bison, *B. bison*	Antelope Island, UT, USA	40.9 E	112.2 W	1446 m	10.6	55.1

a. Climate data are from the CRU 2.0 gridded climate dataset (New et al., 2002). See Table A2.2 for more inforamtion For Australian localities, temperature (T) and relative humidity (Rh) values are averages for the coolest four months of the year, which is the typical egg-laying season for Emu. For Baltimore localities, T and Rh are averages for March through May, the spring egg-laying season during which these samples were collected. For the Utah and Kenya localities (mammal samples), we use mean annual averages of T and Rh, in light of the long duration of tooth enamel mineralization and hence time-averaging of isotopic signals.

b. Approximate minor-axis diameter of eggshell.

The Australian emu (*Dromaius novaehollandiae*) eggshells are from wild birds and were collected from localities across Australia with varying climate during breeding season (Table 2-1), and are a subset of the samples studied by Johnson et al. 1999). The Baltimore wild bird eggshells are opportunisitcally collected, recently hatched eggshells of unknown species. These eggshells vary in color and size as indicated in Table 2-1, and are suspected to be primarily pigeon (*Columbidae*), starling (*Sturnidae*), and robin (*Turdidae*). The mammalian tooth enamel samples are of white-tailed deer (*O. virginianus*) from Parowan, Utah, a bison (*B. bison*) from Antelope Island, Utah, USA, and a giraffe (*G. camelopardalis*) from Tsavo West National Park, Kenya.

2.2.2. Methods

We followed the triple oxygen isotope analytical methods described in Passey et al. (2014). Briefly, the analytical procedure involves phosphoric acid digestion of carbonate (or bioapatite) ($CaCO_3 + 2H^+ \rightarrow Ca^{++} + CO_2 + H_2O$, 90 °C), reduction of the purified CO_2 product by hydrogen over hot Fe catalyst ($CO_2 + 4H_2 \rightarrow CH_4 + 2H_2O$, 560 °C), fluorination of the purified H_2O product ($H_2O + 2CoF_3 \rightarrow 2CoF_2 + 2HF + 1/2\ O_2$, 360 °C), and analysis of the purified O_2 by extended-collection-time dual inlet mass spectrometry. Generally, ~7-9 mg of eggshell calcite ($CaCO_3$) or ~90-150 mg of tooth enamel apatite ($Ca_5(PO_4,CO_3)_3(OH,CO_3)$) is sufficient for one analysis. We report our $\delta^{17}O$, $\delta^{18}O$ and $\Delta'^{17}O$ values in ‰ (parts per thousand) relative to VSMOW2 ($\delta^{18}O \equiv 0$‰, $\delta^{17}O \equiv 0$‰) and SLAP2 ($\delta^{18}O \equiv -55.5$‰, $\delta^{17}O \equiv -29.6986490$‰) scale with a reference slope of $\lambda = 0.528$, using the recommendations in Schoenemann et al. (2013). Further

details of the data normailization scheme can be found in Appendix A of Passey et al. (2014).

During the course of the study we repeatedly analyzed the international standards NBS-18 and NBS-19, and in-house standards 102-GC-AZ01 (a groundwater carbonate) and Tank#2 CO_2 (gas drawn from a size K cylinder of research grade CO_2). From January 2014 to August 2015, we observed the following values for these materials (± values are 1σ): NBS-18, n = 13, $\delta'^{18}O = 15.1 \pm 0.4‰$, $\Delta'^{17}O = -0.103 \pm 0.013‰$; NBS-19, n = 16, $\delta'^{18}O = 36.3 \pm 0.5‰$, $\Delta'^{17}O = -0.143 \pm 0.009‰$; 102-GC-AZ01, n = 9, $\delta'^{18}O = 23.6 \pm 0.6‰$, $\Delta'^{17}O = -0.111 \pm 0.009‰$; Tank#2 CO_2, n = 18, $\delta'^{18}O = 31.5 \pm 0.4‰$, $\Delta'^{17}O = -0.119 \pm 0.009‰$. These values are statistically indistinguishable from values reported for the same materials in Passey et al., (2014), except for 102-GC-AZ01, which on average was 0.017‰ higher in $\Delta'^{17}O$ during the course of this study.

2.3. MODEL DESCRIPTION

The model is a triple oxygen isotope-enabled version of the Kohn (1996) animal body water $^{18}O/^{16}O$ model, which is a steady-state mass balance model. It is a general model applicable to terrestrial vertebrates, including birds, mammals, and reptiles. A principal feature of the model as conceived by Kohn (1996) and retained here is flexibility in accounting for a range of dietary and physiological adaptations of different species, and of behaviors and climatic contexts of individual animals. As explained in more detail below, the core of this approach is to calculate the total oxygen flux based on the energy requirement of the animal (calculated using a mass-based scaling relationship) and specified characteristics of the diet and physiology of the animal. An important

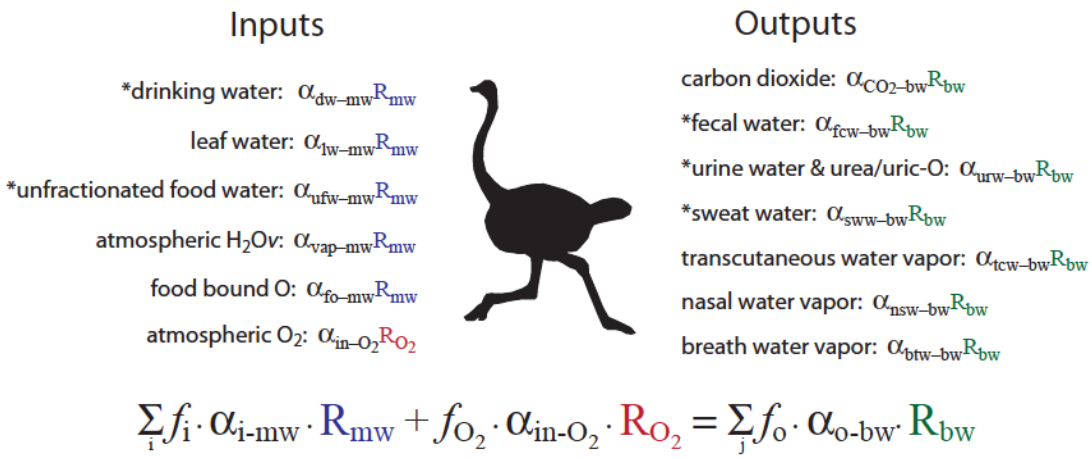

Figure 2-2. A schematic illustration of the triple oxygen isotope animal body water model. Oxygen output and input fluxes are in mass balance relationship following the equation shown in the bottom of the figure. Inputs can be expressed in terms of fractionations relative to meteoric water plus the term of absorbed atmospheric O_2. Outputs can be expressed in terms of fractionations relative to body water. Calculations of fraction (f) and fractionation factors (α) used in this equation are discussed in the text and given in Tables 2-3 and 2-4. Asterisks indicate nonfractionating fluxes ($\alpha = 1$).

parameter in this model is the water economy index (WEI, with units of ml H_2O per kJ), a measure of the water use per unit of metabolized energy (Nagy and Peterson, 1988; Nagy, 2004). The product of the total energy requirement and WEI determines the water requirement of the animal. If food-derived water, including free water in food and metabolic water, does not exceed this total water requirement, then the animal must drink surface waters to make up the deficit. If food-derived water equals or exceeds the total water requirement, the animal does not drink. The minimum WEI that a species is capable of achieving varies significantly and reflects behavioral and physiological adaptations for maintaining water and thermal balance, for example the urea-concentrating ability of the kidneys, ability to tolerate increases in body temperature

(adaptive heterothermy), and thermal load avoidance (shade-seeking, burrowing). However, the day-to-day WEI of a species may vary in response to environmental conditions, water content of food, availability of drinking water, reproductive status, and other factors. Figure 2-2 depicts the input and output fluxes considered by the model, and Table 2-2 lists the physiological, behavioral, and climatic parameters of the model that are chiefly used in calculation of input and output fluxes.

Table 2-2. List of model parameters, and values for the "standard model" based on Emu physiology and habitat. Listed parameter values are taken from Kohn (1996) if not otherwise specified.

Parameters	Values
Animal Specific Parameters	
Mass (kg)	40.000[a]
Metabolic pre-exponent (Met_pre_exp)	2.955
Metabolic exponent (Met_exp)	0.727
Oxygen conversion factor (mole/kJ)	2.16×10^{-3}
Water economy index (WEI, ml/kJ)	0.170[b]
Fecal H_2O content (fraction of total mass, $f_{H_2O\text{-in-fecal}}$)	0.600
Sweat/(sweat+pant) (fraction of total thermoregulatory water loss, $r_{s/p}$)	0.500
Fraction of O_2 used (fraction of inhaled O_2, $f_{used\text{-}O_2}$)	0.200
Z_value	10.500
Body Temperature (K)	311.150[a]
Environmental Parameters	
Relative humidity (rh)	0.500[c]
Environmental temperature (K)	288.150[c]
Meteoric water $\delta^{18}O$ ($\delta^{18}O_{mw}$, ‰)	-4.000[c]
Meteoric water $\Delta'^{17}O$ ($\Delta'^{17}O_{mw}$, ‰)	0.020[c]
Atmospheric O_2 $\delta^{18}O$ ($\delta^{18}O_{O_2}$, ‰)	23.881[d]
Atmospheric O_2 $\Delta'^{17}O$ ($\Delta'^{17}O_{O_2}$, ‰)	–0.506[d]
Food Parameters *(fractional)*	
Relative Digestibility (Digest)	0.700
Energy extraction efficiency (e_{extra})	0.900
Food carbohydrate content (f_{carb})	0.850
Food fat content (f_{fat})	0.050
Food protein content ($f_{protein}$)	0.100
Food associated free H_2O content ($f_{H_2O\text{-in-food}}$)	0.550[b]
Plant/(Plant+Meat) ratio	1.000
Ingested leaf/(stem+leaf) ratio relative to total ingested vegetation ($r_{l/s}$)	0.600

a. Emu mass is from Dawson et al. (1983). Female emu body temperature during breeding season is from Maloney and Dawson (1993).
b. Estimated based on ostrich WEI and typical food water content from Williams et al. (1993).
c. Typical environmental conditions and rainfall isotopic compositions in Australia during Emu breeding season (Liu et al., 2010; Li et al., 2015).
d. Average value for atmosphere samples collected in 2007, 2008, and 2009, reported by (Barkan and Luz, 2011).

This approach contrasts with that of the model of Bryant and Froelich (1995) and the triple oxygen isotope version of that model recently developed by Pack et al. (2013), which scale relative oxygen fluxes directly to body mass, and hence for a single body mass fix the ratio of nonmetabolic to metabolic oxygen fluxes (the latter of which carries the anomalous oxygen isotope signal of atmospheric O_2). Those models were consistent with early suggestions of generally negative correlations between body mass and animal $\delta^{18}O$, suggesting that smaller mammals have high relative fractions of metabolic oxygen, which is enriched in ^{18}O, while larger mammals have high relative fractions of drinking water, which is generally depleted in ^{18}O. This model is attractive for extension to extinct animals, whose dietary behaviors and physiologies are generally unknown but whose body masses can be estimated based on skeletal characteristics. A large amount of isotope data have been published in the past three decades, and it is well-demonstrated that there is significant variability of animal $\delta'^{18}O$ that is independent of body mass (*e.g.*, Ayliffe and Chivas, 1990; Luz et al., 1990; Fricke and O'Neil, 1996; Kohn, 1996; Fricke et al., 1998b; Levin et al., 2006), and this is further illustrated by data presented later in this paper. Body mass is a poor predictor of animal $\delta'^{18}O$ and the fraction of metabolic water, a finding consistent with poor correlations observed between WEI and body mass (Nagy and Peterson, 1988). Thus the main control of body water $\delta'^{18}O$ and $\Delta'^{17}O$ relative to meteoric water compositions is not body mass, but rather a set of factors related to WEI, consumption of evaporated water (primarily as leaf water), and the effect of relative humidity on evaporative isotopic enrichment of leaf water, surface water, and body water.

Aside from the incorporation of $^{17}O/^{16}O$ in our model, the primary departures from the Kohn (1996) model are: i. use of an updated leaf water oxygen isotope model (Roden and Ehleringer, 1999) and plant cellulose oxygen isotope model (Roden et al. 2000); ii. inclusion of a conditional statement so that drinking water flux cannot take on values below zero; and iii. casting the model in terms of isotope ratios R and fractionation factors α, which simplifies the adaptation to $^{17}O/^{16}O$ and reduces mathematical errors associated with using δ-values and 'big delta' values ($\Delta = \delta_1 - \delta_2$) in mass balance equations. Thus the overall isotopic mass balance equation is:

$$R_{bw}^{x/16} = \frac{R_{mw}^{x/16} \sum f_i \alpha_{i-mw}^{x/16} + f_{O_2} \alpha_{in-O_2}^{x/16} R_{O_2}^{x/16}}{\sum f_o \alpha_{o-bw}^{x/16}} \qquad (2)$$

Here x is either 17 or 18 (referring to ^{17}O and ^{18}O), R_{bw} is the isotope ratio of body water, R_{mw} is the isotope ratio of meteoric water, R_{O2} is the isotope ratio of atmospheric O_2, f_i are the incoming molar oxygen fluxes expressed as a fraction of the total incoming flux (including atmospheric oxygen, f_{O2}), f_o are the outgoing oxygen fluxes as a fraction of the total outgoing flux (note that this is a steady-state model where incoming flux = outgoing flux), $\alpha_{\text{i-mw}}$ are isotope fractionations of the incoming fluxes relative to meteoric water, $\alpha_{\text{in-O2}}$ is the fractionation of oxygen absorbed in the lungs relative to atmospheric O_2, and $\alpha_{\text{o-bw}}$ are the isotope fractionations of the outgoing fluxes relative to body water. For adaptation to $^{17}O/^{16}O$, the flux terms remain the same as for the $^{18}O/^{16}O$ model, $^{17/16}\alpha$ values are calculated based on $^{18/16}\alpha$ and triple oxygen isotope exponents θ or λ, $^{17/16}R_{mw}$ is calculated from $^{18/16}R_{mw}$ and $\Delta'^{17}O_{\text{mw}}$ (using appropriate relatioinships among R, δ, δ', and Δ) and $^{17/16}R_{\text{O2}}$ is calculated from $^{18/16}R_{O2}$ and $\Delta'^{17}O_{\text{O2}}$.

Table 2-3. Lists of output and input fluxes for animal body water, based on the "standard model" (see Table 2-2 for details about model parameters).

Total inputs/outputs budget			
Total Energy	$Energy_{Total} = 10^{Met\_pre\_exp} \times Mass^{Met\_exp}$ $= 10^{2.955} \times Mass^{0.727} = 1.3173 \times 10^4$ kJ	Energy from food per kg	$Energy_{food} = (f_{carb} \times 17.3 + f_{fat} \times 39.7 + f_{protein} \times 20.1) \times Digest \times e_{extra} \times 1000$ kJ/kg $= 1.1781 \times 10^4$ kJ/kg
Total dry food consumed	Food consumed = $Energy_{Total} / Energy_{food}$ = 1.1182 kg	Moles of O from food per kg	Food O = $f_{carb} \times 15.4 + f_{fat} \times 2 + f_{protein} \times 3$ = 13.4900 mole/kg
Free H_2O from food per kg	Food H_2O = Food consumed × 55.56 / $(1 - f_{H_2O\text{-in-food}}) \times f_{H_2O\text{-in-food}}$ = 75.9325 mole	Dry fecal output	Dry fecal = Food consumed × (1– Digest) = 0.3355 kg
Air flux through lungs	Air flux = $Energy_{Total}$ × Oxygen conversion factor × 22.4 (L/mole) / $f_{used\text{-}O_2}$ / 0.21 $= 1.5176 \times 10^4$ L	Total H_2O turnover	H_2O turnover = $m_{vap} + m_{lw} + m_{ufw}$ + metabolic water (when $m_{dw} < 0$), or = $Energy_{Total} \times WEI / 18$ (when $m_{dw} > 0$) Here, H_2O turnover = 124.4154 mole

Input	**Moles of oxygen**	**Fraction** [a]	**Output**	**Moles of oxygen**	**Fraction** [a]
Food bound O	m_{fo} = Food consumed × Food O × Digest × e_{extra}	$f_{fo} = 0.1062$	Fecal H_2O	m_{fcw} = Dry fecal / $(1 - f_{H_2O\text{-in-fecal}}) \times 55.56 \times (1 - f_{H_2O\text{-in-fecal}})$	$f_{fcw} = 0.1562$
Leaf water	m_{lw} = Food $H_2O \times r_{l/s}$	$f_{lw} = 0.2546$	Urea/uric O	$m_{uro} = 6 \times$ Food consumed $\times f_{protein} \times$ Digest $\times e_{extra}$	$f_{uro} = 0.0024$
Stem water	m_{ufw} = Food $H_2O \times (1 - r_{l/s})$	$f_{ufw} = 0.1697$	Nasal H_2O	$m_{nsw} = m_{total\text{-}breath}$ [e] $\times 0.5 \times 0.5$	$f_{nsw} = 0.0642$
Atmospheric O_2	$m_{in\text{-}O_2} = 2 \times Energy_{Total} \times$ Oxygen conversion factor	$f_{in\text{-}O_2} = 0.3180$	Transcutaneous H_2O	$m_{tcw} = 1.44 \times Mass^{2/3}$	$f_{tcw} = 0.0941$
Breath H_2O	m_{vap} = rh × saturation concentration of H_2O at environmental T [c] (mol/L) × Air flux (L)	$f_{vap} = 0.0307$	Breath H_2O	$m_{btw} = m_{heat\text{-}loss\text{-}H_2O}$ [f] $\times (1 - r_{s/p}) + m_{orally\text{-}loss\text{-}vapor}$	$f_{btw} = 0.1676$
Drinking water	m_{dw} = (Energy × WEI / 18) – $m_{vap} - m_{lw} - m_{ufw}$ – metabolic water [d] Notice: if the right side is less than 0, then m_{dw} = 0, which means this animal does not drink water	$f_{dw} = 0.1207$	Sweat H_2O	$m_{sww} = m_{heat\text{-}loss\text{-}H_2O} \times r_{s/p}$	$f_{sww} = 0.0393$
			Urine H_2O	$m_{urw} = 0.25 \times H_2O$ turnover	$f_{urw} = 0.1738$
			Exhaled CO_2	m_{CO_2} [g] = $m_{in\text{-}O_2}$ – Food (H_2-O) – $m_{uro} / 2$	$f_{CO_2} = 0.3023$
Total	$m_{t\text{-}in} = m_{fo} + m_{lw} + m_{ufw} + m_{in\text{-}O_2} + m_{vap} + m_{dw}$ = 178.9398 mole	1 [b]	Total	$m_{t\text{-}out} = m_{fcw} + m_{uro} + m_{sww} + m_{nsw} + m_{btw} + m_{tcw} + m_{urw} + m_{CO_2}$ = 178.9398 mole	1 [b]

[a] Fractions for each component are calculated through the equation of: $f_x = m_x/m_t$, where f_x is fraction for each component, m_x is moles of oxygen for each component, and m_t is either total moles of oxygen input or total moles of oxygen output.

[b] Sums of the exact fraction values from the model are both 1, whereas due to rounding the sums of the values listed in the table are not precisely 1.
[c] Saturation concentration of H_2O in air at ambient temperature = $10^{0.686 + 0.027 \times (T/\,^{\circ}C)}$ / (760 × 22.4) (mole/L), where T is body or environmental temperature.
[d] Metabolic water = amount of water produced from respiration, that is amount of food H_2 oxidized = Food consumed × Food H_2 × digestibility × e_{extra}, where Food $H_2 = f_{carb} \times 30.9 + f_{fat} \times 60 + f_{protein} \times 11$ (mole/kg). In this case, metabolic water = 21.3909 mole. Part of the oxygen in metabolic water is from bonded oxygen in food (Food O) and part is from atmospheric O_2.
[e] $m_{total\text{-}breath}$ = Total exhaled water vapor from breathing = Air flux × saturation concentration of H_2O at body T (see footnote c for equation). Assuming 50% of normally respired air is expelled orally ($m_{orally\text{-}loss\text{-}vapor} = 0.5 \times m_{total\text{-}breath}$) and 50% is expelled nasally.
[f] $m_{heat\text{-}loss\text{-}H2O}$ = amount of water used for heat loss = H_2O turnover – Fecal H_2O – Urine H_2O – Nasal H_2O – Transcutaneous H_2O – $m_{orally\text{-}loss\text{-}vapor}$.
[g] CO_2 output is approximately equal to air O_2 input, but corrected for urea or uric acid production and for air O_2 used for oxidizing food H_2 to produce part of the metabolic water. Food (H_2-O) = (Food H_2 – Food O) / 2.

Table 2-4. Fractionation factors and fractionation exponents used in the body water model

Parameter	Description / Comments	Values	Reference(s) / Notes
Fractionations associated with incoming fluxes			
$^{18/16}\alpha_{vap\text{-}mw}$	Fractionation factor between atmospheric water vapor and meteoric water	Eq. 1, footnotes	Majoube (1971); Friedman and O'Neil (1977)
$\theta_{vap\text{-}mw}$	Fractionation exponent between water vapor and liquid water	0.529	Barkan and Luz (2005)
$^{18/16}\alpha_{dw\text{-}mw}$	Fractionation factor between drinking water and meteoric water	1.000	Assuming animal drinking water has the same composition as meteoric water
$^{18/16}\alpha_{w\text{-}mw}$	Fractionation factor between leaf water and meteoric water. Function of relative humidity, temperature, and other factors.	Leaf water model	Roden and Ehleringer (1999)
$\lambda_{lw\text{-}mw}$	Fractionation exponent between leaf water and meteoric water	Eq. 2, footnotes	Landais et al. (2006)
$^{18/16}\alpha_{ufw\text{-}mw}$	Fractionation factor between unfractionated food water (e.g., stem water) and meteoric water	1.000	e.g., Yakir (1992)
$^{18/16}\alpha_{fo\text{-}mw}$	Fractionation factor between food-bound-O and meteoric water. Modeled as cellulose, assuming medium water is 50% leaf and 50% stem water.	Leaf water model	Roden and Ehleringer (1999) Roden et al. (2000)
$\lambda_{fo\text{-}mw}$	Fractionation exponent between cellulose and meteoric water	0.5275	Not yet determined; approximated by Pack et al. (2013)
$^{18/16}\alpha_{in\text{-}O2}$	Fractionation factor between lung-absorbed O_2 and atmospheric O_2	0.993	Kohn (1996); Epstein and Zeiri (1988)[a]
$\lambda_{in\text{-}O2}$	Fractionation exponent between lung-absorbed O_2 and atmospheric O_2	0.5179	Luz and Barkan (2005)

Table 2-4 (continued)

Parameter	Description / Comments	Values	Reference(s) / Notes
Fractionations associated with outgoing fluxes			
${}^{18/16}\alpha_{fcw\text{-}bw}$, ${}^{18/16}\alpha_{urw\text{-}bw}$, ${}^{18/16}\alpha_{uro\text{-}bw}$, ${}^{18/16}\alpha_{sww\text{-}bw}$	Fractionation factors between (fecal water[c], urinary water, urea/uric acid, sweat water) and body water	1.000	Kohn (1996); Schoeller et al. (1986)
${}^{18/16}\alpha_{nsw\text{-}bw}$	Fractionation between nasal water vapor and body water. Calculated for a temperature intermediate between body and environmental temperature.	Eq. 1, footnotes	Majoube (1971); Friedman and O'Neil (1977)
$\theta_{nsw\text{-}bw}$	Fractionation exponent between nasal water vapor and body water	0.529	Barkan and Luz (2005)
${}^{18/16}\alpha_{tcw\text{-}bw}$	Fractionation factor between transcutaneously-lost water vapor and body water	0.982	see Kohn (1996), pg 1484
$\lambda_{tcw\text{-}bw}$	Fractionation exponent between transcutaneously-lost water vapor and body water	0.5235	Not yet determined[c]
${}^{18/16}\alpha_{CO2\text{-}bw}$	Fractionation factor between exhaled carbon dioxide and body water	Eq. 3, footnotes	O'Neil and Adami (1969)
$\theta_{CO2\text{-}bw}$	Fractionation exponent between CO_2 and H_2O. Theoretical value at animal body temperature (~38 °C).	0.5248	Cao and Liu (2011)
${}^{18/16}\alpha_{btw\text{-}bw}$	Fractionation factor between breath water vapor and body water. Calculated for body temperature.	Eq. 1, footnotes	Majoube (1971); Friedman and O'Neil (1977)
$\theta_{btw\text{-}bw}$	Fractionation exponent between breath water vapor and body water	0.529	Barkan and Luz (2005)

a. Based on z-factor of 10.5‰ and oxygen utilization fraction of 0.2.

b. Oxygen bound in undigested food (fecal organic matter) is not considered by the model, under the assumption that this oxygen does not exchange significantly with body water (Kohn, 1996).

c. Estimate is intermediate between binary diffusion of water vapor through atmospheric gas (0.518) and equilibrium vapor – liquid fractionation (0.529).

Equation 1: $10^3\ln(\alpha_{liquid\text{-}vapor}) = 11.36 \times 10^5 / T^2 - 4.20 \times 10^2 / T - 2.07$. Equation 2: $\lambda_{lw\text{-}mw} = -0.0078 \times rh + 0.5216$; rh = relative humidity.

Equation 3: $10^3\ln(\alpha_{liquid\text{-}vapor}) = 16.60 \times 10^4 / T - 15.69$.

Table 2-3 provides an example of how the fluxes are calculated, and Table 2-4 lists the isotopic fractionation factors used in the model. The incoming fluxes are drinking water (f_{dw}), atmospheric oxygen (f_{O2}), free water in food [divided into unfractionated water such as stem and root water (f_{ufw}) and fractionated water such as leaf water (f_{lw})], oxygen bound in food (f_{fo}), and inhaled atmospheric water vapor (f_{vap}) (Fig. 2-2, Table 2-3). The outgoing fluxes are oxygen in fecal water, urine (urinary water, and O in urea / uric acid), and sweat water ($f_{fcw}, f_{urw}, f_{uro}, f_{sww}$), orally exhaled (breath) vapor (f_{btw}), nasally-exhaled vapor (f_{nsw}), transcutaneous water vapor (f_{tcw}), and exhaled carbon dioxide (f_{CO2}). The calculation of fluxes follows Kohn (1996). Briefly, the oxygen flux is set by the energy requirement of animal: this dictates how much food the animal must eat, which given food O content, food free water content, relative digestibility, WEI, and fraction of inhaled O_2 absorbed in the lungs sets the fluxes of food bound oxygen, food associated water (stem water + leaf water), drinking water, atmospheric O_2, and atmospheric water vapor. The outgoing CO_2 flux is based the energy requirement and the stoichiometry of respiration. Orally- and nasally- lost water vapor is based on the volume of air fluxed through the lungs to oxidize the amount of food specified by the energy requirement, and the remaining water is apportioned among fecal water, urinary water, sweat water, and oral water (e.g., panting) as specified by adjustable animal-specific parameters such as the ratio of sweating to panting, and fecal water contents (see Table 2-2). The reader is also referred to Kohn (1996) for the details and justification of how these fluxes are calculated.

Before turning to quantitative predictions of the model, it is useful to qualitatively-asses the effects of different variables based on visual inspection of the

inputs and outputs shown in Figure 2-1. Drinking water and stem water have the same $\delta'^{18}O$ and $\Delta'^{17}O$ values as unevaporated meteoric water (Fig 2-1a, 2-1c), so animals drinking large amounts of water or depending on root or stem water should have isotopic compositions more similar to meteoric water, unless the source water is evaporated (Fig. 2-1b). Leaf waters and atmospheric O_2 are more enriched in $\delta'^{18}O$ and depleted in $\Delta'^{17}O$ (Fig. 2-1c, 2-1d), which will lead to high $\delta'^{18}O$ and low $\Delta'^{17}O$ values in animal body water. Isotopic trends from oxygen effluxes are shown in Figure 2-1 e-f. Evaporated water vapor effluxes make body water more enriched in both of the heavy oxygen isotopes, ^{18}O and ^{17}O; this leads to higher body water $\delta'^{18}O$ values but slightly lower body water $\Delta'^{17}O$ values because the liquid-vapor fractionation exponent is slightly higher than the reference exponent (0.529 versus 0.528). Exhaled CO_2 is a distinctive output as it drives body water $\delta'^{18}O$ to be lower and $\Delta'^{17}O$ to be higher. This is because CO_2 is also more enriched in ^{18}O and ^{17}O than body water ($^{18/16}\alpha_{CO2\text{-}bw}$ = 1.0384 and $^{17/16}\alpha_{CO2\text{-}bw}$ = 1.0200 at 38 °C), but the fractionation exponent for CO_2-H_2O equilibrium is lower than that of the reference exponent (0.5248), which causes negative anomalies of $\Delta'^{17}O$ in CO_2 (and hence drives $\Delta'^{17}O$ to be more positive in the residual body water reservoir). Other unfractionated oxygen outputs, such as urine and fecal water, have the same isotopic compositions as body water (Fig. 2-1f).

2.4. MODEL SENSITIVITY

2.4.1. Standard model

In all, there are 52 parameters in the model, including ten animal-specific parameters, eight related to the diet of the animal, six climatic parameters, and fourteen

isotopic parameters, each featuring a $^{18}O/^{16}O$ and a $^{17}O/^{16}O$ fractionation factor. We evaluated model sensitivity by independently varying each parameter of the model, starting with a "standard model" loosely based on the physiology, diet and habitat of emu living in Australia, using the parameters specified in Tables 2-2 and 2-4. Emus feed primarily on plants, so we use model parameters from the herbivore model in Kohn (1996). In addition, we use emu specific values for mass and body temperature (Dawson et al., 1983; Maloney and Dawson, 1993), and estimate WEI and fraction of free water in food ($f_{H_2O\text{-in-food}}$) from its ratite relative ostrich (Williams et al., 1993). We use average environmental conditions of Australia for environmental parameters, especially for relative humidity and oxygen isotope compositions of precipitation. A standard $\delta^{18}O$ value of Australian precipitation is assigned as –4.0‰, estimated based on Bowen and Revenaugh (2003) and Liu et al. (2010). As $\Delta'^{17}O$ values of precipitation in Australia have not been studied, we choose a typical value of 0.020‰ based on global meteoric water $\Delta'^{17}O$ compositions (Li et al., 2015). The egg laying season for emu is the cool season (Coddington and Cockburn, 1995), and we assign a typical relative humidity value of 0.5, based on the CRU 2.0 dataset from New et al. (2002).

2.4.2. Results of sensitivity test

Table A2.1 presents the results for variation of all parameters in the model within realistic ranges of each parameter. Although there are more than 50 parameters, we observe that the model is only sensitive to a small subset of these. Many of the parameters are fixed or nearly so [*e.g.,* equilibrium fractionation factors between liquid and vapor, "fractionation factors" for unfractionated water influxes/effluxes ($\alpha = 1$)],

represent very small relative fluxes (atmospheric water vapor inhalation, transcutaneous water loss, O loss in urea / uric acid), or otherwise have very little influence on animal isotopic composition (*e.g.*, body mass, body temperature). Several other factors are essentially 'known' in the sense that they are assigned for specific environmental or behavioral conditions of interest (temperature, relative humidity, isotopic composition of meteoric water, variables related to dietary preference). In the discussion below, we will first discuss the dependence of animal body water on the isotopic composition of meteoric water, and then focus on a few parameters relating to plant water intake and isotopic composition that we identified as having outsize influence on body water isotopic composition. We also explore body mass as variable that we found to have relatively little influence on model results. In section 4.5, we further discuss leaf water as an amplifier of the modeled sensitivity to relative humidity, food water content, and water economy index. Finally, in section 4.6 we explore the influence of some important and less precisely known fractionation factors and fractionation exponents.

2.4.3. Dependence on meteoric water

Meteoric water sets the "starting point" of the model, as it is the source of surface water and plant waters, and hence directly determines isotope compositions of food, drinking water and air water vapor. Figure 2-3a and Figure 2-3c show that the slope of body water isotopes versus meteoric water isotopes is ~0.7 for both $\delta^{18}O$ and $\Delta'^{17}O$ (that is, about 7‰ change in $\delta^{18}O_{bw}$ per 10‰ change in $\delta^{18}O_{mw}$, and about 0.007‰ change in $\Delta'^{17}O_{bw}$ per 0.01‰ change in $\Delta'^{17}O_{mw}$). The curved line of $\Delta'^{17}O_{bw}$ versus $\delta^{18}O_{mw}$ in Figure 2-3b is a result of the nonlinear mixing effects between atmospheric O_2 inputs and

meteoric water input (and other inputs related to meteoric waters; see detailed explanation in Figure 2-4). The model predicts that $\delta^{18}O_{bw}$ and $\delta^{18}O_{mw}$ are closely related, as has long been appreciated and has been widely used in reconstructing paleoclimate (Fricke and O'Neil, 1996; Fricke et al., 1998a; Fricke and Wing, 2004; Gehler et al., 2012).

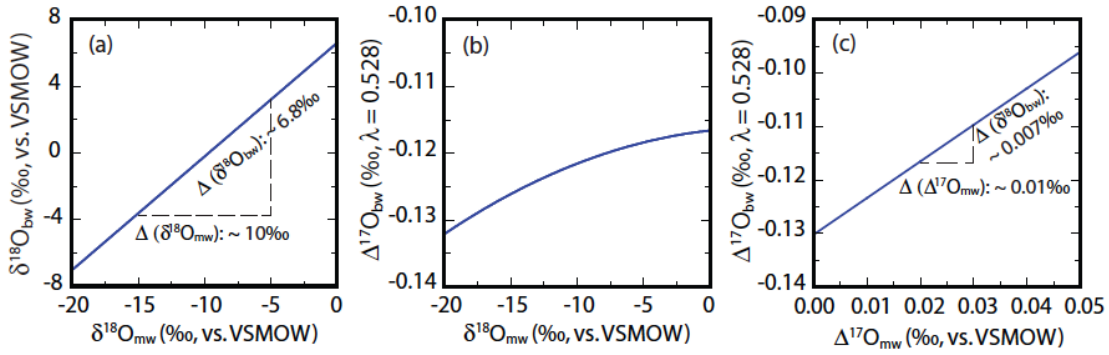

Figure 2-3. Dependence of animal body isotopic compositions water on meteoric water isotopic compositions. (a) Influence of $\delta^{18}O_{mw}$ on $\delta^{18}O_{bw}$. (b) Influence of $\delta^{18}O_{mw}$ on $\Delta'^{17}O_{bw}$. Changes in $\delta^{18}O_{mw}$ will cause small changes in $\Delta'^{17}O_{bw}$. The curved line is caused by mixing effects between meteoric water-related inputs and atmospheric O_2 inputs of animal body water (see Figure 2-4 for detailed explanation). (c) Influence of $\Delta'^{17}O_{mw}$ on $\Delta'^{17}O_{bw}$.

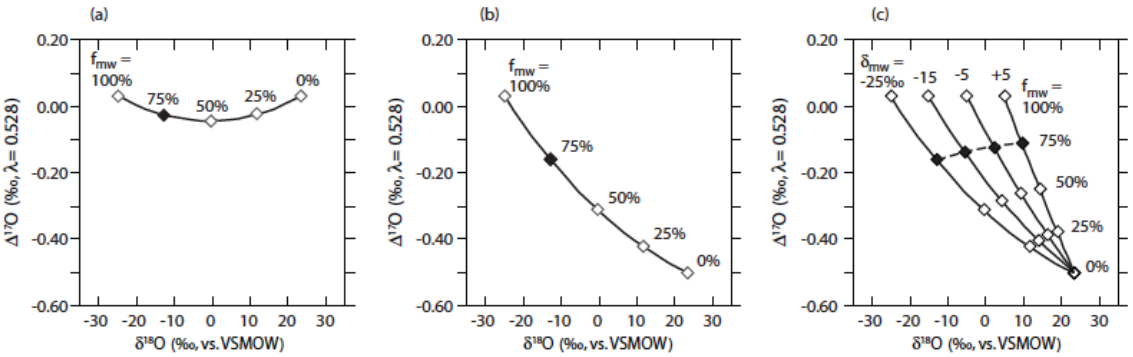

Figure 2-4. Illustration of how mixing effects lead to a dependency of $\Delta'^{17}O_{bw}$ on $\delta^{18}O_{mw}$, even when all other factors are held constant. (a) Simple mixing between two endmembers with constant $\Delta'^{17}O$ but differing $\delta^{18}O$. The diamonds show the relative proportions of the left-hand endmember (taken to represent meteoric water, mw). The filled diamond at 75% is highlighted to help track the mixing effect in subsequent panels. The curved mixing line and depression of $\Delta'^{17}O$ in intermediate mixtures is an artifact of the definition of $\Delta'^{17}O$, which being based on δ' values [that is, $\delta' = \ln(R_{sample}/R_{standard})$] is linear with respect to fractionation processes, but nonlinear with respect to mixing. (b) Same as (a), but now the right-hand endmember has a $\Delta'^{17}O$ value more reflective of atmospheric O_2. The curved mixing line is still apparent. (c) Same as (b), but now with additional left-hand endmembers representing a range of values representative of meteoric waters. Here it can be seen that lines connecting points with the same "mw" contributions are curved and concave-down (as illustrated for the 75% mw case), an effect that ultimately relates to the simple curved, concave-up mixing effect between endmembers.

2.4.4. Dependence on relative humidity, plant water, and thermophysiology

Beyond the isotopic composition of meteoric water, the model predicts that the following four parameters will be particularly important in determining animal body water isotopic composition (Table A2.1): relative humidity (rh), food free water content ($f_{H2O\text{-}in\text{-}food}$), leaf water ratio ($r_{l/s}$), and water economy index (WEI). These four parameters are key to the evaporated water intake of an animal: WEI helps to determine the amount of drinking water (which dilutes metabolic water and evaporated leaf waters),

$r_{l/s}$ and $f_{H2O\text{-}in\text{-}food}$ determine relative amounts of leaf water intake, and rh controls the degree of evaporative isotopic enrichment in leaf water. Evaporation and transpiration lead to enrichment of $\delta^{18}O$ and depletion of $\Delta'^{17}O$ in leaf waters, while stem and root water is not affected and is isotopically unfractionated relative to soil water (Yakir et al., 1990; Yakir, 1992; Yakir, 1998; Roden and Ehleringer, 1999; Helliker and Ehleringer, 2000; Landais et al., 2006). Landais et al. (2006) observed a dependence on rh of the triple oxygen isotope fractionation slope between leaf water and stem water, $\lambda_{trans} = 0.5216 - 0.0078 \times rh$. By combining the $^{18}O/^{16}O$ leaf water model from Roden and Ehleringer (1999) with this relationship for λ_{trans}, we can model the triple oxygen isotope composition of leaf water as a function of rh (*e.g.,* Figure 2-1c).

Figure 2-5a shows the model-predicted sensitivity of body water isotope composition to relative humidity. The predicted trends accord the trends in leaf water, that is, animals in low rh conditions have high $\delta^{18}O_{bw}$ and low $\Delta'^{17}O_{bw.}$ This prediction suggests the importance of leaf water inputs for animal body water. Therefore, high water content and high leaf fraction in food should also cause enrichment in $\delta^{18}O_{bw}$ and depletion in $\Delta'^{17}O_{bw}$ (Fig. 2-5b, 2-5c). Additionally, with higher water content in food, animals may be able maintain water balance only by eating and hence may not need to drink. The inflection points in Figure 2-5b reflect whether an animal needs to drink water or not. Drinking water is modeled as unevaporated meteoric water and hence a larger fraction of drinking water will dilute the evaporated signal from leaf waters and lead to lower $\delta^{18}O_{bw}$ and higher $\Delta'^{17}O_{bw}$ values. But if the water content in food is high enough, food water will in turn dilute the anomalously low $\Delta'^{17}O$ of metabolic water derived from atmospheric O_2. This is the explanation for the positive slopes in $\Delta'^{17}O_{bw}$ - $f_{H2O\text{-}in\text{-}food}$ and

$\Delta'^{17}O_{bw}$ - $\delta^{18}O_{bw}$ [Fig. 2-5 (b-2), (b-3)] under very high food water contents (that is, to the right of the inflection points).

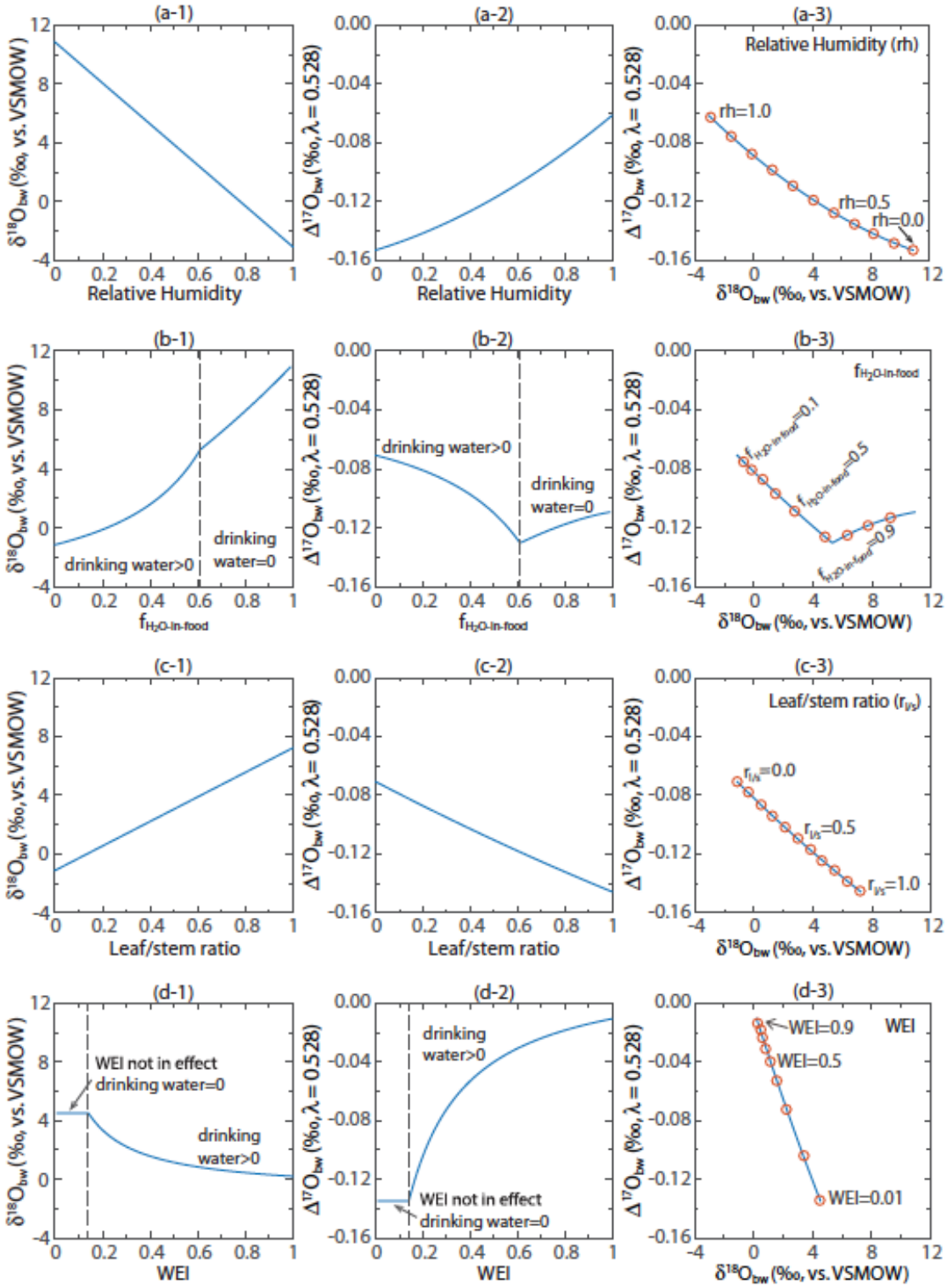

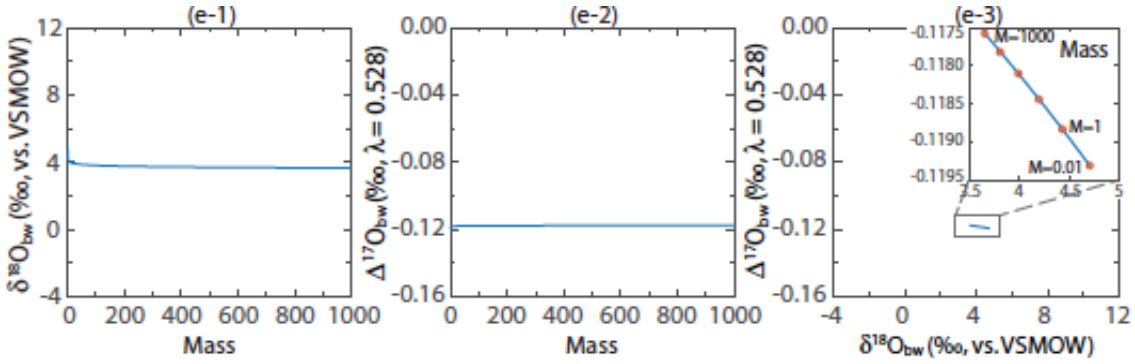

Figure 2-5. Effects of environment, diet and physiology on predicted $\delta^{18}O_{bw}$ and $\Delta'^{17}O_{bw}$, based on the standard emu model. Sub-figures in the left column show influences on $\delta^{18}O_{bw}$, in the middle column show influences on $\Delta'^{17}O_{bw}$, and in the right column with marked parameter values (open circles) show combined influences on $\delta^{18}O_{bw}$ and $\Delta'^{17}O_{bw}$. (a) Influence of relative humidity (rh); with decreasing rh, $\delta^{18}O_{bw}$ increases and $\Delta'^{17}O_{bw}$ decreases. (b) Influence of free water fraction in food (food water content). The inflection point relates to whether an animal needs to drink or not: to the left of this point (*i.e.,* lower food water content), the animal must drink to meet its water requirement. With higher food water content, $\delta^{18}O_{bw}$ increases and $\Delta'^{17}O_{bw}$ decreases. But at very high food water content (to the right of the inflection point), food water dilutes the low $\Delta'^{17}O$ contribution from atmospheric O_2, and hence $\Delta'^{17}O_{bw}$ increases. (c) Influence of leaf water fraction of total food water (leaf/ (leaf + stem) ratio). With increasing leaf water fraction, $\delta^{18}O_{bw}$ increases and $\Delta'^{17}O_{bw}$ decreases. (d) Influence of water economy index (WEI). The inflection point indicates whether WEI is in effect of determining animal total water turnover or not. When WEI is not in effect (to the left of the inflection) the animal does not need to drink. When WEI is in effect, $\delta^{18}O_{bw}$ decreases and $\Delta'^{17}O_{bw}$ increases with increasing WEI values. (e) Influence of body mass. Animal body mass has negligible effect on both $\delta^{18}O_{bw}$ and $\Delta'^{17}O_{bw}$, becuase in this model it has no effect on the isotopic compositions or relative amounts of different influxes and outfluxes, except for a minor influence on the magnitude of the transcutaneous water efflux.

Figure 2-5d shows the model-predicted influence of WEI on body water isotopic composition. An increase in WEI (= decrease in water use efficiency) generally leads to lower $\delta^{18}O_{bw}$ and higher $\Delta'^{17}O_{bw}$. In Figures 2-5 (d-1) and (d-2), the inflection points

represent the transition from no drinking water required (to the left of the inflections) to a finite drinking water requirement. We note here that desert-adapted animals commonly have lower WEI values than non-desert-adapted animals. Desert animals, especially eutherian mammals, may lower their water requirements through reduced metabolic rates, by limitng water losses in feces and urine, and by adjusting behavior (*e.g.*, "hiding" from the heat by seeking shade or entering burrows, by being less active during daytime and above ground). Such adaptations may allow the animal to be partially or completely independent of drinking water. If the animal does not drink, its water turnover amount will be determined only from dietary water and metabolic water, and hence the isotopically-evaporated inputs from leaf waters and negative $\Delta'^{17}O$ inputs from atmospheric O_2 are not diluted by drinking water. Therefore, deserted-adapted animals (low WEI) should have higher $\delta^{18}O_{bw}$ and lower $\Delta'^{17}O_{bw}$ values than non-desert-adapted (high WEI) animals.

Animal body mass is not in control of the relative proporations of O influxes and effluxes, except for minor relative changes in transcutaneous water efflux, and our model predicts that it has minor influence on both $\delta^{18}O_{bw}$ and $\Delta'^{17}O_{bw}$ (Fig. 2-5e). The slight enrichment in $\delta^{18}O_{bw}$ and depletion in $\Delta'^{17}O_{bw}$ with increasing body mass that our model predicts (Fig. 2-5e) is due to transcutaneous loss water vapor loss, the amount of which is calculated based on skin area and skin permeability of animal (Table 2-3), with skin area related to the cube of mass. In our model, body mass, metabolic pre-exponent and metabolic exponent determine the metabolic requirement of an animal (Table 2-3), but do not influence the fractions of each input and output component. Therefore, body mass

change has a negligible effect on animal body water compositions compared to animal diet, habit and ambient living environment.

Overall, our model predicts that animals living in arid environments (low rh), having high water use efficiency (low WEI), obtaining most water from food (high $f_{H_2O\text{-in-food}}$), and ingesting a relativly large fraction of leaves in food (high $r_{l/s}$), will tend to have high $\delta^{18}O_{bw}$ and low $\Delta'^{17}O_{bw}$ values. Animals with opposite behaviors and physiologies and living in humid environments will have low $\delta^{18}O_{bw}$ and lower $\Delta'^{17}O_{bw}$ values.

2.4.5. Leaf water effects

Leaf water is like an isotope amplifier that can magnify the effects from other parameters (Fig. 2-6): when the animal consumes leaf water, the model is very sensitive to those parameters, and when the animal does not consume leaf water, the model becomes relatively insensitive to those parameters. Leaf water itself is a good aridity proxy as its isotopic composition responds strongly to relative humidity. While leaf water carries evaporative isotopic signals, stem and root water are isotopically unfractionated relative to meteoric water. Animals consuming leaves acquire the evaporative signal, and inherit the isotopic effects of rh on leaf water. Thus, animals depending entirely on leaves but no stems ($r_{l/s} = 1$) are more sensitive to rh (Fig. 2-6a) compared to those depending entirely on stems and roots ($r_{l/s} = 0$). Figure 2-6b shows sensitivity tests of $f_{H_2O\text{-in-food}}$ for animals only eating leaves and those only eating stems and roots. As stem and root water affects body water compositions in a similar fashion as drinking water, the model predicts reverse trends for $r_{l/s} = 0$ and $r_{l/s} = 1$, when $f_{H_2O\text{-in-food}}$

increases. WEI indirectly controls the relative amount of leaf water an animal should ingest from food, and hence influences animal body water compositions differently for $r_{l/s} = 0$ and $r_{l/s} = 1$ (Fig. 2-6c). In general, leaf water input is a key factor in influencing animal body water compositions. Dietary differences of animals can lead to very different body water isotopic compositions. That is to say, even for animals from the same climate, their $\delta^{18}O_{bw}$ and $\Delta'^{17}O_{bw}$ can be very different because of different dietary preferences.

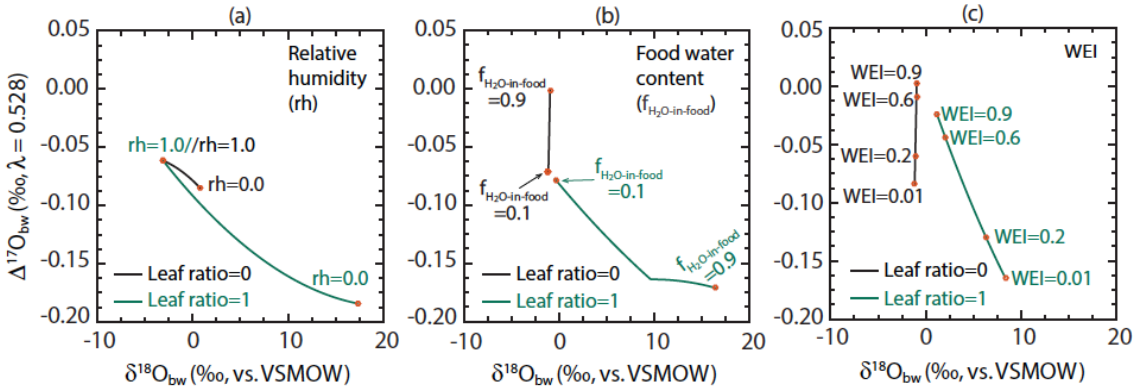

Figure 2-6. Leaf water amplification of other factors. We compare body water sensitivities to rh, food water content and WEI for model of leaf / (leaf + stem) ratio = 1, and with model of leaf / (leaf + stem) ratio = 0. Stem water is unfractionated meteoric water (note that root and tuber water is isotopically equivalent to stem water). But leaf water is evaporated, and this effect is enhanced in arid climates. (a) Relative humidity has a strong influence on animal body water compositions when animals eat only leaves, and a relatively weak influence when animals eat only stems. (b) Oxygen isotope compositions of animals that ingest leaf water are more sensitive to $f_{H_2O\text{-in-food}}$ change compared to those that ingest stem water. Because of the exceptional evaporative signals in leaf water, animals that eat leaves only will have higher $\delta^{18}O_{bw}$ and lower $\Delta'^{17}O_{bw}$, with increasing food water content. Stem water has same isotopic compositions as meteoric water. So body water compositions of animals that eat stems only move towards meteoric water compositions when food water content is increasing. (c) For the same WEI value, animals that eat only

leaves will have higher $\delta^{18}O_{bw}$ and lower $\Delta'^{17}O_{bw}$ compared to those that only eat stems. Also, animals only eat leaves are more sensitive to WEI change compared to those that only eat stems because leaf waters are more variable and have larger ranges in oxygen isotope compositions.

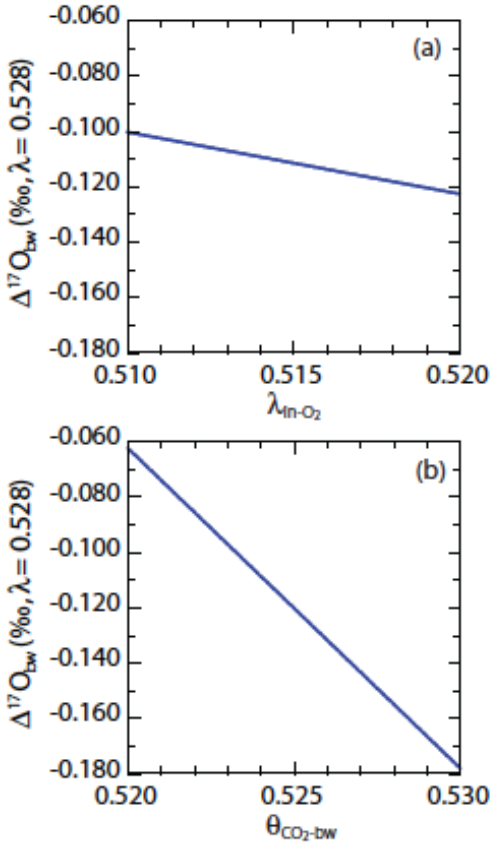

Figure 2-7. Influences of yet well-constrained fractionation exponents. Here we show the influences of fractionation exponents for (a) lung absorbed O_2 versus atmospheric O_2 ($\lambda_{in\text{-}O_2}$) and (b) exhaled CO_2 versus body water ($\theta_{CO_2\text{-}bw}$). The sensitivity is such that 0.01 changes in $\lambda_{in\text{-}O_2}$ and $\theta_{CO_2\text{-}bw}$ lead to ~0.01‰ and ~0.12‰ change in $\Delta'^{17}O_{bw}$. The latter is of great importance in model accuracy.

2.4.6. Sensitivities to fractionation factors

While many of the fractionation factors used in the model (Table 2-4) are well constrained (*e.g.*, $^{18/16}\alpha_{vap\text{-}mw}$, $^{18/16}\alpha_{CO2\text{-}bw}$), there are also some poorly constrained

fractionation factors and fractionation exponents. Figure 2-7 shows the sensitivity of $\Delta'^{17}O_{bw}$ to $\lambda_{in\text{-}O2}$ and $\theta_{CO2\text{-}bw}$. $\Delta'^{17}O_{bw}$ is more sensitive to $\theta_{CO2\text{-}bw}$ change than to $\lambda_{in\text{-}O2}$ because the intrinsic isotopic fractionation is much larger (~38‰ for $^{18/16}\alpha_{CO2\text{-}bw}$ versus ~7‰ for $^{18/16}\alpha_{in\text{-}O2}$). For a range in $\theta_{CO2\text{-}bw}$ from 0.52 to 0.53, $\Delta'^{17}O_{bw}$ decreases ~0.12‰, meaning that the model is almost as sensitive to $\theta_{CO2\text{-}bw}$ as to WEI. In our model, we use $\theta_{CO2\text{-}bw}$ = 0.5248 based on theoretical calculations in Cao and Liu (2011), a value that is similar to forthcoming results from our own laboratory. Barkan and Luz (2012) reported a value of $\theta_{CO2\text{-}bw}$ = 0.5229, and use of this value would shift $\Delta'^{17}O_{bw}$ by ca. +0.03‰ relative to model predictions using our preferred value of 0.5248. These uncertainties are not insignificant, and hence more studies on these less precisely known fractionation processes are needed.

2.5. MODEL-DATA COMPARISON

Measured triple oxygen isotope compositions of carbonates and the calculated parent water values are reported in Table 2-5 and shown in Figure 2-8. Table 2-5 and Table A2.3 gives the entire dataset that we consider in this paper, including new data reported here, and biomineral data that have already been reported in Pack et al. (2013) and Passey et al. (2014). For comparison to the body water model predictions, we focus on the calculated body water isotopic compositions rather than the measured compositions of the mineral samples. The methods and fractionation factors used to calculate of body water isotopic compositions from biomineral isotopic compositions are described in Passey et al. (2014).

Table 2-5. Measured isotopic compositions of eggshell and tooth enamel samples, and calculated compositions of parent waters of these samples. Values are given in units of per mil (‰) relative to the VSMOW-SLAP scale of Schoenemann et al. (2013), with $\lambda = 0.528$.

Sample ID	Species	N[a]	Measured values				Body T[d]	$^{18}\alpha$[e]	Calculated values			
			$\delta^{18}O_c$[b]	±[c]	$\Delta'^{17}O_c$[b]	±[c]	°C	($CaCO_3$–H_2O)	$\delta^{18}O_w$[b]	±[f]	$\Delta'^{17}O_w$[b,g]	±[f]
Australian emu eggshell												
BC 608	Emu	2	44.138	0.4	–0.197	0.011	38	1.0380	5.958	1.2	–0.068	0.017
BC 609	Emu	1	34.508	–	–0.157	–	38	1.0380	–3.320	1.5	–0.029	0.022
BC 611	Emu	2	35.885	0.1	–0.152	0.003	38	1.0380	–1.994	1.2	–0.023	0.017
BC 612	Emu	2	43.367	0.7	–0.183	0.001	38	1.0380	5.215	1.2	–0.054	0.017
BC 613	Emu	2	44.643	1.0	–0.222	0.003	38	1.0380	6.445	1.2	–0.093	0.017
BC 615	Emu	2	44.708	0.3	–0.230	0.003	38	1.0380	6.507	1.2	–0.101	0.017
BC 616	Emu	1	46.112	–	–0.230	–	38	1.0380	7.860	1.5	–0.101	0.022
BC 623	Emu	1	46.158	–	–0.201	–	38	1.0380	7.904	1.5	–0.072	0.022
BC 628	Emu	2	45.507	0.3	–0.203	0.009	38	1.0380	7.277	1.2	–0.075	0.017
BC 629	Emu	1	52.508	–	–0.226	–	38	1.0380	14.022	1.5	–0.097	0.022
BC 630	Emu	2	41.678	0.2	–0.160	0.005	38	1.0380	3.588	1.2	–0.031	0.017
BC 894	Emu	2	42.941	0.8	–0.203	0.003	38	1.0380	4.805	1.2	–0.074	0.017
BC 975	Emu	2	51.302	0.3	–0.233	0.006	38	1.0380	12.859	1.2	–0.104	0.017
BC 977	Emu	1	36.945	–	–0.177	–	38	1.0380	–0.972	1.5	–0.048	0.022
BC 1035	Emu	1	43.064	–	–0.171	–	38	1.0380	4.923	1.5	–0.042	0.022
Baltimore wild bird eggshell												
USABAL-Bird-2	Unknown	2	35.238	0.9	–0.172	0.003	39	1.0380	–2.617	1.2	–0.043	0.017
USABAL-Bird-3	Unknown	2	34.459	0.9	–0.150	0.001	39	1.0380	–3.367	1.2	–0.021	0.017
USABAL-Bird-4	Unknown	1	36.355	–	–0.174	–	39	1.0380	–1.541	1.5	–0.045	0.022
USABAL-Bird-5	Unknown	1	34.125	–	–0.161	–	39	1.0380	–3.689	1.5	–0.032	0.022
USABAL-Bird-6	Unknown	2	36.135	0.8	–0.167	0.001	39	1.0380	–1.752	1.2	–0.038	0.017
USABAL-Bird-7	Unknown	2	35.819	1.0	–0.204	0.016	39	1.0380	–2.057	1.2	–0.075	0.017
USABAL-Bird-8	Unknown	2	33.461	0.1	–0.190	0.006	39	1.0380	–4.329	1.2	–0.061	0.017
Mammalian tooth enamel												
K00-TSV-113	Giraffe	2	47.195	0.1	–0.236	0.003	38	1.0332	13.545	1.2	–0.122	0.016
UT-deer	Deer	2	35.129	0.0	–0.255	0.012	38	1.0332	1.867	1.2	–0.142	0.016
AIJB-B3-T4-DP4	Bison	2	31.526	1.3	–0.177	0.003	38	1.0332	–1.621	1.2	–0.064	0.016

a. Number of analyses, where each analysis involves acid digestion of carbonate to produce CO_2, reduction of CO_2 by H_2 to produce H_2O, fluorination of H_2O to produce O_2, and analysis of the gas on a Thermo MAT 253 mass spectrometer, as described in Section 2.2.
b. $\delta^{18}O_c$ and $\Delta^{17}O_c$ are isotopic compositions of O_2 generated from carbonates samples; $\delta^{18}O_w$ and $\Delta^{17}O_w$ are calculated parent water oxygen isotope compositions.

c. Values are the absolute difference between pairs of analyses.
d. Emu body temperature is from Maloney and Dawson (1993); other body temperatures are generic estimates.
e. Fractionation factor for eggshell carbonates is 1.0380, a combined mineral-water and acid digestion fractionation as determined by (Passey et al., 2014). For tooth enamel apatite, we multiply the mineral-water fractionation factor in Lécuyer et al. (2010) by 1.0079, which is the acid fractionation factor calculated for 90 °C phosphoric acid digestions of tooth enamel reported in Passey et al. (2007).
f. Values are based on standard error propagation using the 95% confidence intervals error reported in Passey et al. (2014) for ${}^{18}\alpha_{CaCO_3-H_2O} = 1.0380 \pm 0.0008$ and $\lambda_{CaCO_3-H_2O} = 0.5245 \pm 0.0003$. Average external precision for $\delta^{18}O_c$ and $\Delta'^{17}O_c$ measurements are 0.7‰ (1σ) and 0.01‰ (1σ) (Passey et al., 2014). Then, errors used in the propagations are 1.96 × S.E.M, where S.E.M. are generic errors. S.E.M. = average external precision/$\sqrt{N}$ (N is number of analyses).
g. Calculated using $\Delta'^{17}O_w = \Delta'^{17}O_c + 10^3 \ln {}^{18}\alpha_{CaCO_3-H_2O} \times (0.528 - \lambda_{CaCO_3-H_2O})$, where $\lambda_{CaCO_3-H_2O}$ is 0.5245 for all samples.

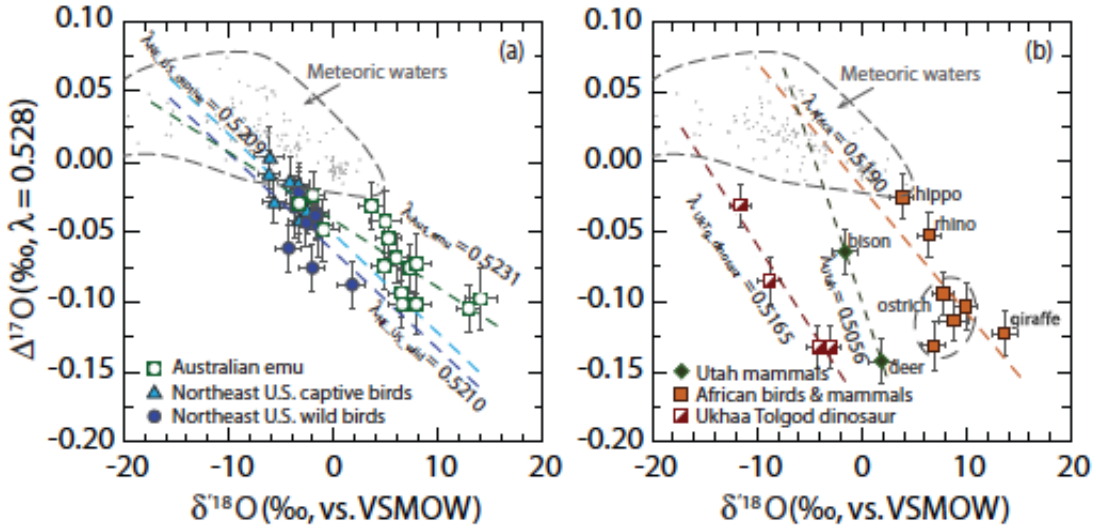

Figure 2-8. Measured body water compositions. (a) Captive birds and wild birds from northeast U.S. and Australian emu. (b) Mammals from Utah, ostrich and mammals from Africa, and late Cretaceous dinosaurs (oviraptorid) from Ukhaa Tolgod, Mongolia. Grey dashed curves bracket the range of meteoric waters (small grey dots). Body water is lower in $\Delta'^{17}O_{bw}$ than meteoric waters. Modern and fossil animals from each location plot in linear arrays with slopes of ~0.52 (dashed lines). λ values are regression slopes of $\delta'^{17}O_{bw} - \delta'^{18}O_{bw}$.

2.5.1. General observations and comparisons to data

The body water model makes several predictions about body water isotopic composition that are generally supported by data. Perhaps the most basic prediction of the model is that animal body water is almost always lower in $\Delta'^{17}O$ than local meteoric waters. This is because all of the inputs into the animal are either the same in $\Delta'^{17}O$ as meteoric waters (*e.g.,* drinking water, stem water), or lower in $\Delta'^{17}O$ (atmospheric O_2, evaporated waters including leaf waters, food-bound O, atmospheric water vapor). The only significant factor that can work to elevate animal body water $\Delta'^{17}O$ is the exhaled CO_2 flux, but this flux is generally not large enough relative to other fluxes to result in an

overall elevation of body water $\Delta'^{17}O$. The data shown in Figure 2-8 support these general predictions. Only a small fraction of samples overlap with the meteoric water range, and these are at the lower end of the range. The samples that overlap most are the captive birds in the northeast U.S., and the hippopotamus sample from Kenya (Fig. 2-8b). Presumably these captive birds were fed dry feeds and not fresh, green vegetation, and so they did not have the evaporative water influxes from leaf waters (low in $\Delta'^{17}O$). The highest $\Delta'^{17}O_{bw}$ value we observed in these captive birds is 0.004‰ (USA2013-NJemu-001), which is still lower than the average meteoric water $\Delta'^{17}O$ of northeast U.S., ~0.02‰ (Li et al., 2015). The wild hippopotamus from Kenya presumably had access to fresh green vegetation, at least seasonally, but being a semi-aquatic animal, its water balance was apparently dominated by meteoric waters.

Another basic prediction of the model is that populations of animals from the same geographic area should have isotopic compositions that plot along approximately linear arrays in $\Delta'^{17}O$ versus $\delta'^{18}O$ space, with slopes (= λ values) of ca. 0.52. The reason for this is that the evaporation trajectory in evaporation of standing water and leaf waters is approximately 0.52, as is the slope of a line joining typical meteoric waters and atmospheric O_2. λ values in Figure 2-8 represent regression slopes of $\delta'^{17}O_{bw} - \delta'^{18}O_{bw}$ for each group of samples, and range between 0.505 and 0.523. We note that this negative correlation of $\Delta'^{17}O_{bw}$ and $\delta'^{18}O_{bw}$ may not be very obvious when $\delta'^{18}O_{mw}$ is highly variable, like in seasonal climates. In this case, arrays for these animals may be dispersed along the $\delta'^{18}O$ axis, creating a parallelogram-like distribution. Additionally, if animals do not consume significant leaf water, like the captive birds in Figures 2-8a and 2-8b, a negative correlation between $\Delta'^{17}O_{bw}$ and $\delta'^{18}O_{bw}$ may not be apparent, and if there was

significant seasonal variability in $\delta'^{18}O_{mw}$ we would expect arrays of data to have a slope near 0.528, the slope of the meteoric water line. Other slopes are possible in under-sampled data sets. For example, if local animals have scattered body water compositions, but we only sampled those high in $\Delta'^{17}O_{bw}$ and $\delta'^{18}O_{bw}$, and those low in $\Delta'^{17}O_{bw}$ and $\delta'^{18}O_{bw}$, a positive regression trend will be achieved (i.e., $\lambda > 0.528$). Local trends will be most robust when multiple taxa and multiple individuals are studied. We note here that negative correlations between $\Delta'^{17}O_{bw}$ and $\delta'^{18}O_{bw}$ are not apparent in the dataset of Pack et al. (2013); these data show large variaion in $\Delta'^{17}O_{bw}$ with correspondingly little variation in $\delta'^{18}O_{bw}$, such that the overall array is 'vertical' in a plot of $\Delta'^{17}O_{bw}$ and $\delta'^{18}O_{bw}$, even when restricting the dataset to only the samples from Germany (the most well-sampled region in that study). At present it is not clear whether this pattern is representative of actual isotopic compositions of north-central European animals, is an artifact of undersampling, is related to the differing analytical methods used by Pack et al. (2013), or is related to some other unknown factors.

Another important prediction of the model, discussed extensively in Section 4, is that water-independent, leaf-consuming animals should have lower $\Delta'^{17}O_{bw}$ than water-dependent, non-leaf consuming animals. In Figure 2-8b, it can be seen that the leaf consumers (giraffe, ostrich and deer) have much lower $\Delta'^{17}O_{bw}$ than animals from the same locations that drink more water and do not depend as much on leaf water, such as hippo, rhino and bison. Similar trends, presumably related to physiology and dietary differences, are also observed between captive and wild birds in northeast U.S., and among the late Cretaceous fossil dinosaur samples from Nemegt Basin, Mongolia.

2.5.2. Relationship to relative humidity

Figure 2-5 and the related text showed how relative humidity has the effect of amplifying the evaporative lowering of $\Delta'^{17}O$ in leaf waters and consequently in animals consuming leaf waters. Thus the model predicts that the range in $\Delta'^{17}O_{bw}$ for a population of animals increases with decreasing rh. Here we explore the extreme lower and upper limits of $\Delta'^{17}O_{bw}$ by developing a "maximum evaporation body water model" (MAX-EVAP) and a "minimum evaporation body water model" (MIN-EVAP), respectively. The lowest modern animal $\Delta'^{17}O_{bw}$ values (MAX-EVAP) are expected from animals that live in arid climates, consume a large amount of leaf water, and have low WEI values (high water use efficiency). Conversely, the highest modern animal $\Delta'^{17}O_{bw}$ values (MIN-EVAP) are expected from animals that live in humid climates, consume little leaf water, and have high WEI values (poor water use efficiency). In the MAX-EVAP model, we use a WEI value of 0.05 mL/KJ, $\Delta'^{17}O$ of meteoric water of 0.010‰, food associated water content ($f_{H_2O\text{-in-food}}$) of 0.7, and a leaf/stem ratio ($r_{l/s}$) of 0.9. Similarly, we model the limits for the MIN-EVAP model by holding the WEI value at 0.6 mL/KJ, $\Delta'^{17}O$ of meteoric water at 0.035‰, $f_{H_2O\text{-in-food}}$ at 0.4, and leaf/stem ratio at 0.1. We run these models under different rh, representing humid (rh = 0.8), semi-arid (rh = 0.5) and arid (rh = 0.3) environments, with meteoric water $\delta^{18}O$ varying from –20‰ to +5‰. Figure 2-9a shows that both the maximum and minimum $\Delta'^{17}O_{bw}$ values decrease with decreasing rh, but the sensitivity of $\Delta'^{17}O_{bw}$ to rh in the MAX-EVAP model is dramatic while that in the MIN-EVAP model is negligible.

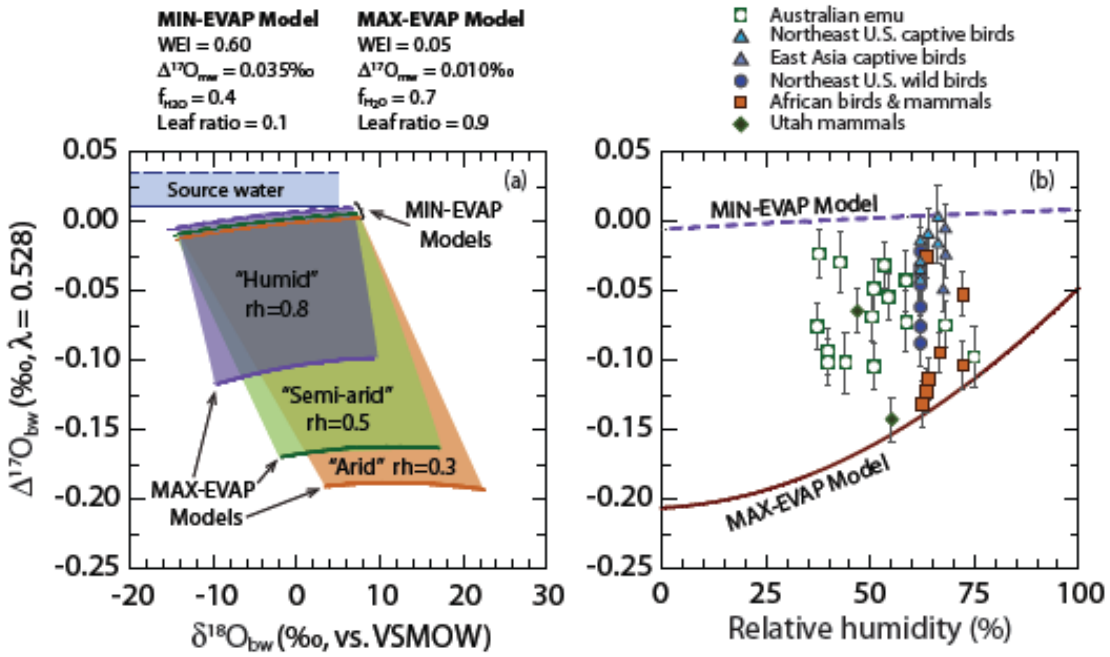

Figure 2-9. Modeled animal $\delta^{18}O_{bw} - \Delta'^{17}O_{bw}$ ranges under different relative humidities, and comparision wtih data. (a) Modeled animal $\delta^{18}O_{bw} - \Delta'^{17}O_{bw}$ range in humid (rh = 0.8, shown in purple shade), semi-arid (rh = 0.5, shown in green shade) and arid (rh = 0.3, shown in orange shade) climates. The blue rectangle in the upper left represents source water isotopic compositions used for the models. Thick dashed lines (upper limits) are model outputs from three MIN-EVAP models; solid lines (lower limits) are model outputs from the three MAX-EVAP models. Model parameters are as listed. MAX-EVAP models are highly sensitive to relative humidity change and range of $\Delta'^{17}O_{bw}$ increases with decreasing rh. Notice that the $\delta^{18}O_{bw} - \Delta'^{17}O_{bw}$ range will be extended if range of source water (blue shade) is extended. Note that Figure 2-4 provides the explanation for why these lines are curved. (b) Modeled $\Delta'^{17}O_{bw}$ range vs. relative humidity and comparison with data from modern animals. We run the MIN-EVAP and MAX-EVAP models with continuously changing rh, assuming $\delta^{18}O_{mw} = -4‰$. Ranges in $\Delta'^{17}O_{bw}$ for a population of animals increase with decreasing humidity: upper limits (MIN-EVAP) on $\Delta'^{17}O_{bw}$ stay about the same with rh, whereas lower limits (MAX-EVAP) decrease with decreasing humidity. The total range is predicted to be approximately 0.2‰ in extremely arid climates. Our data are approximately consistent with this prediction, but are not adequate for fully exploring the range of possible climates and physiologies. Relative humidity

data are from the CRU 2.0 gridded climate dataset (New et al., 2002, see Table 2-1 and Table A2.2 for more information).

Figure 2-9b shows $\Delta'^{17}O_{bw}$ versus rh, modeled for both the MAX-EVAP and MIN-EVAP scenarios. The model predicts an increasing range of $\Delta'^{17}O_{bw}$ with decreasing rh. We expect to observe both a wider range of $\Delta'^{17}O_{bw}$ and lower minimum $\Delta'^{17}O_{bw}$ for animals from arid environments. Our dataset is consistent with this prediction (Figure 2-9b), but is inadequate for fully evaluating the prediction. What is needed is a dataset where several species are studied, each across a wide range of climatic conditions. We are currently studying hippopotamus, elephant, giraffe, beaver, deer, and other animals across a wide range of climates, and the results support the model predictions presented in Figure 2-9b. This relationship between rh and $\Delta'^{17}O_{bw}$ forms the basis of an aridity index.

The advantage of using $\Delta'^{17}O_{bw}$ as an aridity proxy is that $\Delta'^{17}O_{bw}$ records evaporative signals with less influence from meteoric water compositions compared to the $\delta^{18}O$ aridity index (*e.g.,* Kohn, 1996; Levin et al., 2006). Unlike like $\Delta'^{17}O_{bw}$, $\delta^{18}O_{bw}$ of animals is strongly influenced by local surface water compositions. Hence, when taking $\delta^{18}O_{bw}$ of 'MAX-EVAP' animals as an aridity proxy, it is necessary to normalize to local $\delta^{18}O_{bw}$ of 'MIN-EVAP' animals first (or "evaporation sensitive" (ES) versus "evaporation insensitive" (EI) animals in the parlance of Levin et al., 2006). But the absolute depletions of $\Delta'^{17}O_{bw}$ for ES animals can directly be used to indicate arid environments without normalization to $\Delta'^{17}O_{bw}$ of EI animals. This principle is widely applicable to both modern and fossil animals for determining climate change and reconstructing paleaoclimate or paleaoaridity. A caveat is that one must account for the

possiblity of variable $\Delta'^{17}O$ of atmospheric O_2 when using $\Delta'^{17}O_{bw}$ to reconstruct paleoaridity.

2.5.3. Influence of $\Delta'^{17}O$ of atmospheric O_2

If the $\Delta'^{17}O$ of atmospheric O_2 [$\Delta'^{17}O$ (O_2)] was not constant in the past, as seems to have been case (*e.g.,* Luz et al., 1999; Bao et al., 2008), analysis of both EI and ES animals may be necessary for determining paleoaridity. For example, a ~0.1‰ change in $\Delta'^{17}O$ (O_2) may lead to ~0.03‰ change in $\Delta'^{17}O_{bw}$ (Table A2.1). In other words, low $\Delta'^{17}O_{bw}$ values of fossil samples may not necessarily reflect high aridity, but rather low $\Delta'^{17}O$ (O_2) values. Since the range in $\Delta'^{17}O_{bw}$ is strongly correlated to rh (Fig. 2-9b), a combination of examining both the range in $\Delta'^{17}O_{bw}$ and mean $\Delta'^{17}O_{bw}$ of a community of animals may allow resolution of the influence of both rh and $\Delta'^{17}O$ (O_2).

The Ukhaa Tolgod dinosaurs (late Cretaceous, Mongolia) (Fig. 2-8b) have a $\Delta'^{17}O_{bw}$ range of ~ 0.10‰ (a range that could plausibly increase with additional sampling). Based on the discussion in section 5.2, and the model predictions shown in Figure 2-9, this suggests relative humidities of ~0.8 or lower during that time. Previous studies suggest a seasonal and semi-arid environment for Nemegt Basin during late Cretaceous (Jerzykiewicz et al., 1993; Montanari et al., 2013). It is possible that the $\Delta'^{17}O$ (O_2) during late Cretaceous was different from present. If $\Delta'^{17}O$ (O_2) was higher, a more arid climate would be needed to explain the lowest $\Delta'^{17}O_{bw}$ values that we observe. Conversely, if $\Delta'^{17}O$ (O_2) was lower, more humid climates could explain the lowest $\Delta'^{17}O_{bw}$ values, but the range $\Delta'^{17}O_{bw}$ would still point to rh of about 0.8 or lower. In summary, both the range in $\Delta'^{17}O_{bw}$ and the mean of $\Delta'^{17}O_{bw}$ will be important in

distinguishing the rh signal from the $\Delta'^{17}O$ (O_2) signal during times when the latter was significantly different from present.

Another related factor to consider when interpreting isotopic compositions of fossils is diagenesis. Open system digenesis tends to elevate $\Delta'^{17}O$ of biominerals towards $\Delta'^{17}O$ of meteoric water (*e.g.,* Gehler et al., 2011), so anomalous $\Delta'^{17}O_{bw}$ indicates at least partial preservation of original biogenic signal. Thus, measured $\Delta'^{17}O$ values place upper limits on primary $\Delta'^{17}O$ values. If diagenisis did effect the dinosaur eggshell samples, then the Nemegt Basin may have been more arid or paleo $\Delta'^{17}O$ (O_2) values were more depleted than apparent from the measured isotopic compositions of the eggshells.

2.5.4. Case study: Australian Emus

Here we present data from Australian Emu eggshells as a case study for using the combination of $\Delta'^{17}O_{bw}$ and $\delta^{18}O_{bw}$ to study climate and ecology. The emu eggshell samples in this study were previously studied by Johnson et al. (1999). They were collected from a range of seasonal precipitation and vegetation regimes across Australia and show a wide range in both $\Delta'^{17}O_{bw}$ and $\delta^{18}O_{bw}$ (Fig. 2-10). Some of this variability in oxygen isotope compositions of emu body water may be explained by diverse meteoric water sources from different locations. Precipitation across northern and central Australia is highly seasonal. The Australian monsoon delivers precipitation to the north during the summer months, westerly storm tracks deliver precipitation to the south during the winter months, and the continental interior areas receive limited precipitation in all seasons (Tapper and Hurry, 1993; Johnson et al., 1999; Barras and Simmonds, 2009).

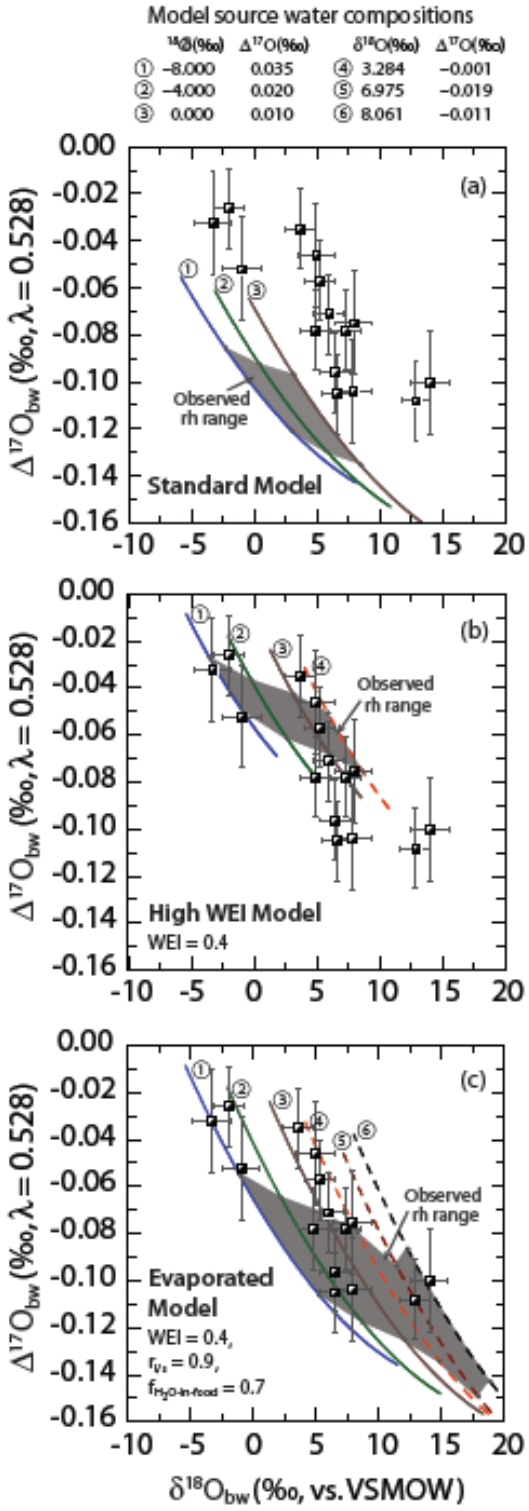

Figure 2-10. Comparisons of observed emu body water isotopic compositions with predictions from different models. Source waters 1, 2 and 3 are representative of typical primary rainfall compositions in Australia. Source waters 4, 5 and 6 are pre-evaporated waters of isotopic compositions calculated based on

pan evaporation of typical primary rainfall (Criss 1999). Source waters 4, 5 and 6 are evaporated in environments with rh = 0.5, 0.5 and 0.3, respectively, and evaporated until 80%, 70% and 70% of the initial water mass remains, respectively. Initial water oxygen isotope compositions are $\delta^{18}O_{initial}$ = –4.0‰ and $\Delta'^{17}O_{initial}$ = 0.020‰. Grey shading shows the rh range for the locations where the emu samples were collected, based on the CRU 2.0 data product, where rh values are the long-term monthly averages for emu breeding months (see Table 2-1 and Table A2.2 for rh data). (a) Comparisons between emu data and standard models with source water compositions of 1, 2 and 3. The models show large discrepancies with the data. (b) Comparisons between emu data and models with WEI adjusted to 0.4 (from a value of 0.17), and source water compositions of 1, 2, 3 and 4. (c) Comparisons between emu data and models with WEI = 0.4, $r_{l/s}$ =0.9 and $f_{H2O\text{-}in\text{-}food}$ = 0.7, and source water compositions of 1 to 6. The better agreement between data and the models showin in (b) and (c) suggest that emu typically have lower water use efficiency (higher WEI) than we initially assumed based on the ostrich analog, and that they commonly consume significant quantities of pre-evaporated water, either directly or as plant water sourced from pre-evaporated waters.

We initially ran the emu body water model with standard model settings (Table 2-3), and varied only the climate parameters, including relative humidity, and meteoric water $\delta^{18}O$ and $\Delta'^{17}O$. Based on Liu et al. (2010), we estimated an average $\delta^{18}O_{mw}$ value of -4‰ for emu breading season (July through September). $\Delta'^{17}O_{mw}$ studies on Australian precipitation has not been carried out yet, so we used a typical global $\Delta'^{17}O_{mw}$ values from the reported $\Delta'^{17}O$ ranges in Luz and Barkan (2010) and Li et al. (2015). We set up three emu body water models with reasonable ranges of meteoric water ($\delta^{18}O$, $\Delta'^{17}O$) inputs: (-8‰, 0.04‰), (-4‰, 0.03‰), (0‰, 0.02‰) for model 1, model 2 and model 3, respectively. Each model was run with under a range of relative humidities. In Figure 2-10, the grey shadowed areas show the typical rh range during the breeding season based on the CRU 2.0 dataset (as in Table 2-1 and Table A2.2). In this run, the overall λ trend

of emu samples is consistent with modeled curves, but none of the data points lie within the modeled range. The real data have a far greater range, are more enriched in $\delta^{18}O_{bw}$, and less depleted in $\Delta'^{17}O_{bw}$ compared to the model predictions.

One possible explanation for this discrepancy is that emu are not able to maintain water balance without drinking, unless a water-rich food source is available (Dawson et al., 1983; Patodkar et al., 2009). Field observations indicate that emus drink regularly, and hence their effective WEI values may change from low to high when they drink large amounts of water. Therefore, the original WEI value of 0.17 based on ostrich might not always be applicable to typical emus. If we change the WEI values in models 1, 2 and 3 from 0.17 to 0.4 (Figure 2-10b), the observed data with high $\Delta'^{17}O_{bw}$ fit better, except for a couple of points with high $\delta^{18}O_{bw}$. However, in this model, even extremely low rh can not account for the samples with low $\Delta'^{17}O_{bw}$.

It is possible and even likely that some of the water sources for the emu and the plants they eat are pre-evaporated. The Lake Eyre Basin, where many of the emu samples are found, extends across arid to semi-arid zones and is one of the largest internally drained river systems on Earth (Croke et al., 1996). The river system in the Lake Eyre Basin is characterized by extreme variation in discharge and flow duration, and is subject to high evaporative water losses (McMahon and Merz, 2005). Rainfall during the emu egg-lying season is usually sparse in Australia, and evaporation is the predominant cause of long-term water loss for the waterbodies in Lake Eyre Basin (Costelloe et al., 2003; Hamilton et al., 2005). As a result, observed $\delta^{18}O$ values of the waterbodies are enriched along local evaporation lines, and can even be as high as ~ +20‰ (Hamilton et al., 2005). The $\Delta'^{17}O$ of the remaining waterbodies should be low, as predicted by models of pan

evaporation as shown in Figure 2-1b (Criss, 1999; Luz and Barkan, 2010), and as observed for natural bodies of evaporated water (Luz and Barkan, 2010; Surma et al., 2015). Therefore, we set up an additional model (model 4) based on a pre-evaporated water source. Using simple pan evaporation, we calculate $\delta^{18}O = 3.284‰$ and $\Delta'^{17}O = -0.001‰$ for rh = 0.5 and 80% of initial water remained ($\delta^{18}O_{initial} = -4.000‰$, $\Delta'^{17}O_{initial} = 0.020‰$). By taking the evaporation effects into consideration, model 4 seems to explain the data with both high $\delta^{18}O_{bw}$ and high $\Delta'^{17}O_{bw}$ (Fig. 2-10b).

To explain data points with low $\Delta'^{17}O_{bw}$, we increased the amount of evaporative water input by increasing leaf ratio to 0.9 and food water content to 0.7. Models in Figure 2-10c have higher $r_{l/s}$ and $f_{H2O\text{-}in\text{-}food}$, but the same WEI as models in Figure 2-10b. Source water in model 5 and 6 are pre-evaporated waters for rh = 0.5 and rh = 0.3 when 70% initial water remains. With all these assumptions, samples low in $\Delta'^{17}O_{bw}$ and high in $\delta^{18}O_{bw}$ can be explained.

Overall, to the extent that our model predictions are accurate, the comparisons between models and observed patterns indicate emus typically have higher drinking water requirements than ostrich, and commonly obtain a large fraction of water from pre-evaporated water sources, reflecting the the unique hydrology of the Lake Eyre Basin. Future studies could better evaluate these suggestions by more controlled and comprehensive sampling, for example in case studies where surface waters, plant waters, and contemporaneously-formed biominerals are collected over a specific time interval, during which climatic conditions are monitored in detail.

2.6. CONCLUSIONS

The triple oxygen isotope modeling of animal body water described in this study reveals the potential of using $\Delta'^{17}O$ to learn more about the environment and ecology of animals. This model extends traditional $\delta^{18}O$ body water models to include $\Delta'^{17}O$, a better indicator of evaporation and relative contribution of metabolic water, and improves our ability to infer physiological and environmental information from biomineral isotopes. Observed animal body water isotopic compositions mostly validate our model predictions, although additional studies and more data are clearly needed to fully evaluate model predictions, and perhaps more importantly, to allow for refinement of the models. One of the most promising applications is using body water $\Delta'^{17}O$ as a new proxy for paleoaridity and paleophysiology.

In conclusion, this study presents several practical observations: (1) Animal body water $\Delta'^{17}O$ is most influenced by relative humidity, fraction of leaf water intake, free water content in food and WEI values. Other physiological factors play less important roles in controlling body water $\Delta'^{17}O$, and body mass is a minor factor in our models. (2) $\Delta'^{17}O_{bw}$ is almost always lower than $\Delta'^{17}O_{mw}$, primarily because of the low $\Delta'^{17}O$ inputs of evaporated waters (including leaf waters) and metabolic water, which reflects a combination of food-bound O and atmospheric O_2. (3) Populations of animals plot along approximately linear arrays in $d^{18}O_{bw}$ versus $\Delta'^{17}O_{bw}$ space, following a trend of increasing $\delta^{18}O_{bw}$ with decreasing $\Delta'^{17}O_{bw}$. (4) We predict and also observe that leaf-eating, relatively water-independent animals such as giraffe, ostrich, and deer have lower $\Delta'^{17}O_{bw}$ and higher $\delta^{18}O_{bw}$ than more water-dependent animals from the same regions (*e.g.*, hippopotamus, rhino, bison). Our model predicts that differences in $\Delta'^{17}O_{bw}$

between such groups of animals will increase with decreasing relative humidity. That is, the community-wide range in $\Delta'^{17}O_{bw}$ increases with decreasing rh, making $\Delta'^{17}O_{bw}$ a potential proxy for past aridity. (5) Emus apparently have higher drinking water requirements than initially expected based on our choice of ostrich as an anologue, and emu body water isotopic compositions are consistent with the evaporation-dominated environment in central Australia during emu egg-lying season. (6) The body water model can potentially be used to help constrain $\Delta'^{17}O$ of paleoatmospheric O_2. Reconstructed $\Delta'^{17}O(O_2)$ values may be an important indicator of paleo-CO_2 levels, paleo-CO_2/O_2 ratio, and past rates of carbon cycling.

ACKNOWLEDGEMENTS

We thank Matt Kohn for sharing his body water $^{18}O/^{16}O$ model spreadsheet, and Scott Pitz, Sara Rivero, and Greg Henkes for providing chicken and wild bird eggshells. We also thank Shuning Li and Haoyuan Ji for helping with sample analysis.
We thank the donors of the American Chemical Society, Petroleum Research Fund for partial support of this work.

APPENDIX A. SUPPLEMENTARY DATA

Supplementary data associated with this chapter (Table A2.1, Table A2.2, Table A2.3 and Matlab scripts of the body water model) can be found in the appendices and supplementary files.

CHAPTER 3:MESOZOIC CARBON CYCLING FROM TRIPLE OXYGEN ISOTOPES IN FOSSIL DINOSAURIAN EGGSHELL CARBONATE

Abstract

The triple oxygen isotope anomaly of atmospheric O_2 [$\Delta'^{17}O(O_2)$] is related to stratospheric photochemistry, the partial pressure of atmospheric CO_2 (pCO_2), and global primary productivity (GPP), and hence is a tracer of global carbon cycle dynamics. A tantalizing opportunity exists to study carbon cycles of the deep geologic past, because ~ 5 – 30% of the oxygen in animal body water comes from atmospheric O_2 through respiration ($CH_2O + O_2 \rightarrow CO_2 + H_2O$), and biogenic carbonates forming in isotopic equilibrium with body water can preserve this $\Delta'^{17}O(O_2)$ signal over geological timescales. In order to use this property, we predict the degree of dilution of the $\Delta'^{17}O(O_2)$ signal in total animal body water by other sources of oxygen based on a triple oxygen isotope animal body water model. We address uncertainties from climate and physiology by modeling endmember and mean $\Delta'^{17}O$(body water) values under different $\Delta'^{17}O(O_2)$. Using these modeled relationships between $\Delta'^{17}O$(body water) and $\Delta'^{17}O(O_2)$, we narrow the range of concordant $\Delta'^{17}O(O_2)$ values that are consistent all observed $\Delta'^{17}O$(body water) values of contemporaneous animals. We have applied this method to fossil dinosaurian eggshells of Jurassic and Cretaceous age. Mid- and Late Cretaceous fossil samples indicate slightly lower or similar $\Delta'^{17}O(O_2)$ values compared to modern samples, indicating similar or slightly higher pCO_2 or similar or slightly lower GPP. The Late Jurassic samples indicate anomalously low $\Delta'^{17}O(O_2)$ values, pointing to pCO_2 several times higher than present, reduced gross primary productivity, or a combination of both. Assuming present day GPP, pCO_2 was up to 1490±780 ppm during the Late

Jurassic. The triple oxygen isotope approach, while unable to uniquely constrain pCO_2 or GPP, shows promise for identifying distinctive modes of the carbon cycle in the geological past. Reconstructed $\Delta'^{17}O(O_2)$ constrains the slope of pCO_2 versus GPP (that is, the GPP sensitivity to pCO_2), which is of further value for investigating paleo-carbon-cycling.

3.1. INTRODUCTION

Atmospheric CO_2 is thought to play a major role in regulating global temperature and biological activity (Arrhenius, 1896; Sundquist and Broecker, 1985; Royer et al., 2001b). Ice core records show a close coupling between temperature (reconstructed from ice $\delta^{18}O$) and the partial pressure of CO_2 (pCO_2) of trapped gases in the ice cores (Petit et al., 1999; Lüthi et al., 2008). Carbon dioxide levels affect key aspects of Earth's ecosystems, including primary productivity, distribution of terrestrial vegetation, and pH of the oceans (Long, 1991; Curtis and Wang, 1998; Cramer et al., 2001; Montañez et al., 2007; Chaboureau et al., 2014). The only direct records of pCO_2 come from the trapped gases in polar ice cores, records which extend back to about 800,000 years (Barnola et al., 1987; Petit et al., 1999; Lüthi et al., 2008; Ahn et al., 2012). Different methods have been used to investigate the pCO_2 in the deeper geological past, including fossil leaf stomatal index (Royer, 2001; Haworth et al., 2005; Passalia, 2009), fossil leaf stomatal density (Woodward, 1987; Royer, 2001), carbon isotopes of palaeosols (Cerling, 1991; Ekart et al., 1999), boron isotopes of planktonic foraminifera (Pearson et al., 2009; Henehan et al., 2013), and Earth system modeling (Berner, 2006; Franks et al., 2014). However, each of

these methods has specific limitations in constraining pCO_2 in the past (Royer et al., 2001a; Beerling and Royer, 2011), and hence, further studies remain essential.

Triple oxygen isotopes (^{16}O, ^{17}O, ^{18}O) in sulfates, oxides, and skeletal apatite are the basis of a relatively new approach for reconstructing past pCO_2 (Bao et al., 2008) (Pack et al., 2013; Gehler et al., 2016). Oxygen atoms in these minerals partially originate from atmospheric O_2, whose triple oxygen isotope composition relates to pCO_2, gross primary productivity (GPP) and other factors (Luz et al., 1999; Bao et al., 2008; Blunier et al., 2012; Young et al., 2014). This relationship arises because of the balance between ^{17}O-anomaly production in the stratosphere by photochemical reactions among O_2, O_3, and CO_2, and ^{17}O-anomaly sequestration to the hydrosphere forced primarily by photosynthesis and respiration of the global biota. Conditions of high pCO_2 or low GPP (or both) result in a deficit of ^{17}O in atmospheric O_2 relative to terrestrial reservoirs such as waters and rocks, while low pCO_2 and high GPP cause atmospheric O_2 to have an isotopic composition more similar to terrestrial reservoirs. Section 4 discusses these phenomena in more detail.

This method of reconstructing past carbon cycling involves three separate challenges: (1) measuring ^{17}O anomalies of minerals with a high degree of precision (~10 ppm or 0.01‰ in the $\Delta'^{17}O$ value, defined in Section 2); (2) reconstructing $\Delta'^{17}O$ of atmospheric O_2 [$\Delta'^{17}O(O_2)$] based on measured $\Delta'^{17}O$ values of minerals; and (3) relating $\Delta'^{17}O(O_2)$ to pCO_2 and GPP. In this study, challenge (1) is addressed using the recently developed analytical methods described in Passey et al. (2014) for $\Delta'^{17}O$ analysis of CO_2 (including CO_2 liberated from carbonates by acid digestion). Challenge (3) is addressed using the $\Delta'^{17}O(O_2)$-pCO_2-GPP model of Cao and Bao (2013). To address challenge (2),

we develop a new "environmental physiology isotope concordance" (EPIC) approach that explicitly accounts for uncertainty introduced by climate and animal physiology, both of which strongly control $\Delta'^{17}O$ of body water independently of the control that $\Delta'^{17}O(O_2)$ exerts on $\Delta'^{17}O$ of body water.

In this chapter, we will first present triple oxygen isotope compositions of 71 dinosaurian eggshell carbonates ranging in age from Late Jurassic to Late Cretaceous. We then use the triple oxygen isotope body water model described in Chapter 2 to model the isotopic relationships between atmospheric O_2 and animal body water. We introduce the EPIC approach and illustrate how it is used to place constraints on $\Delta'^{17}O(O_2)$. Finally, we infer Mesozoic carbon cycling, including pCO_2 and GPP, using the reconstructed $\Delta'^{17}O(O_2)$ values combined with the $\Delta'^{17}O$ budget model of Cao and Bao (2013).

3.2. MATERIALS AND METHODS

3.2.1. Triple oxygen isotope notation and background

We use δ and δ' - notation to express the relative abundance of ^{17}O and ^{18}O, which are defined as:

$$\delta^{x}O=\left(\frac{{}^{x}R_{sample}}{{}^{x}R_{VSMOW}}-1\right)\times 1000$$

$$\delta'^{x}O=\ln\left(\frac{{}^{x}R_{sample}}{{}^{x}R_{VSMOW}}\right)\times 1000$$

Here $R = {}^{x}O/{}^{16}O$ and x = 17 or 18. The logarithmic δ'-notation better describes the linearized relationship of mass-dependent oxygen isotope fractionations. Fractionation factors for oxygen isotopes between different phases or states are defined as: $\alpha^{x}_{A\text{-}B}={}^{x}R_A/{}^{x}R_B$, where A and B refer to different phases or states of oxygen-bearing

materials. Mass-dependent fractionation (MDF) involving three oxygen isotopes can be related through a fractionation exponent, θ or λ (Barkan and Luz, 2005; Landais et al., 2006; Luz and Barkan, 2010). The MDF laws can be equated as: $\alpha^{17}_{A\text{-}B} = \left(\alpha^{18}_{A\text{-}B}\right)^{\theta_{A\text{-}B}}$ (Mook and Rozanski, 2000), where $\theta_{A\text{-}B}$ (or $\lambda_{A\text{-}B}$) is the specific MDF exponent for oxygen isotopes between phases A and B, which is approximately 0.52 for physical and chemical processes at Earth surface temperatures (Craig, 1957; Friedman and O'Neil, 1977; Miller, 2002; Young et al., 2002; Rumble et al., 2007). Different oxygen isotope fractionation processes have variable θ values, ranging from ~0.5160 of kinetic process to 0.5305 of high temperature equilibrium process (Young et al., 2002; Cao and Liu, 2011).

The $\Delta'^{17}O$ value describes the departure of $\delta'^{17}O$ from a reference relationship between $\delta'^{17}O$ and $\delta'^{18}O$:

$$\Delta'^{17}O = \delta'^{17}O - \lambda_{ref} \times \delta'^{18}O \quad (1)$$

where λ_{ref} is the slope of a reference $\delta'^{17}O$ - $\delta'^{18}O$ line. In this study, we choose the global meteoric water line (GMWL) of $\lambda_{ref} = 0.528$ as reference (Meijer and Li, 1998; Luz and Barkan, 2010). Variation in θ or λ values during oxygen isotope fractionations will lead to different values of $\Delta'^{17}O$. For instance, θ of kinetic processes are typically lower than the equilibrium processes. Thus leaf waters or evaporated surface waters that experience different degrees of evaporation show relative low $\Delta'^{17}O$ values compared to stem waters and unevaporated surface waters (Fig. 3-1).

In contrast to mass dependent fractionation, mass-independent fractionation (MIF) is independent of the mass differences between isotopes, and can lead to $\Delta'^{17}O$ values with large positive or negative magnitudes. These processes follow a relationship of $\alpha^{17} \approx \alpha^{18}$ (Thiemens and Heidenreich, 1983; Thiemens et al., 1995). Photochemical MIF

processes are particularly important in the stratosphere and are a significant contributor to the anomalous $\Delta'^{17}O$ values observed in atmospheric O_2 (Fig. 3-1).

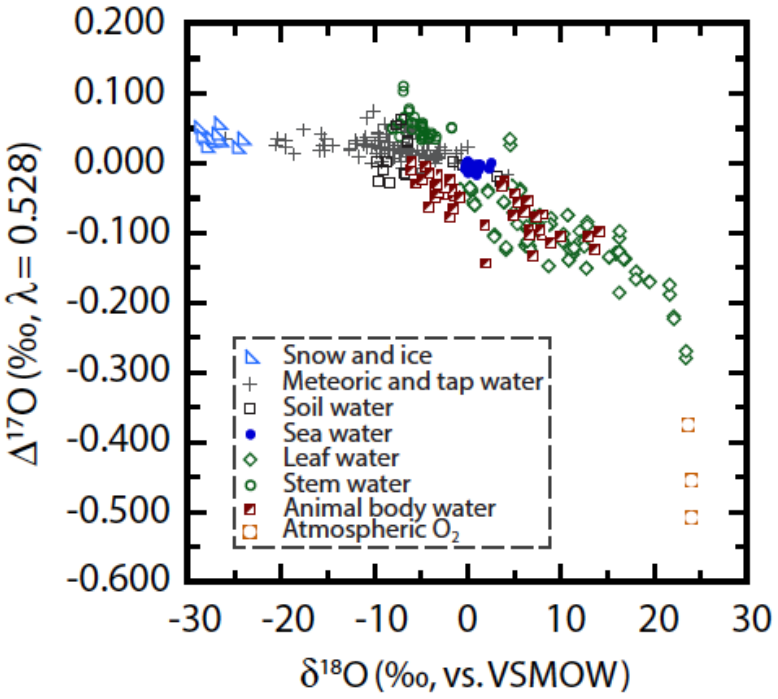

Figure 3-1. Triple oxygen isotope data compilation of sea water (Luz and Barkan, 2010), meteoric water (Luz and Barkan, 2010; Li et al., 2015), snow and ice (Landais et al., 2008; Landais et al., 2012a; Landais et al., 2012b), plant water (Landais et al., 2006), soil water reconstructed from soil carbonates (Passey et al., 2014), animal body water (Chapter 2) and atmospheric O_2 (Barkan and Luz, 2005, 2011; Young et al., 2014). There is large ^{17}O-deficit in atmospheric O_2 compared to natural waters.

Atmospheric O_2 is a significant oxygen input with distinct isotopic composition that accounts for ~ 5 – 30% oxygen of the total body water of nonaquatic terrestrial animals. Other major oxygen inputs include drinking water and stem water (both with $\Delta'^{17}O$ values similar to meteoric waters), and leaf water (with markedly lower $\Delta'^{17}O$ values which decrease with decreasing relative humidity). Generally speaking, animal body water oxygen isotope compositions show trends similar to those of leaf waters

because of kinetic effects during evaporation, and lower $\Delta'^{17}O$ values than surface waters because of the low $\Delta'^{17}O$ inputs from atmospheric O_2 (Fig. 3-1).

3.2.2. Materials

We analyzed the triple oxygen isotope compositions of 71 eggshell samples of the Late Cretaceous, Early Cretaceous and Late Jurassic epochs. Most of the eggshell samples are identified as dinosaurian, including Oviraptoridae, *Maiasaura*, *Troodon* and some unidentified dinosaurid samples. Others are not clearly related to dinosaurs, such as crocodilian eggshell, or lack identification. Sample information is summarized in Table 3-1.

Samples are divided into groups based on locality and age (Table 3-1). Overall, we have 6 groups of different ages. Late Cretaceous samples are in Mastrichitian age from Shanyang Formation (×5) Shaanxi, China; Campanian to Mastrichitian age from Nemegt Formation (×8), Bugin Tsav, Mongolia; Campanian age from Djadokhta Formation, Mongolia (Ukhaa Tolgod ×4, Bayn Dzak ×4), Two Medicine Formation (×15), Montana, USA, and Jingangkou Formation (×12), Shandong, China; and Santonian age from Jiangjunding Formation (×2), Shandong, China. Early Cretaceous samples are in Albian age from Cedar Mountain Formation (×9), Utah, USA, and Xinminpu Group (×1), Gansu, China. Late Jurassic samples are in Oxfordian age from Morrison Formation, Colorado, USA (×11). We will interpret pCO_2 and GPP for each time period separately following these divisions.

Table 3-1. Sample information

Age	Sample ID/Formation			Taxon / Ootaxon	Location
Late Cretaceous					
Maastrichtian	*Shanyang Formation*				
	S140519-1	S140517-4		Elongatoolithidae	Shanyang Basin, Shaanxi, China
	S140515-19	S140514-7			
	S140515-16				
Maastrichtian /Campanian	*Nemegt Formation*				
	Bugin Tsav 1.1	Bugin Tsav eggshell BT1		Oviraptorid	Bugin Tsav, Nemegt Basin Mongolia
	BB06 Bugin Tsav	Bugin Tsav eggshell BT2			
	BB08 Bugin Tsav	Bugin Tsav eggshell BT3			
	Bugin Tsav BT4	Bugin Tsav 1GM100/1189			
Campanian	*Djadokhta Formation*				
	Ukhaa Tolgod JH1	A5-1.1 Ukhaa Tolgod		Oviraptorid	Ukhaa Tolgod, Nemegt Basin Mongolia
	Ukhaa Tolgod A7 1.1	Ukhaa Tolgod 1GM100/975			
	Djadokhta Formation				
	A26-Bayn-Dzak	Bayn Dzak 1GM100/1150		Oviraptorid	Bayn Dzak, Nemegt Basin, Mongolia
	Bayn Dzak 1GM 100/1154, -2			Protoceratops (?)	
	Two Medicine Formation				
	UCM-377-1	UCM-948-1	UCM-949-1	Maiasaura	Teton, Montana, USA
	UCM-377-2	UCM-948-2	UCM-949-2		
	UCM-377-3	UCM-948-3	UCM-949-3		
	UCM-378-1	UCM-378-3	UCM-952-2	Troodon	
	UCM-378-2	UCM-952-1	UCM-952-3		
	Jingangkou Formation				
	S090723-D2#			Elongatoolithidae	Jiaozhou Basin, Shandong, China
	L110813-D2#	L101209-D2		Elongatoolithidae	Laiyang Basin, Shandong, China
	L120625-D3	L100525-D2-1			
	L120722-D3				
	L110712-D2	L100525-D2-2		Ovaloolithidae	
	L100510-D6#	L100509-D2C			
	L100601-D5				
	L110816-D1			Crocodile (?)	
Santonian	*Jiangjunding Formation*				
	L120630-D1#			Spheroolithidae	Laiyang Basin, Shandong, China
	L130605-D1				
Early Cretaceous					
Albian	*Cedar Mountain Formation*				
	UCM-264-6-1	UCM-861-1	UCM-157-1	Dinosaurid	Emery, Utah, USA
	UCM-264-6-2	UCM-861-2	UCM-157-2		
	UCM-264-6-3	UCM-861-3	UCM-157-3		
	Xinminpu Group				
	G140616-A			Stalicoolithidae?	Yujingzi Basin, Gansu, China
Late Jurassic					
Oxfordian	*Morrison Formation*				
	UCM-418-1	UCM-532-1-1	UCM-656-1	Dinosaurid	Mesa, Colorado, USA
	UCM-418-2	UCM-532-1-2	UCM-656-2		
	UCM-418-3	UCM-532-1-3	UCM-656-3		
	UCM-418-4	UCM-532-1-4			

3.2.3. Analytical methods

The isotopic analyses of all samples were performed in the stable isotope lab at Johns Hopkins University using a dual inlet Thermo MAT 253 isotope mass spectrometer. All dinosaur eggshell samples were analyzed for triple oxygen isotope composition following the analytical methods described in Passey et al. (2014). Fossil samples may endure different degrees of digenesis. Prior to isotopic sampling, the surface layers of all fossil eggshell samples were removed by mechanical abrasion because they appeared to be more altered than the interior of the eggshells. Typically 7-9 mg of eggshell calcite was sufficient for one analysis of well-preserved samples, but 10-14 mg was needed for less well preserved samples that had non-carbonate ingrowths (e.g., silica replacement of pore space or carbonate; see Section 3 for more information on diagenetic alteration of the samples). The triple oxygen isotope analytical procedure involves phosphoric acid digestion of carbonate at 90 °C, reduction of the purified CO_2 product by hydrogen over hot (560 °C) Fe catalyst, fluorination of the purified H_2O product at 360 °C using CoF_3, and analysis of the purified O_2 by extended-collection-time dual inlet mass spectrometry. Details of this analytical method can be found in Passey et al. (2014).

Triple oxygen isotope values were first normalized to the VSMOW2 and SLAP2 scale with a reference slope of $\lambda_{ref} = 0.528$ (Schoenemann et al., 2013). Then, the $\delta'^{18}O$ values of sample eggshells were corrected based results from standards analyzed along with the samples (NBS-18, NBS-19, 102-GC-AZ01, Tank #2 CO_2) with known $\delta'^{18}O$ values, using the correction scheme described in Passey et al. (2014).

Dinosaur samples reported in this study were analyzed from February 2013 to August 2015. The observed triple oxygen isotope compositions of the four standards

were: Tank #2 CO_2, n = 30, $\delta'^{18}O$ = 31.6 ± 0.6‰, $\Delta'^{17}O$ = –0.119 ± 0.008‰; NBS-18, n = 23, $\delta'^{18}O$ = 15.1 ± 0.5‰, $\Delta'^{17}O$ = –0.101 ± 0.013‰; NBS-19, n = 29, $\delta'^{18}O$ = 36.4 ± 0.7‰, $\Delta'^{17}O$ = –0.140 ± 0.012‰; 102-GC-AZ01, n = 16, $\delta'^{18}O$ = 23.8 ± 0.7‰, $\Delta'^{17}O$ = –0.108 ± 0.014‰. Long-term mean external precisions (1σ) observed for standards are 0.6‰ and 0.011‰ for $\delta'^{18}O$ and $\Delta'^{17}O$, respectively. Except for $\Delta'^{17}O$ value of 102-GC-AZ01, these values are indistinguishable from the values reported in Passey et al. (2014). We have observed slightly lower $\Delta'^{17}O$ values of 102-GC-AZ01 (~0.015‰ lower) since 2014.

In order to calculate the triple oxygen isotope compositions of dinosaur body water, we still need a dinosaur body temperature to estimate oxygen isotope fractionation factors between eggshell carbonates and body water. However, dinosaur thermoregulation has been debated for many decades (Weishampel et al., 1990). Recently, Eagle et al. (2011) and Eagle et al. (2015) used clumped isotope thermometry to determine dinosaur body temperatures from fossil teeth and eggshells. They observed similar body temperatures (36-38 °C) to modern endotherms for sauropods and titanosaurs, but lower body temperatures (~ 30 °C) for oviraptors. Our clumped isotope results (Table A3.1) for the oviraptors from Mongolia also indicate similar low body temperatures as Eagle et al. (2015). These results suggest variability in non-avian dinosaur thermoregulation and body temperature. In this case, the fractionation factors (α) of oxygen isotopes might be variable for dinosaurs with different body temperatures, and hence influence the final calculations of body water isotope compositions. Passey et al. (2014) presented an oxygen isotope fractionation factor of $^{18}\alpha_{CaCO_3-H_2O} = 1.0380 \pm 0.0008$ for eggshell carbonates and body water at bird body

temperature (~ 38-40 °C). Based on previous oxygen isotope fractionation studies (O'Neil et al., 1969; Kim and O'Neil, 1997), we estimated that 10 °C decrease in dinosaur body temperature will lead to ~ 0.002 increase in $^{18}\alpha_{CaCO_3\text{-}H_2O}$, and hence ~ 1.9‰ decrease in calculated body water $\delta^{18}O$ values. But fractionation exponents are not closely related to temperature. Using the fractionation exponents reported by Passey et al. (2014), $\lambda_{CaCO_3-H_2O} = 0.5245 \pm 0.0003$, we calculate that a 0.002 increase in $^{18}\alpha_{CaCO_3\text{-}H_2O}$ will only cause ~ 0.007‰ increase in body water $\Delta'^{17}O$ values. In this study, we will mainly focus on using $\Delta'^{17}O$. So ~ 1.9‰ variations in $\delta^{18}O$ will not influence our conclusions, and ~ 0.007‰ variations in $\Delta'^{17}O$ is negligible within analytical error. Consequently, we calculate the triple oxygen isotope compositions for dinosaur body water based on the Passey et al. (2014) fractionation factors for modern eggshell carbonates. For convenience, all discussions later in this paper refer to the equivalent body water oxygen isotope compositions calculated from the eggshell carbonates. All carbonate isotopic data and calculated body water isotopic compositions are reported in Table 3-2.

We also carried out $\delta^{13}C$, $\delta^{18}O$, and clumped isotope analyses on a subset of samples. These samples were digested by 100% phosphoric acid (H_3PO_4) to produce CO_2 and analyzed for $\delta^{13}C$, $\delta^{18}O$, and clumped isotopes after the CO_2 was purified through an extraction line designed for carbonate clumped isotope thermometry (Passey et al., 2010; Henkes et al., 2014). For these analyses, $\delta^{18}O$ values are given on the VPDB scale and are normalized to NBS-19. $\delta^{18}O$ of VPDB scale was converted to the VSMOW scale using the relationship $\delta^{18}O_{VSMOW} = 1.03091 \times \delta^{18}O_{VPDB} + 30.91$ (Coplen et al., 1983). We calculated paleotemperatures using linear regressions through the Δ_{47}-temperature calibration from Defliese et al. (2015): $\Delta_{47} = 37120/T^2 + 0.2784$ (T in Kelvin). All isotope

values ($\delta^{17}O$, $\delta^{18}O$, $\Delta'^{17}O$, $\delta^{13}C$, Δ_{47}) used in this paper are in ‰ (parts per thousand) notation and are reported in Table 3-2 and Table A3.1.

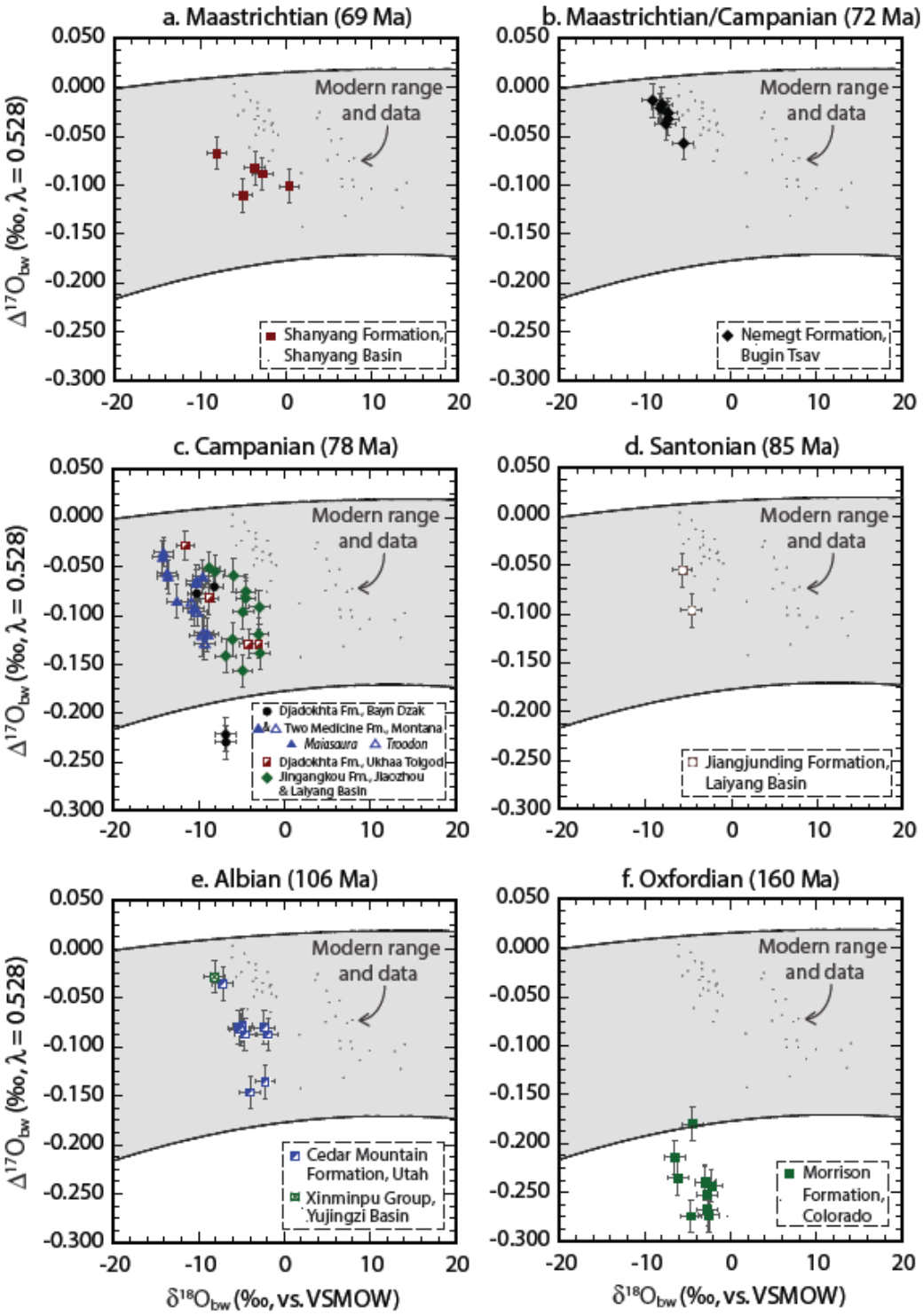

Figure 3-2. Measured dinosaur body water triple oxygen isotope compositions from different time intervals, and comparisons with modern animals. The small black dots are body water data from modern samples reported in Chapter 2. Grey shadowed area represents the maximum possible range in $\Delta'^{17}O_{bw}$ for dinosaurs, predicted from the MAX-EVAP-2 and MIN-EVAP-2 models when assuming present day $\Delta'^{17}O(O_2)$ value (–0.506‰, Barkan and Luz (2011)). Note that rh values in MAX-EVAP-2 and MIN-EVAP-2 models are 0.1 and 0.9 to better account for uncertainty in past climates. (a) Mastrichtian (Late Cretaceous) samples from Shanyang Formation of China. (b) Maastrichtian/Campanian (Late Creteaceous) samples from Nemegt Formation of Bugin Tsav, Mongolia. (C) Campanian (Late Cretaceous) samples from Djadokht Formation (Bayn Dzak and Ukhaa Tolgod) of Mongolia, Two Medicine Formation of USA and Jingangkou Formation of China. Two Medicine Formation samples consist of two types of dinosaurs, *Troodon* (open triangle) and *Maiasaura* (filled triangle). Most of the Djadokhta Formation samples are *oviraptorid*, except for two samples of the lowest $\Delta'^{17}O$ values from Bayn Dzak are possibly *protoceratops*. Jingangkou Formation samples are poorly identified for species. (d) Santonian (Late Cretaceous) samples from Jiangjunding Formation of China. (e) Albian (Early Cretaceous) samples from Cedar Mountain Formation of USA and Xinminpu Group of China. (f) Oxfordian (Late Jurassic) samples from Morrison Formation of USA.

3.3. RESULTS AND PRELIMINARY DISCUSSION

3.3.1. Stable isotopes

Stable isotope results for dinosaur eggshell carbonate and equivalent body water are reported in Table 3-2. Figure 3-2 shows body water triple oxygen isotope compositions of dinosaurs for each time period in the context of results for modern animals, while Figure 3-3 illustrates the values as a function of geologic time. We observe significant variability in dinosaur body water triple oxygen isotope compositions for different groups of dinosaurs and also within the same groups of dinosaurs, with the overall variability exceeding that observed for modern animals.

Table 3-2. Measured isotopic compositions of eggshell samples, and calculated compositions of parent waters of these samples. Values are given in units of per mil (‰) relative to the VSMOW-SLAP scale of Schoenemann et al. (2013), with $\lambda = 0.528$.

Time	Sample ID	N[a]	Measured values				$^{18}\alpha$[d] ($CaCO_3$–H_2O)	Calculated body water values			
			$\delta^{18}O_c$[b]	1σ[c]	$\Delta^{17}O_c$[b]	1σ[c]		$\delta^{18}O_w$[b]	±[e]	$\Delta^{17}O_w$[b, f]	±[e]
Late Cretaceous											
Mastrichtian	*Shanyang Formation*										
	S140519-1	2	29.526	0.3	-0.196	0.001	1.0380	-8.120	1.2	-0.067	0.017
	S140515-19	2	35.045	1.2	-0.217	0.001	1.0380	-2.803	1.2	-0.088	0.017
	S140515-16	2	34.186	0.9	-0.211	0.005	1.0380	-3.630	1.2	-0.082	0.017
	S140517-4	2	38.313	0.1	-0.230	0.004	1.0380	0.346	1.2	-0.101	0.017
	S140514-7	2	32.694	1.2	-0.239	0.008	1.0380	-5.067	1.2	-0.110	0.017
Maastrichtian /Campanian	*Nemegt Formation*										
	Bugin Tsav 1.1	3	30.364	0.2	-0.154	0.005	1.0380	-7.313	1.1	-0.026	0.015
	BB06 Bugin Tsav	2	32.204	0.4	-0.186	0.008	1.0380	-5.540	1.2	-0.057	0.017
	BB08 Bugin Tsav	2	30.351	0.6	-0.161	0.001	1.0380	-7.325	1.2	-0.032	0.017
	Bugin Tsav eggshell BT1	2	29.603	0.5	-0.146	0.006	1.0380	-8.045	1.2	-0.017	0.017
	Bugin Tsav eggshell BT2	3	29.396	0.2	-0.150	0.006	1.0380	-8.245	1.1	-0.021	0.015
	Bugin Tsav eggshell BT3	3	30.280	0.3	-0.155	0.001	1.0380	-7.394	1.1	-0.026	0.015
	Bugin Tsav 1GM100/1189	2	28.470	0.1	-0.142	0.001	1.0380	-9.137	1.2	-0.013	0.017
	Bugin Tsav BT4	2	30.058	0.0	-0.166	0.006	1.0380	-7.607	1.2	-0.037	0.017
Campanian	*Djadokhta Formation*										
	Ukhaa Tolgod JH1	3	34.865	0.5	-0.258	0.006	1.0380	-2.977	1.1	-0.129	0.015
	Ukhaa Tolgod 1GM100/975	2	28.824	1.0	-0.211	0.019	1.0380	-8.796	1.2	-0.082	0.017
	A5-1.1 Ukhaa Tolgod	3	33.633	1.0	-0.258	0.001	1.0380	-4.163	1.1	-0.129	0.015
	Ukhaa Tolgod A7 1.1	3	25.951	0.5	-0.157	0.003	1.0380	-11.564	1.1	-0.028	0.015
	Djadokhta Formation										
	A26-Bayn-Dzak	3	29.440	1.1	-0.199	0.004	1.0380	-8.203	1.1	-0.070	0.015

Table 3-2 (continued)

Time	Sample ID	N[a]	Measured values				^{18}a[d] ($CaCO_3$–H_2O)	Measured values			
			$d^{18}O_c$[b]	1s [c]	$D^{17}O_c$[b]	1s [c]		$d^{18}O_c$[b]	1s [c]	$D^{17}O_c$[b]	±[e]
Campanian	*Djadokhta Formation (continued)*										
(continued)	Bayn Dzak 1GM100/1150	4	27.319	0.4	-0.205	0.008	1.0380	-10.247	1.0	-0.077	0.014
	Bayn Dzak 16M 100/1154	2	30.847	0.4	-0.358	0.001	1.0380	-6.848	1.2	-0.229	0.017
	Bayn Dzak 1GM100/1154-2	2	30.822	0.3	-0.350	0.002	1.0380	-6.871	1.2	-0.221	0.017
	Two Medicine Formation										
	UCM-377-1	2	23.750	0.6	-0.185	0.002	1.0380	-13.685	1.2	-0.056	0.017
	UCM-377-2	2	23.219	0.1	-0.169	0.009	1.0380	-14.196	1.2	-0.040	0.017
	UCM-377-3	2	23.859	0.5	-0.189	0.003	1.0380	-13.579	1.2	-0.060	0.017
	UCM-948-1	3	27.282	0.4	-0.196	0.004	1.0380	-10.281	1.1	-0.067	0.015
	UCM-948-2	2	27.311	0.6	-0.193	0.012	1.0380	-10.254	1.2	-0.064	0.017
	UCM-948-3	2	28.075	0.0	-0.189	0.007	1.0380	-9.517	1.2	-0.060	0.017
	UCM-949-1	3	23.298	0.2	-0.164	0.015	1.0380	-14.120	1.1	-0.035	0.015
	UCM-949-2	2	26.957	0.1	-0.222	0.001	1.0380	-10.595	1.2	-0.093	0.017
	UCM-949-3	2	24.938	0.4	-0.214	0.003	1.0380	-12.540	1.2	-0.085	0.017
	UCM-378-1	2	26.675	0.5	-0.215	0.000	1.0380	-10.867	1.2	-0.086	0.017
	UCM-378-2	2	28.284	0.4	-0.256	0.005	1.0380	-9.317	1.2	-0.128	0.017
	UCM-378-3	2	28.184	0.1	-0.246	0.004	1.0380	-9.413	1.2	-0.117	0.017
	UCM-952-1	3	27.393	0.5	-0.225	0.007	1.0380	-10.175	1.1	-0.096	0.015
	UCM-952-2	1	27.946	–	-0.249	–	1.0380	-9.643	1.5	-0.120	0.022
	UCM-952-3	2	28.655	0.2	-0.248	0.005	1.0380	-8.959	1.2	-0.119	0.017
	Jingangkou Formation										
	S090723-D2#	2	32.914	0.9	-0.225	0.017	1.0380	-4.856	1.2	-0.096	0.017
	Jingangkou Formation										
	L110813-D2#	2	30.852	0.8	-0.270	0.006	1.0380	-6.842	1.2	-0.141	0.017

Table 3-2 (continued)

Time	Sample ID	N[a]	Measured values				^{18}a[d] ($CaCO_3$–H_2O)	Measured values			
			$d^{18}O_c$[b]	1s [c]	$D^{17}O_c$[b]	1s [c]		$d^{18}O_c$[b]	1s [c]	$D^{17}O_c$[b]	±[e]
Campanian	*Jingangkou Formation (continued)*										
	L120625-D3	2	35.007	0.6	-0.267	0.002	1.0380	-2.840	1.2	-0.138	0.017
	L120722-D3	2	31.666	0.5	-0.253	0.000	1.0380	-6.058	1.2	-0.124	0.017
	L101209-D2	2	29.552	0.2	-0.184	0.005	1.0380	-8.095	1.2	-0.055	0.017
	L100525-D2-1	2	33.258	0.7	-0.211	0.008	1.0380	-4.524	1.2	-0.082	0.017
	L110712-D2	2	28.825	0.3	-0.180	0.008	1.0380	-8.795	1.2	-0.051	0.017
	L100510-D6#	2	31.788	1.3	-0.188	0.001	1.0380	-5.941	1.2	-0.059	0.017
	L100601-D5	2	33.279	1.7	-0.204	0.001	1.0380	-4.505	1.2	-0.075	0.017
	L100525-D2-2	2	34.933	1.0	-0.220	0.001	1.0380	-2.911	1.2	-0.091	0.017
	L100509-D2C	2	34.837	1.1	-0.248	0.016	1.0380	-3.004	1.2	-0.119	0.017
	L110816-D1	2	32.900	1.5	-0.285	0.005	1.0380	-4.869	1.2	-0.156	0.017
Santonian	*Jiangjunding Formation*										
	L120630-D1#	2	33.123	0.0	-0.225	0.006	1.0380	-4.654	1.2	-0.096	0.017
	L130605-D1	2	31.990	0.2	-0.184	0.000	1.0380	-5.746	1.2	-0.055	0.017
Early Cretaceous											
Albian	*Cedar Mountain Formation*										
	UCM-264-6-1	2	35.959	0.2	-0.216	0.006	1.0380	-1.922	1.2	-0.087	0.017
	UCM-264-6-2	2	33.826	0.0	-0.275	0.002	1.0380	-3.977	1.2	-0.146	0.017
	UCM-264-6-3	2	35.525	0.1	-0.209	0.001	1.0380	-2.340	1.2	-0.080	0.017
	UCM-861-1	2	30.490	0.5	-0.164	0.005	1.0380	-7.191	1.2	-0.035	0.017
	UCM-861-2	2	35.639	0.5	-0.263	0.001	1.0380	-2.231	1.2	-0.135	0.017
	UCM-861-3	2	32.891	0.6	-0.207	0.001	1.0380	-4.878	1.2	-0.078	0.017
	UCM-157-1	2	32.435	0.0	-0.209	0.002	1.0380	-5.317	1.2	-0.080	0.017
	UCM-157-2	2	32.629	0.6	-0.211	0.002	1.0380	-5.130	1.2	-0.082	0.017
	UCM-157-3	2	33.179	0.0	-0.216	0.004	1.0380	-4.601	1.2	-0.087	0.017

Table 3-2 (continued)

Time	Sample ID	N[a]	Measured values				^{18}a[d] ($CaCO_3$–H_2O)	Measured values			
			$d^{18}O_c$[b]	1s [c]	$D^{17}O_c$[b]	1s [c]		$d^{18}O_c$[b]	1s [c]	$D^{17}O_c$[b]	±[e]
Albian	*Xinminpu Group*										
(continued)	G140616-A	2	29.490	0.3	-0.157	0.002	1.0380	-8.155	1.2	-0.028	0.017
Late Jurassic											
Oxfordian	*Morrison Formation*										
	UCM-418-1	2	35.113	0.3	-0.380	0.011	1.0380	-2.737	1.2	-0.252	0.017
	UCM-418-2	2	33.143	1.0	-0.403	0.010	1.0380	-4.635	1.2	-0.274	0.017
	UCM-418-3	2	34.813	0.9	-0.369	0.007	1.0380	-3.026	1.2	-0.240	0.017
	UCM-418-4	2	35.179	0.7	-0.396	0.010	1.0380	-2.674	1.2	-0.267	0.017
	UCM-532-1-1	2	35.287	0.1	-0.401	0.001	1.0380	-2.570	1.2	-0.273	0.017
	UCM-532-1-2	2	31.190	0.2	-0.343	0.004	1.0380	-6.516	1.2	-0.214	0.017
	UCM-532-1-3	2	31.533	0.4	-0.364	0.005	1.0380	-6.187	1.2	-0.235	0.017
	UCM-532-1-4	2	34.837	0.1	-0.368	0.011	1.0380	-3.003	1.2	-0.239	0.017
	UCM-656-1	2	35.644	0.7	-0.372	0.003	1.0380	-2.226	1.2	-0.243	0.017
	UCM-656-2	2	33.331	0.3	-0.309	0.015	1.0380	-4.454	1.2	-0.180	0.017
	UCM-656-3	2	35.356	0.3	-0.402	0.003	1.0380	-2.503	1.2	-0.273	0.017

a. Number of triple oxygen isotope analyses. Procedures are described in Section 2.3.

b. $\delta^{18}O_c$ and $\Delta^{17}O_c$ are isotopic compositions of O_2 generated from carbonate samples; $\delta^{18}O_w$ and $\Delta'^{17}O_w$ are calculated parent water oxygen isotope compositions. Values are first normalized to VMOW-SLAP scale (Schoenemann et al., 2013), and then normalized to known $\delta^{18}O$ values of carbonates standards (Passey et al., 2014).

c. Values are 1σ (n = 3), or the absolute per mil differences between pairs of analyses (n = 2).

d. Assuming dinosaurs body temperature is ~ 38-40 °C, fractionation factor for fossil eggshell carbonates is 1.0380, a combined mineral-water and acid digestion fractionation as determined by (Passey et al., 2014).

e. Values are based on standard error propagation using the 95% confidence intervals error reported in Passey et al. (2014) for $^{18}\alpha_{CaCO_3\text{-}H_2O}$=1.0380±0.0008 and $\lambda_{CaCO_3\text{-}H_2O}$ = 0.5245±0.0003. Observed average external precision for $\delta^{18}O_c$ and $\Delta'^{17}O_c$ measurements from February 2013 to August 2015 are 0.6‰ (1σ) and 0.011‰ (1σ). Then, errors used in the propagations are 1.96 × S.E.M, where S.E.M. are generic errors. S.E.M. = average external precision/$\sqrt{N}$ (N is number of analyses).

f. Calculated using $\Delta'^{17}O_w = \Delta'^{17}O_c + 10^3 \ln^{18}\alpha_{CaCO_3\text{–}H_2O} \times (0.528 - \lambda_{CaCO_3\text{–}H_2O})$, where $\lambda_{CaCO_3\text{–}H_2O}$ is 0.5245 for all samples.

General observations include: (1) almost all the dinosaur body water compositions are lower in $\Delta'^{17}O$ values than meteoric waters ($\Delta'^{17}O_{mw}$: ~ –0.01‰ - 0.05‰, Fig. 3-1), an expected pattern related to the influence of evaporated water and low $\Delta'^{17}O$ input from atmospheric O_2; (2) there is typically a large range in $\Delta'^{17}O$ values within each age-locality group of samples, indicating that different dinosaurs species (or individuals within species) may have had different physiologies and behaviors, or that they experienced different environmental conditions; and (3) Cretaceous samples have similar or slightly lower body water $\Delta'^{17}O$ values relative to modern samples, while Late Jurassic samples have significantly lower body water $\Delta'^{17}O$ values relative to modern samples. Two samples from the Campanian-age Djadokhta Formation (Bayn Dzak locality), and the entire group of samples from Oxfordian-age Morrison Formation, lie well outside of the $\Delta'^{17}O_{bw}$ range of modern animals (Fig. 3-2c, f and Fig. 3-3). The two Bayn Dzak samples with low $\Delta'^{17}O_{bw}$ values are outliers compared to all the other Campanian samples, whereas the Morrison Formation samples cluster together.

Taxon-specific partitioning of $\Delta'^{17}O_{bw}$ is observed in the dinosaur samples from Two Medicine Formation, Montana (Fig. 3-2c). The fossil samples are identified as *Troodon* (Troodontidae) and *Maiasaura* (Hadrosauridae) (Chin, 2007). *Troodon* is generally thought to have preyed on small mammals, dinosaur eggs and dinosaur hatchlings, and possibly insects, although omnivory has also been suggested for *Troodon* on the basis of the pattern of tooth serrations (Holtz Jr et al., 1998). *Maiasaura* is interpreted as a herbivore, possibly consuming poor-quality, high fiber vegetation (Chin, 2007). For the other localities, there is generally insufficient taxonomic identification of the eggshell samples to permit an evaluation of taxon-specific isotope partitioning.

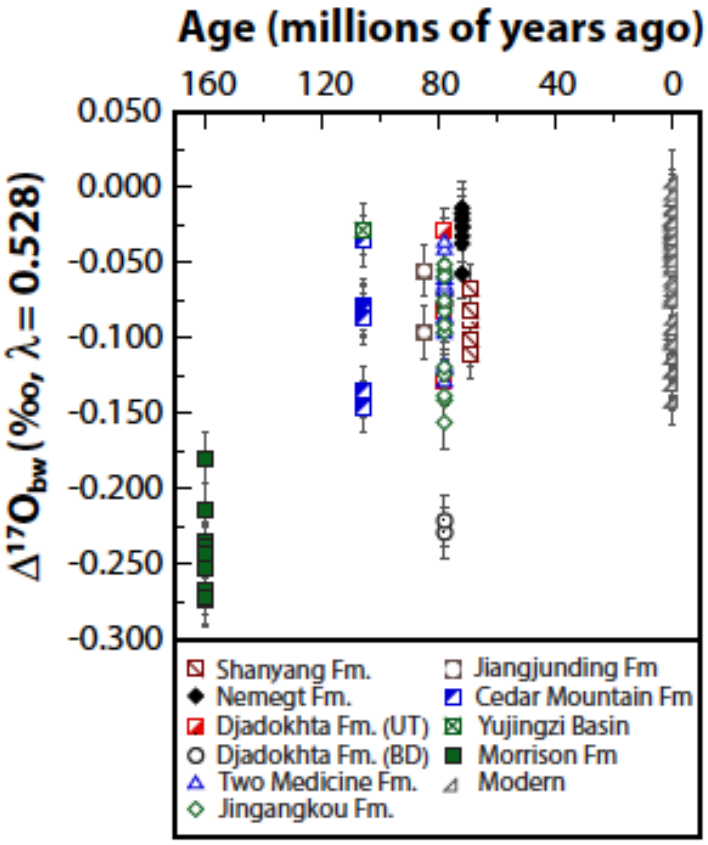

Figure 3-3. The $\Delta'^{17}O$ dinosaur body record for Late Jurassic through Late Cretaceous, and comparisons to the $\Delta'^{17}O$ of modern animal body water.

3.3.2. Preservation of samples

Electron backscatter diffraction (EBSD), X-ray Diffraction (XRD) and energy-dispersive spectrometry (EDS) results indicate good preservation for most of the Cretaceous samples, but poor preservation for some of the Late Jurassic samples (Fig. A3.2). EBSD is capable of detecting loss of primary crystallographic orientation, presence of secondary mineralization, and recrystallization (Pérez-Huerta et al., 2007; Cusack et al., 2008; Pérez-Huerta et al., 2012). For well-preserved samples, the crystallographic characteristics were broadly comparable to modern ostrich eggshell

calcite. Observed diagenetic features include patchy dolomitization of several Cretaceous samples and heavy silicification for some Late Jurassic samples. Open-system digenesis should elevate $\Delta'^{17}O$ of biominerals towards $\Delta'^{17}O$ of meteoric water (Gehler et al., 2011), so anomalous body water $\Delta'^{17}O$ values (lower than the observed range of $\Delta'^{17}O$ for meteoric water, Fig. A3.3) indicate at least partial preservation of original biogenic signal. For instance, the reconstructed $\Delta'^{17}O$ values of Ukhaa Tolgod dinosaur body water are lower than the surface waters reconstructed from the eggshell associated soil carbonates (Fig. A3.3, Table A2.3). In other words, the Ukhaa Tolgod samples are either unaltered (isotopically), or at least not totally altered. Thus measured $\Delta'^{17}O$ values place upper limits on primary $\Delta'^{17}O$ values. Although EBSD results indicate the Morrison formation samples are partially altered, the significantly lower $\Delta'^{17}O$ values we observed in fossil eggshell carbonates indicate that the fossil samples are not totally altered and the original $\Delta'^{17}O$ values in fossil eggshells may have been even lower than the observed values.

Clumped isotopes and $\Delta'^{17}O$ can be used as two independent proxies to evaluate the preservation of fossil samples. Unlike $\Delta'^{17}O$, clumped isotopes are sensitive to both open system diagenesis (high water/rock ratio) and closed system digenesis (rock/water $\rightarrow \infty$). Clumped isotopes record the temperature of mineralization, be it primary mineralization in the living animal (at body temperature), or secondary mineralization during diagenesis. Purely closed system diagenesis is capable of changing isotopic clumping, but has no influence on bulk isotopic composition such as $\Delta'^{17}O$ because all of the diagenetic oxygen originates from the sample itself (Ferry et al., 2011; Huntington et al., 2011). We can examine isotopic alteration of samples based on the difference

between observed clumped isotope temperatures and plausible body temperatures (Fig. A3.3). Almost all of the Late Jurassic samples show very high clumped isotope temperatures and hence have experienced a degree of digenesis. The fact that these samples preserve highly anomalous $\Delta'^{17}O$ and elevated clumped isotope temperatures is consistent with closed system diagenesis, but does not rule out a contribution of open-system diagenesis (which would tend to elevate $\Delta'^{17}O$ above original values). The Mongolia samples record clumped isotope temperatures that are plausible as body temperatures (~22 – 37 °C). The low body temperatures we observed in these Mongolia dinosaurs are consistent with the low body temperatures reported by Eagle et al. (2015) based on clumped isotope compositions of eggshells from the same localities. These results are consistent with, but do not prove, essentially no isotopic diagenesis in terms of clumping and bulk isotopic composition.

In summary, many of the samples have experienced significant diagenesis, and diagenesis cannot be entirely ruled out for any of the samples. However, the extent to which this diagenesis affected $\Delta'^{17}O$ values less certain, and all samples preserve $\Delta'^{17}O$ values that are lower than typical meteoric water values, suggesting that they preserve at least part of their original $\Delta'^{17}O$ signals. Accordingly, the fossil $\Delta'^{17}O$ values should be interpreted as placing upper limits on primary $\Delta'^{17}O$ values. As will become clear later in this paper, this translates to the fossil $\Delta'^{17}O$ values placing lower limits on estimates of past pCO_2.

3.4. RECONSTRUCTION OF PALEO-CARBON-CYCLING

3.4.1. $\Delta'^{17}O(O_2)$ reconstruction using the environmental physiology isotope concordance approach

The triple oxygen isotope body water model developed in Chapter 2 illustrates that isotopic compositions of animal body water are influenced by climate, animal physiology and diet. Chapter 2 used MAX-EVAP and MIN-EVAP models to evaluate body water $\Delta'^{17}O$ endmembers of modern animals and suggested an increasing range in $\Delta'^{17}O$ of body water from humid to arid climates (see Fig. 2-9 of Chapter 2). Variations in climate and physiology can lead to as large as ~0.20‰ differences in $\Delta'^{17}O_{bw}$. Using this approach, we develop specific endmember models and a mean model to evaluate the variations in dinosaur body water $\Delta'^{17}O$ values with different atmospheric O_2 $\Delta'^{17}O$ values. These endmembers are a key aspect of the 'environmental physiology isotope concordance' (EPIC) approach for identifying the range of $\Delta'^{17}O(O_2)$ values that are concordant with observed $\Delta'^{17}O_{bw}$ values.

The endmember models we use in this study consider extreme environmental and physiological conditions in order to model the maximum and minimum possible $\Delta'^{17}O$ values of dinosaur body water under any given $\Delta'^{17}O(O_2)$ value. Relative humidity (rh), free water content in food ($f_{H_2O\text{-in-food}}$), fraction of ingested leaf water relative to total ingested food water [$r_{l/s}$ = leaf/(leaf+stem)] and water economy index (WEI) are the four most important parameters in regulating animal body water compositions when source water isotopic compositions are fixed. Where possible, we use dinosaur-specific physiological parameters, for example sweat/(sweat + pant) = 0 (because dinosaurs almost certainly did not sweat; (Bakker, 1971; Paladino et al., 1990; Barrick et al., 1996).

The $\delta^{18}O_{mw}$ input for all dinosaur models is fixed at -15.0‰, a value reflective of the mid- to high latitude and continental nature of many of the sample localities (we note that $\Delta'^{17}O$(body water) is relatively insensitive to $\delta^{18}O_{mw}$, with a 10‰ change in $\delta^{18}O_{mw}$ leading to < 0.01‰ change in $\Delta'^{17}O$ of body water). Using such parameters, we present revised 'MAX- and MIN-EVAP' models, termed MAX-EVAP-2 and MIN-EVAP-2, which are based on extension of the limits of climatic and physiological parameters of the body water model. The model parameters are listed in Table 3-3. As will become more apparent below, extending these limits has the effect of enlarging the error bars on our estimates of $\Delta'^{17}O(O_2)$, meaning that our estimated error in $\Delta'^{17}O(O_2)$ is more conservative. The MAX-EVAP-2 model, giving the lower $\Delta'^{17}O_{bw}$ limit, represents evaporation sensitive dinosaurs with low WEI values living in extremely arid climates (rh = 0.1), and ingesting high water content leaves instead of stems. The MIN-EVAP-2 model, giving the upper $\Delta'^{17}O_{bw}$ limit, represents evaporation insensitive dinosaurs with high WEI values living in extremely humid climates (rh = 0.9) and ingesting low water content stems instead of leaves. These two models should bracket the possible maximum and minimum $\Delta'^{17}O_{bw}$ values for dinosaurs.

We then model the response of $\Delta'^{17}O_{bw}$ to $\Delta'^{17}O(O_2)$ for both the MIN-EVAP-2 (high $\Delta'^{17}O_{bw}$ limit) and the MAX-EVAP-2 models (low $\Delta'^{17}O_{bw}$ limit). For each model, we obtain a unique slope and intercept for the $\Delta'^{17}O_{bw}$ - $\Delta'^{17}O(O_2)$ relationship (slopes and intercepts are given in Table 3-3). These response curves, to the extent that the models are accurate, will bracket the total $\Delta'^{17}O_{bw}$ range in nonaquatic terrestrial animal body water for any given $\Delta'^{17}O(O_2)$ value (Fig. 3-4a).

Table 3-3. Body water model parameters for MIN-EVAP-2, MAX-EVAP-2 and MEAN model.

Parameters[a]	Values		
	MAX-EVAP-2	MIN-EVAP-2	MEAN
Animal Specific Parameters			
Mass (kg) [b]	40	40	40
Metabolic pre-exponent	2.955	2.955	2.955
Metabolic exponent	0.727	0.727	0.727
Oxygen conversion factor (mole/kJ)	2.16×10^{-3}	2.16×10^{-3}	2.16×10^{-3}
Water economy index (WEI, ml/kJ) [c]	0.05	0.60	0.25
Fecal H_2O content (fraction of total mass)	0.6	0.6	0.6
Sweat/(sweat+pant) ratio (thermoregulation type)	0.0	0.0	0.0
Fraction of O_2 used (fraction of inhaled O_2)	0.2	0.2	0.2
Z_value [d]	10.5	10.5	10.5
Body Temperature (K) [e]	311.15	311.15	311.15
Environmental Parameters			
Relative humidity (rh)	0.1	0.9	0.5
Environmental temperature (K)	288.15	288.15	288.15
Meteoric water $d^{18}O$	–15.0‰	–15.0‰	–15.0‰
Meteoric water $\Delta'^{17}O$	0.010‰	0.035‰	0.020‰
Atmospheric O_2 $d^{18}O$	23.5‰	23.5‰	23.5‰
Atmospheric O_2 $\Delta'^{17}O$	Variable: from –5.000‰ to –0.100‰		
Food Parameters *(fractional)*			
Relative Digestibility	0.8	0.8	0.8
Energy extraction efficiency	0.9	0.9	0.9
Food carbohydrate content	0.85	0.85	0.85
Food fat content	0.05	0.05	0.05
Food protein content	0.10	0.10	0.10
Food associated free H_2O content	0.70	0.40	0.55
Plant/(Plant+Meat) ratio	1.0	1.0	1.0
Leaf/(stem+leaf) ratio (fraction of total ingested food water)	0.9	0.1	0.5
Model outputs: $\mathbf{\Delta'^{17}O_{bw} = A \times \Delta'^{17}O(O_2) + B}$ [f]			
A	0.2784	0.1167	0.2414
B	–0.0481	0.0657	0.0460

a. Animal specific and food parameters are from Kohn (1996) if not specified.
b. Estimated from ostrich. Influences of mass on $\Delta'^{17}O_{bw}$ are negligible (Chapter 2).
c. Possible WEI range is based on the study of Nagy and Peterson (1988) and Nagy (2004).
d. Z-value = [$\delta^{18}O$ (exhaled O_2) – 23.5]/ (Fraction of O_2 used) (Kohn, 1996)
e. Assuming dinosaur body water temperature is 38 °C. Body temperature is not a major factor in regulating $\Delta'^{17}O_{bw}$.
f. Based on this equation, $\Delta'^{17}O(O_2)$ can be calculated for any given $\Delta'^{17}O_{bw}$.

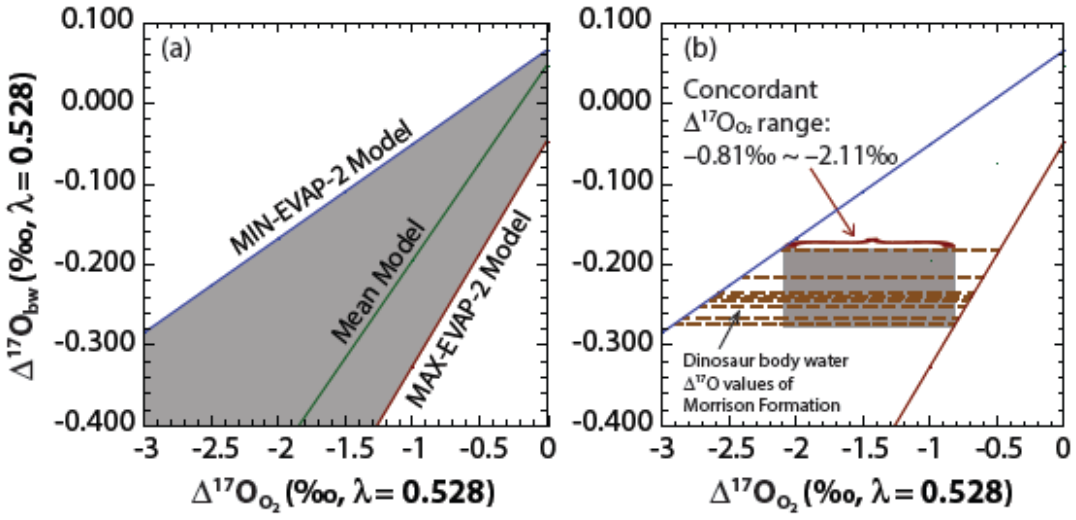

Figure 3-4. $\Delta'^{17}O_{bw} - \Delta'^{17}O(O_2)$ response curves for $\Delta'^{17}O(O_2)$ reconstructions. (a) Response curves from the MAX-EVAP-2 (red line), the MIN-EVAP-2 (blue line) and the MEAN (green line) model. Grey shadowed area includes all possible $\Delta'^{17}O$ values of body water for any given $\Delta'^{17}O$ of atmospheric O_2. (b) Reconstructing $\Delta'^{17}O(O_2)$ using the Morrison Formation samples as an example. We use the 'EPIC' concordance method to infer the range of reconstructed $\Delta'^{17}O(O_2)$ consistent with the $\Delta'^{17}O_{bw}$ values of all samples. That is, for all observations of $\Delta'^{17}O_{bw}$ of the same group, there should be one single range of $\Delta'^{17}O(O_2)$ that account for all samples.

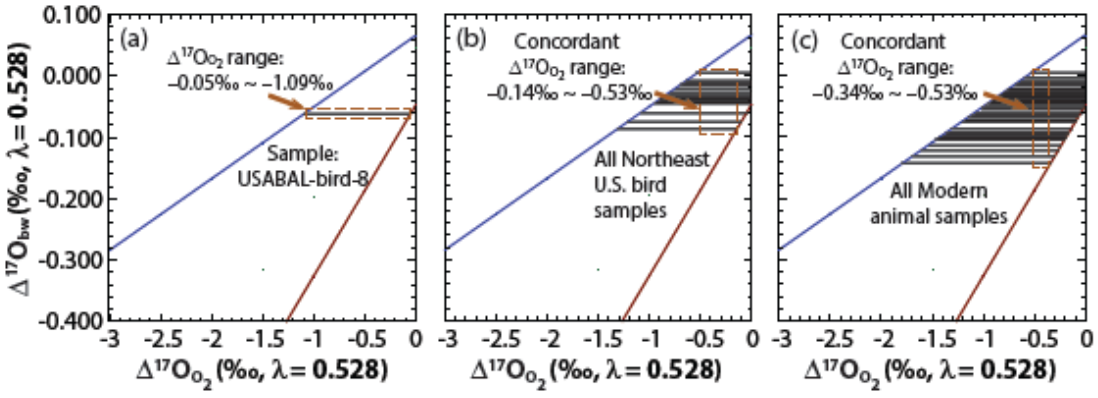

Figure 3-5. Illustration of the EPIC method for constraining the possible range of $\Delta'^{17}O(O_2)$, using modern samples. (a) $\Delta'^{17}O(O_2)$ range predicted from one specimen (sample: USABAL-bird-8). (b) A further

constrained $\Delta'^{17}O(O_2)$ range predicted from all northeast U.S. bird samples. (c) A very narrowly constrained $\Delta'^{17}O(O_2)$ range predicted from all modern animal samples.

The concordance aspect of the approach is carried out by examining animal $\Delta'^{17}O_{bw}$ values in the context of these response curves. For any given $\Delta'^{17}O_{bw}$ value, the two curves bracket the range of $\Delta'^{17}O(O_2)$ values that could have existed during the lifetime of the animal. In plotting all observed $\Delta'^{17}O_{bw}$ values for a single fossil locality (that is, a single time-location instance), there should be one single $\Delta'^{17}O(O_2)$ range that is accounts for all of the observations (Fig. 3-4b, using Morrison Formation samples as example). This range is the concordant $\Delta'^{17}O(O_2)$ range for the time period in question. This range will be minimized (= error in reconstructed $\Delta'^{17}O(O_2)$ is minimized) when the analyzed samples span the full range of animal physiologies and climatic conditions for a given time period. Modern samples in Chapter 2 are of various physiologies and from different climatic conditions, which are ideal for illustrating how the EPIC method constrains $\Delta'^{17}O(O_2)$ ranges. A single wild bird sample from northeast U.S. gives a possible $\Delta'^{17}O(O_2)$ range of –0.05‰ - –1.09‰ (Fig. 3-5a), whereas this wide range will be narrowed down to –0.14‰ - –0.53‰ when taking all northeast U.S. birds into consideration (Fig. 3-5b), and finally to –0.34‰ - –0.53‰ when including all modern samples (Fig. 3-5c). In Figure 3-5, we can see that the highest $\Delta'^{17}O(O_2)$ value is constrained by the sample of lowest $\Delta'^{17}O_{bw}$ value, and vice versa. Hence, the reconstructed $\Delta'^{17}O(O_2)$ range will be most precise when the collection of fossil samples cover the whole range of $\Delta'^{17}O_{bw}$ for a given time instance. Undersampling of coetaneous animals (which is generally the case for each time instance in our study), will lead to a less well constrained range of $\Delta'^{17}O(O_2)$. However, this range is still robust as it brackets

the 'real' $\Delta'^{17}O(O_2)$ value.This is the advantage of using the EPIC method in reconstructing $\Delta'^{17}O(O_2)$ values relative to commonly-used 'mean value + error bars' method. It directly constrains possible $\Delta'^{17}O(O_2)$ values into a reliable range, which can be further minimized with additional sampling. Table 3-4 shows our estimates of the $\Delta'^{17}O(O_2)$ range for each group of samples from Late Jurassic to Late Cretaceous based on the EPIC approach.

A set of samples may be said to be 'discordant' when there is no single $\Delta'^{17}O(O_2)$ value that is consistent with all observed $\Delta'^{17}O_{bw}$ values at a given fossil locality. Such discordance might arise from isotopic diagenesis of fossil samples, from diachroneity of the fossil assemblage (i.e., different individuals represented in the assemblage lived during different time intervals with different $\Delta'^{17}O(O_2)$ values), or inappropriateness of the body water models for the particular organisms in question (for example, if there are gross errors in our model, or if some of the organisms were fully aquatic such as fish, and hence not represented by our model).

For comparison, we also present estimates of $\Delta'^{17}O(O_2)$ using a MEAN body water model representing moderate climate and intermediate physiology and behavior. Similarly, we obtain a relationship between $\Delta'^{17}O_{bw}$ and $\Delta'^{17}O(O_2)$ for the MEAN model that lies between the MAX-EVAP-2 and MIN-EVAP-2 relationships (Table 3-3, Fig. 3-4a). Then, using the average $\Delta'^{17}O_{bw}$ value for each group of samples, we can reconstruct "mean" $\Delta'^{17}O(O_2)$ values for each time interval (Table 3-4).

Table 3-4. Reconstructed $\Delta'^{17}O(O_2)$ values (‰), and pCO_2 (ppm) when assuming $GPP_t/GPP_0 = 1$.

Age	Formation/Location	EPIC method (Using MAX-EVAP-2 & MIN-EVAP-2 model)				Mean Model	
		MAX-EVAP-2 model $\Delta'^{17}O(O_2)$	MIN-EVAP-2 model $\Delta'^{17}O(O_2)$	Min pCO_2	Max pCO_2	$\Delta'^{17}O(O_2)$	pCO_2
Modern	Various	–0.34	–0.53	170	390	–0.43	280
Mastrichtian	Shanyang Formation	–0.22	–1.14	43	1102	–0.56	429
Maastrichtian/Campanian	Nemegt Formation, Bugin Tsav	–0.03	–0.68	0	560	–0.31	140
Campanian	Djadokhta Formation, Ukhaa Tolgod	–0.29	–0.80	120	710	–0.57	440
	Djadokhta Formation, Bayn Dzak	–0.65	–1.16	530	1130	–0.81	710
	Two Medicine Formation	–0.29	–0.87	110	780	–0.53	390
	Jingangkou Formation	–0.39	–1.00	230	940	–0.60	470
Santonian	Jiangjunding Formation	–0.17	–1.04	0	980	–0.50	360
Albian	Cedar Mountain Fm. & Xinminpu Group	–0.35	–0.80	190	710	–0.54	400
Oxfordian	Morrison Formation	–0.81	–2.11	710	2280	–1.20	1180

3.4.2. $\Delta'^{17}O$ budget model

Once $\Delta'^{17}O$ values of atmospheric O_2 are reconstructed, we need a model of $\Delta'^{17}O(O_2) - pCO_2 - GPP$ to infer characteristics of past carbon cycling. Recently, Cao and Bao (2013) and Young et al. (2014) modeled the budget of $\Delta'^{17}O$ of atmospheric O_2 by considering the influences from GPP, O_2/CO_2 ratio, stratospheric chemistry, stratospheric-troposphere dynamics, and other factors. Generally, a dominant origin of non-zero $\Delta'^{17}O$ values in the atmosphere is the mass independent O_3–CO_2–O_2 photochemical reactions in the stratosphere. The relevant photochemical reactions in the stratosphere have been investigated theoretically and experimentally, and fundamental reactions for generating ^{17}O-anomalies include:

$$O_3 + h\nu \rightarrow O(^1D) + O_2, \qquad O(^1D) + CO_2 \rightarrow CO_3^*;$$
$$CO_3^* \rightarrow CO_2 + O(^3P), \qquad O(^3P) + O_2 \xrightarrow{M} O_3$$

These processes ultimately produce ^{17}O-enriched O_3 and CO_2 ($\Delta'^{17}O > 0$), and ^{17}O-depleted O_2 ($\Delta'^{17}O < 0$) (Yung et al., 1997; Luz et al., 1999; Bao et al., 2008; Cao and Bao, 2013; Young et al., 2014). After transport into the troposphere, the isotopically anomalous CO_2 and O_2 exchange oxygen with the effectively infinite reservoir of the hydrosphere, a process driven by photosynthesis and respiration. Although the isotopically anomalous O_2 is consumed by respiration and replaced by isotopically normal O_2 from photosynthesis, this flux is relatively small compared with the stratospheric production. Additionally, atmospheric O_2 has a longer residence time (~1200 yrs., Bender et al. (1994)) than CO_2 (5-15 yr., Essenhigh (2009)). Thus the negative ^{17}O anomaly of O_2 accumulates and eventually stabilizes when the negative

$\Delta'^{17}O$ flux carried by O_2 to the hydrosphere matches the positive $\Delta'^{17}O$ flux carried by CO_2.

Table 3-5. Parameters in $\Delta'^{17}O(O_2)$ budget model

Parameter	Value	Comment
pCO_2 [a]	Variable	*e.g.* Pre-industrial pCO_2 = 280 ppm
pO_2 [b]	0.21 bar (4.15×10^{19} mole)	Present day pO_2 Moles of O_2 = 0.21 × total moles of atmosphere = $0.21 \times 1.98 \times 10^{20}$ mole (Young et al., 2014)
GPP [c]	3.43×10^{16} mole O_2 a^{-1}	Present day GPP = gross marine productivity + gross terrestrial productivity (Blunier et al., 2012)
ρ	pO_2/pCO_2	O_2/CO_2 ratio
τ	O_2/GPP	= Moles of O_2/GPP
$\Phi(\rho)$ [d]	$(1.039 - \lambda) \times \delta^{18}O_{CO_2\text{-}O_2} - 1.1738$	l = 0.52 (Cao and Bao, 2013)
$\delta^{18}O_{CO_2\text{-}O_2}$	$(64 + 146 \times (\rho/1.23))/(1 + \rho/1.23)$	Shaheen et al. (2007)
θ [e]	0.0170	Fixed in our model
γ [e]	0.1321	Fixed in our model
$\delta^{18}O_{Atm\text{-}O_2}$	23.5‰	Assumed $d^{18}O$ value of atmospheric O_2

a. pCO_2 is variable in the model to generate different $\Delta'^{17}O(O_2)$ values.
b. pO_2 is fixed at present day value as it has little influence on $\Delta'^{17}O$ (O_2) when pCO_2/GPP is not high. Total moles of atmospheric gas from Young et al. (2014).
c. Total gross primary productivities of ocean and terrestrial biosphere (Blunier et al. 2012).
d. Relationship taken from Cao and Bao (2013) using a reference scheme of λ = 0.52. Readers can also refer to Cao and Bao (2013) for derivations of this relationship.
e. Values from Cao and Bao (2013).

Assuming a steady state $\Delta'^{17}O$ anomaly in the troposphere, the negative and positive magnitude of ^{17}O-anomalies depend on the balance of CO_2 and O_2 fluxes. Thus the anomaly magnitude in O_2 is strongly influenced by global primary productivity of biosphere (GPP). Consequently, the negative $\Delta'^{17}O$ anomaly in O_2 increases with increasing tropospheric pCO_2 and decreases with increasing GPP. In our study, we use the $\Delta'^{17}O$ model of Cao and Bao (2013) for paleoclimate reconstructions. Their $\Delta'^{17}O$ model at steady state is:

$$\Delta^{17}O_{O_2} = \frac{-\Phi(\rho)\gamma\theta\tau}{1+\rho+\gamma\theta\tau} \quad (2)$$

where $\Phi(\rho)$ is the difference of $\Delta'^{17}O$ between steady-state CO_2 and O_2 in O_2–CO_2–O_3 photochemical reaction, which is a function of ρ and $\delta^{18}O_{CO_2\text{-}O_2}$ (see Table 3-5 for equations), ρ is the ratio of pO_2/pCO_2, τ is the residence time of atmospheric O_2 ($\equiv pO_2/F_{GPP}$, and F_{GPP} is total rate of GPP including terrestrial and marine productivity); and γ and θ reflect the stratosphere–troposphere exchange rate and the mixing efficiency in the stratosphere, respectively. Values of all parameters in equation (2) are presented in Table 3-5. In the original model of Cao and Bao (2013), $\Delta'^{17}O$ values were calculated using a $\lambda_{ref} = 0.52$. We convert the output $\Delta'^{17}O$ values into the $\lambda_{ref} = 0.528$ reference scheme by assuming atmospheric $\delta^{18}O_{O_2} = 23.5‰$ ($\delta'^{18}O_{O_2} = 23.2‰$). For any given $\Delta'^{17}O(O_2)$ value ($\lambda_{ref} = 0.52$) from the original model, the corresponding $\delta'^{17}O$ of atmospheric O_2 can be calculated as $\delta'^{17}O_{O_2} = \Delta'^{17}O_{O_2} + 0.52 \times \delta'^{18}O_{O_2}$. Then, based on known $\delta'^{18}O_{O_2}$ and $\delta'^{17}O_{O_2}$ values, we can recalculate $\Delta'^{17}O(O_2)$ values in the $\lambda_{ref} = 0.528$ reference scheme based on equation (1). Thus, we have a $\lambda_{ref} = 0.528$ -based $\Delta'^{17}O(O_2)$ – pCO_2 – GPP relationship that suits our data. For any given $\Delta'^{17}O(O_2)$ values reconstructed from the MAX-EVAP-2, MIN-EVAP-2 and MEAN dinosaur body water model, we can interpret the pCO_2 and GPP combination during that time.

3.4.3. Paleo-carbon-cycling reconstructions

We will first discuss the pCO_2 reconstructions assuming GPP and pO_2 of the past (GPP_t, $pO_{2(t)}$) are the same as today (GPP_0, $pO_{2(0)}$), and then discuss the situation when GPP and pO_2 are not known.

3.4.3.1 pCO_2 reconstructions when $GPP_t = GPP_0$ and $pO_{2(t)} = pO_{2(0)}$

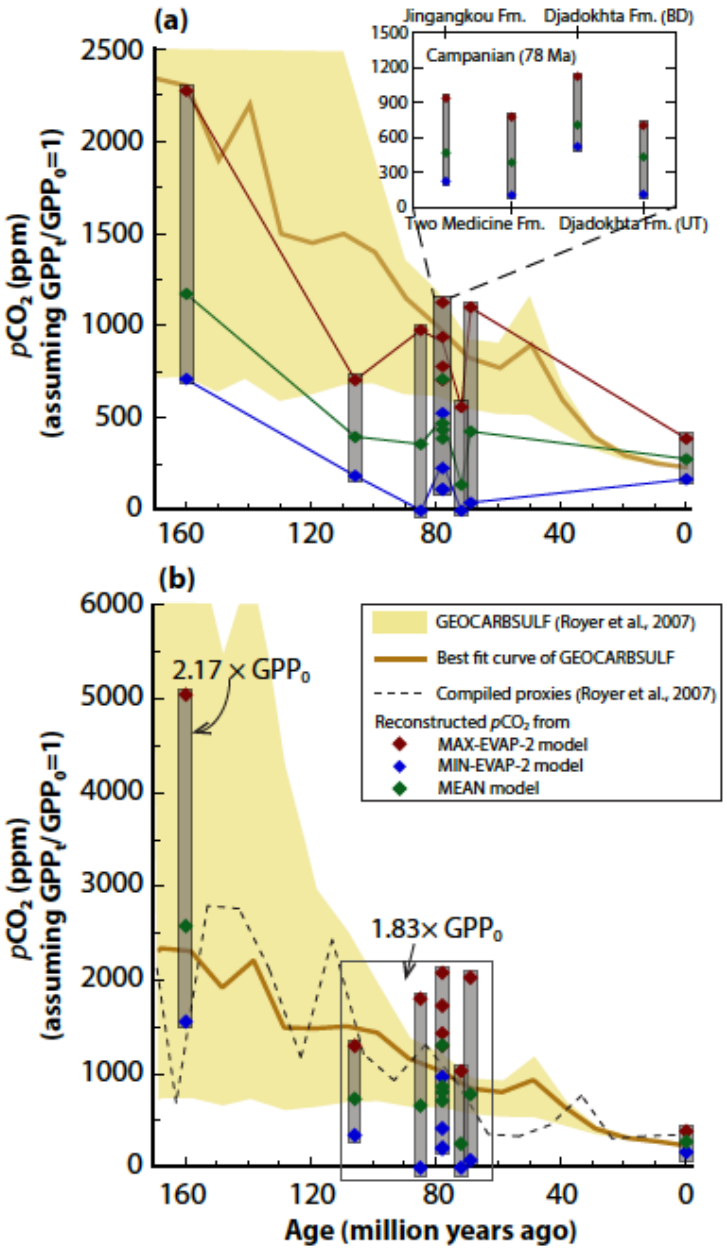

Figure 3-6. Reconstructed pCO_2. (a) pCO_2 when assuming GPP is the same as today, and comparisons with the GEOCARBSULF modeling result (Royer et al., 2007). The thick orange curve is the best fit of the GEOCARBSULF model suggested by Royer et al. (2007). Red, blue and green diamonds are pCO_2 calculated from MAX-EVAP-2, MIN-EVAP-2 and MEAN models, respectively. (b) Refined pCO_2 when taking variations of GPP into consideration. Based on the GPP estimates from Beerling (1999), all Cretaceous samples are remodeled with $GPP_t = 1.83 \times GPP_0$, and Late Jurassic samples with $GPP_t = 2.17 \times GPP_0$.

Our method can be used under the following assumptions to reconstruct pCO_2 of the past: the body water models are accurate, the GPP is the same as present, and the atmospheric $\Delta'^{17}O(O_2)$ was constant during the lifetimes of the eggshell-laying animals from each time-location group. We then use the estimated $\Delta'^{17}O(O_2)$ values in Table 3-4 and set $GGP_t/GPP_0=1$ in equation (2) to model pCO_2 for each group of samples. The pCO_2 estimates using this method are presented in Table 3-4 and Figure 3-6a. We reconstruct a modern pCO_2 range of 170 – 390 ppm from the MAX-EVAP-2 and MIN-EVAP-2 model, and an average value of 280 ppm from MEAN model. This result is consistent with the preindustrial pCO_2, and hence the preindustrial $\Delta'^{17}O(O_2)$ value, since atmospheric O_2 is dominantly "preindustrial" due to the long residence time of O_2 (Bender et al., 1994). We reconstruct similar or slightly elevated pCO_2 during the Cretaceous and a significantly elevated pCO_2 during the Late Jurassic. The general patterns of our reconstructed pCO_2 are similar to pCO_2 trends inferred from the GEOCARBSULF model of Royer et al. (2007). But our results suggest slightly lower pCO_2 during the Cretaceous relative to GEOCARBSULF model (Royer et al., 2007) under the assumption of $GGP_t/GPP_0=1$.

This method predicts pCO_2 in a very conservative way, because we extended the MAX-EVAP-2 and MIN-EVAP-2 models to extreme conditions, in order to represent endmembers of all possible dinosaur body water $\Delta'^{17}O$. The response curves of $\Delta'^{17}O_{bw}$ - $\Delta'^{17}O(O_2)$ from these two models consider uncertainties from variations in climate, physiology and diet. Actual pCO_2 values in the past were probably not lower than the values predicted from the MIN-EVAP-2 model, but could be higher than the values predicted from MAX-EVAP-2 if fossil samples were altered in $\Delta'^{17}O$. Even though our

method gives large uncertainty ranges in pCO_2, the range could be narrowed down when animal physiology, diet and environmental conditions are well sampled. This could be accomplished by targeting fossil localities with numerous specimens of numerous species, as well as by sampling from many fossil localities globally for each time interval. We also tested the sensitivities of pCO_2 to variations in $\Delta'^{17}O_{bw}$ and $\Delta'^{17}O(O_2)$ for the MEAN model. For every 0.10‰ decrease in $\Delta'^{17}O_{bw}$, the MEAN model predicts ~0.40‰ decrease in $\Delta'^{17}O(O_2)$, which will eventually cause ~480 ppm increase in pCO_2. As our high precision triple oxygen isotope measurements give an analytical precision of 0.01‰ for $\Delta'^{17}O$, this method could potentially resolve < 100 ppm changes in pCO_2. An interesting testpiece would be to apply this method to detect the pCO_2 variations between glacial and interglacial times.

3.4.3.2 GPP_t and pCO_2 constrains

In actuality, GPP and pO_2 have both varied over geological time. Here we discuss the sensitivity of reconstructed pCO_2 to these variables, and we then incorporate estimates of GPP from Earth system models to illustrate one way in which $\Delta'^{17}O$-based estimates of pCO_2 might be refined.

The model of Cao and Bao (2013) shows that $\Delta'^{17}O(O_2)$ becomes less negative with decreasing pO_2, but that the influence of pO_2 on predicting pCO_2 is minor when $\Delta'^{17}O(O_2)$ is not very negative or GPP and pCO_2 were not highly elevated. Figure 3-7 shows changes in both pCO_2 and GPP with half pO_2 using Two Medicine Formation (Late Cretaceous) and Morrison Formation (Late Jurassic) samples as an example. The pCO_2 – GPP curves are plotted based on the reconstructed $\Delta'^{17}O(O_2)$ values from the MEAN model and the $\Delta'^{17}O(O_2)$ budget model of Cao and Bao (2013). The Morrison

Formation samples point to a lower $\Delta'^{17}O(O_2)$ value and a steeper pCO_2 – GPP slope relative to Two Medicine samples. The influence of halving pO_2 is not as obvious for the Two Medicine pCO_2 – GPP curves within the plotted range. Even under extreme greenhouse conditions (high GPP and high pCO_2), halving pO_2 will not cause significant changes in final predictions of both GPP and pCO_2. The two pCO_2 – GPP curves of Morrison Formation deviate slightly more from each other when GPP and pCO_2 are both very high (Fig. 3-7). For instance, when $GPP_t = 5 \times GPP_0$, predicted pCO_2 will increase from 6120 ppm to 6460 ppm, about 6% change, with half pO_2. The influences of pO_2 will be more significant under extreme high GPP and pCO_2 conditions or for excessively steeper pCO_2 – GPP curves (that is, anomalously lower $\Delta'^{17}O(O_2)$ values). Under such conditions, pO_2 variations should not be overlooked when using $\Delta'^{17}O(O_2)$ to reconstruct pCO_2. The pO_2 reconstruction of Berner (1999) suggests that during the Mesozoic, pO_2 varied between ~ 20 vol.% to ~ 25 vol.%. Such varitions in pO_2 would have little effect on $\Delta'^{17}O$-based reconstructions of pCO_2 and GPP. Even though some other authors have suggested that pO_2 was half its current value during parts of the Mesozoic (Falkowski et al., 2005; Berner, 2006; Tappert et al., 2013), reconstructed pCO_2 would increase less than 10% under half pO_2 when $pCO_2 < 10000$ ppm and $GPP < 8 \times GPP_0$. Besides, previous studies show Mesozoic pCO_2 was not very likely to exceed 7000 ppm (Royer et al. 2007), and hence for the purposes of this study we fix the pO_2 value at the modern value.

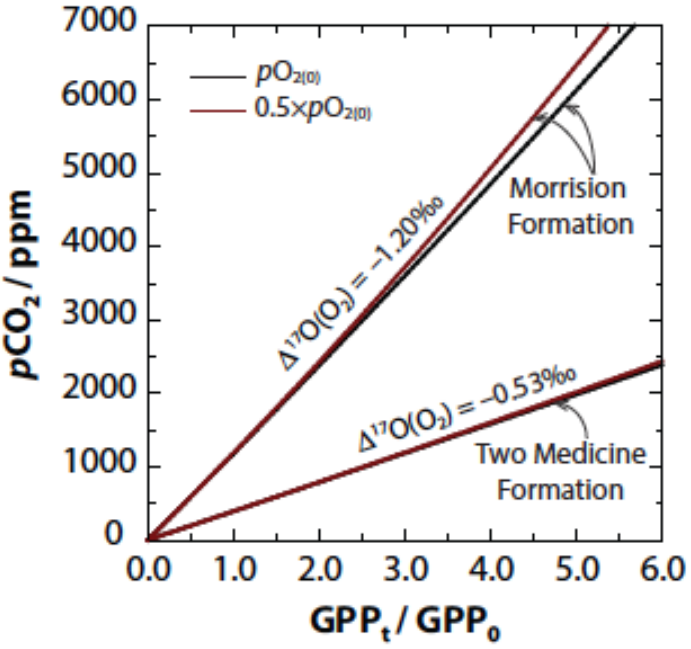

Figure 3-7. Influence of pO_2. The Δ'^{17} O(O_2) O(O_2) values along the curves are reconstructed $\Delta'^{17}O(O_2)$ values from the MEAN model for both Morrison Formation and Two Medicine Formation. We then model the pCO_2 – GPP curves based on the reconstructed $\Delta'^{17}O(O_2)$ values and the $\Delta'^{17}O(O_2)$ budget model of Cao and Bao (2013). Black curves are modeled using pO_2 of the present day value (0.210 bar), while red curves are modeled using half-present pO_2 (0.105 bar).In contrast, $\Delta'^{17}O(O_2)$ is very sensitive to changes in GPP. For a given $\Delta'^{17}O(O_2)$ value, the reconstructed pCO_2 value would approximately double per doubling of GPP (Luz et al., 1999; Blunier et al., 2002; Blunier et al., 2012; Cao and Bao, 2013; Young et al., 2014). This means we cannot separately constrain GPP and pCO_2 based only on reconstructed $\Delta'^{17}O(O_2)$ values. Earth system models are one approach for independently estimating GPP. In general terms, such models use past plate tectonic configurations and paleo GCMs to simulate past distributions of characteristic ecoregions (e.g., tropical evergreen forest, steppe, desert), and from these distributions estimate GPP. Beerling (1999) estimated global GPP during Late Jurassic and Mid-Cretaceous at ~2.17 and ~1.83 times present GPP. Figure 3-6b and Table 3-6 show the refined pCO_2 with these estimated GPP values.

Table 3-6. Refined pCO_2 with adjusted GPP. Cretaceous samples using $GPP_t = 1.83 \times GPP0$, and Jurassic samples using $GPP_t = 2.17 \times GPP_0$. Mean pCO_2 refers to the value derived from the Mean body water model, not the average of the Min and Max pCO_2 estimates.

Age	Formation/Location	Min pCO_2	Max pCO_2	Mean pCO_2
Modern	Various	170	390	280
Mastrichtian	Shanyang Formation	80	2030	790
Maastrichtian/Campanian	Nemegt Formation, Bugin Tsav	0	1030	260
Campanian	Djadokhta Formation, Ukhaa Tolgod	220	1300	810
	Djadokhta Formation, Bayn Dzak	970	2080	1310
	Two Medicine Formation	200	1440	720
	Jingangkou Formation	420	1730	870
Santonian	Jiangjunding Formation	0	1810	660
Albian	Cedar Mountain Fm. & Xinminpu Group	350	1300	740
Oxfordian	Morrison Formation	1560	5050	2580

However, Earth system models still have major uncertainties in predicting GPP of the deep past. Our work provides the relationship of GPP and pCO_2 that can be further used in Earth system models. From the model of Cao and Bao (2013), it can be shown that $\Delta'^{17}O(O_2)$ represents the ratio of GPP and pCO_2 when pO_2 is fixed. As discussed before, the reconstructed $\Delta'^{17}O(O_2)$ values therefore define unique curves on a plot of pCO_2 versus GPP (Fig. 3-8). The $\Delta'^{17}O(O_2)$ ranges reconstructed from the EPIC approach indicate similar or slightly different carbon cycling during Cretaceous, but significantly different carbon cycling during the Late Jurassic. Cretaceous samples indicate slightly lower or similar $\Delta'^{17}O(O_2)$, that is, pCO_2/GPP ratios that were similar to or slightly higher than present. This either means a similar carbon cycle to today, or the pCO_2 and GPP were both higher. The Late Jurassic samples have significantly lower $\Delta'^{17}O$ compared to today, indicating an anomalous pCO_2/GPP ratio. The ratio points to less vigorous carbon cycling (lower GPP) for any given pCO_2, a condition that could be referred to as a 'slow' carbon cycle. During Late Jurassic, the GPP and pCO_2 may both have been high, or they may both have been low. Either way suggests a fundamentally different carbon cycle during the Late Jurassic.

Overall, the best estimates for both GPP and pCO_2 can be achieved by combining our $\Delta'^{17}O(O_2)$ – pCO_2 –GPP predictions with other Earth system models. Since GPP estimates from Earth system models are not generally independent of the pCO_2 values specified in those models, a promising way forward would be to run Earth system models over a range of pCO_2 values. If GPP were calculated for each model run, this approach would allow construction of a model-based GPP - pCO_2 response curve (a model GPP sensitivity to pCO_2). Such curves could be overlain on the $\Delta'^{17}O(O_2)$-based GPP-pCO_2 relationship (i.e., Fig. 3-8), and the intersection of the curves may point to the most likely pCO_2 / GPP combination for the particular time interval.

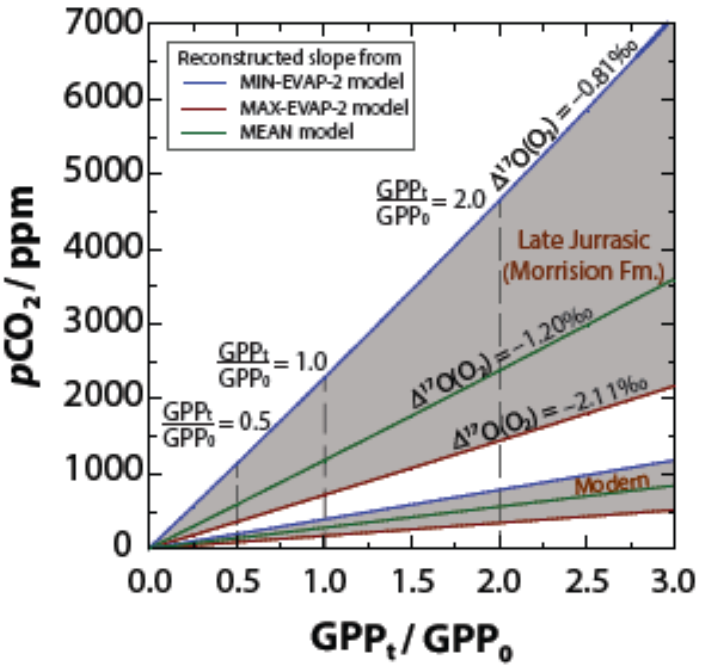

Figure 3-8. pCO_2 – GPP response range for modern and Morrison Formation times. Slopes of red, blue and green lines are calculated based on the $\Delta'^{17}O(O_2)$ values reconstructed from MAX-EVAP-2, MIN-EVAP-2 and MEAN models, respectively. The significantly different range indicates distinct carbon cycling during Late Jurassic relative to today.

3.5. CONCLUSIONS

$\Delta'^{17}O$ of dinosaur eggshells shows great potential for reconstructing paleo-carbon-cycling. The method is based on entirely different mechanisms than existing pCO_2 proxies, which makes it a valuable addition to the available toolbox for reconstructing past carbon cycling. Although there are large uncertainties in constraining pCO_2, the method has several unique features that distinguish it from other proxies. For instance, it should not lose sensitivity at high pCO_2 (a limitation of fossil leaf stomata-based approaches), and it should not produce 'false high CO_2' estimates (a limitation of the soil carbonate $\delta^{13}C$ method). It is possible that uncertainties could be continually reduced by the addition of $\Delta'^{17}O$ data from coeval fossil samples, and accuracy can be improved as we refine animal body water models, and models of the relationships among $\Delta'^{17}O(O_2)$, pCO_2, pO_2, and GPP.

Using the $\Delta'^{17}O$ method, we reconstruct similar to present (or slightly higher) pCO_2 during Cretaceous, and up to 1490 ± 780 ppm during Late Jurassic when assuming GPP was the same as today. Refined pCO_2 results are ~ 1× to 4× present pCO_2 for Cretaceous, and ~ 9× present pCO_2 for Late Jurassic after considering different GPP values during Mesozoic. These results are generally consistent with other studies and proxies in the general pattern of substantially higher pCO_2 for the early Mesozoic, and declining pCO_2 in the mid- and Late Mesozoic toward near-present values. Our results also constrain relationships between past pCO_2 and GPP, which may be further used in conjunction with Earth system models to permit a better understanding of past carbon cycle dynamics.

ACKNOWLEDGEMENTS

We thank Michael Bender and Kate Dennis for bringing to our attention the potential use of animal $\Delta'^{17}O$ to reconstruct past CO_2 levels. We thank Haoyuan Ji, Shuning Li and Dana Brenner for helping with sample analysis. We thank the donors of the American Chemical Society Petroleum Research Fund for partial support of this work.

APPENDIX A. SUPPLEMENTARY DATA

Supplementary data associated with this chapter (Table A3.1, Figure A3.2, and Figure A3.3) can be found in the appendices.

CHAPTER 4:CONCLUSION AND FUTURE RESEARCH

This dissertation describes a fundamental triple oxygen isotope body water model and a unique approach of using $\Delta'^{17}O$ for paleo-carbon-cycling reconstructions. This work was accomplished through extensively laboratory experiments and careful modelings. It should shed light on future applications of using triple oxygen isotopes in biominerals for paleoclimate studies.

The triple oxygen isotope body water model of Chapter 2 provides insights into the roles of physiological and environmental factors in regulating body water $\Delta'^{17}O$, and shows the potential of using $\Delta'^{17}O$ of body water as a proxy of paleoaridity and paleoecophysiology. Our observations suggest $\Delta'^{17}O$ of body water ($\Delta'^{17}O_{bw}$) is a good indicator of evaporation, and is strongly influenced by the relative proportions of evaporative water intake. $\Delta'^{17}O_{bw}$ is most sensitive to the effects of relative humidity, fraction of leaf water intake, free water content in food and the water economy index of an animal. We predict and also observe that a leaf-dependent animal of low WEI values should have lower $\Delta'^{17}O_{bw}$ values than a leaf-independent animal of high WEI values in the same area. We also modeled an increasing range in $\Delta'^{17}O_{bw}$ with decreasing relative humidity between leaf-dependent and leaf-independent animals. Besides, the model also predict ~ 5-30% oxygen of body water is from atmospheric O_2, which provides modeling support to the study of Chapter 3.

Chapter 3 presents an approach of using $\Delta'^{17}O$ of dinosaur body water to model the carbon cycling of the Mesozoic. The three essential elements of this method are: (1) $\Delta'^{17}O$ values of dinosaur body water calculated from analyzed $\Delta'^{17}O$ of dinosaurian eggshell carbonates, (2) the $\Delta'^{17}O_{bw} - \Delta'^{17}O(O_2)$ relationships modeled from the body

water model of Chapter 2, and (3) the $\Delta'^{17}O$ budget model of Cao and Bao (2013) to relates $\Delta'^{17}O(O_2)$ and pCO_2/GPP. Our results show similar to present or slightly higher pCO_2 during Cretaceous, and up to 1490±780 ppm of pCO_2 during Late Jurassic when assuming GPP is the same as today, but could also be much higher with higher GPP. Besides, the reconstructed $\Delta'^{17}O(O_2)$ values are of great potential in reconstructing the ratio of pCO_2 and GPP, which can be further used with Earth system models, as they could not constrain pCO_2 and GPP separately.

Our work is just a start of the triple oxygen isotope study in biominerals, but shows a promising future in this field. The most exciting application is to utilize the $\Delta'^{17}O(O_2) - pCO_2$ –GPP proxy to fossil vertebrates biominerals from any time period of interest. This work should not be limited to fossil eggshell carbonates and tooth enamel apatite. Even though dentin and bone are always strongly affected by diagenesis, first triple oxygen isotope analysis on these materials is also of great importance as fossil bone is more abundant compared to fossil tooth enamel. An interesting compliment research to this dissertation is to explore the full range of Mesozoic dinosaur body water $\Delta'^{17}O$ by analyzing vast numbers of fossil dinosaur eggshells, bones, tooth enamels and dentins. The trend of the lowest $\Delta'^{17}O$ values observed from each time period should be closely related to the pCO_2/GPP trend over Mesozoic. Similarly work can be done to any time of interest that might show distinct carbon cycling (*e.g.*, Paleocene-Eocene Thermal Maximum, Pleistocene glacial-interglacial cycles). Theoretically, our $\Delta'^{17}O$ proxy is able to resolve < 100 ppm changes in pCO_2, whether or not it is capable to distinguish pCO_2 variations during glacial-interglacial cycles is worth testing. Besides pCO_2/GPP reconstructions, the general predictions from the body water model, especially the

increasing $\Delta'^{17}O_{bw}$ trend with decreasing relative humidity, are also very useful in evaluating paleoaridity and animal paleoecophysiology. For instance, investigating triple oxygen isotope compositions of Holocene mammals could provide us information of local aridity, which is also closely related to human evolutions. Additionally, triple oxygen isotopes of sedimentary carbonates and nonvertebrate carbonates are another aspect of studies for this field. $\Delta'^{17}O$ of these carbonates directly reflect the $\Delta'^{17}O$ of the parent water. So low $\Delta'^{17}O$ values should indicate evaporative signals of the parent waters when these carbonates precipitated. This can be used to identify evaporated water bodies (*e.g.*, closed lakes) or to reconstruct paleo-ocean water isotope compositions. Finally, emerging high precision triple oxygen isotope analytical methods enable us to justify oxygen isotope fractionation exponents of different processes (e.g., CO_2-H_2O equilibrium process, H_2O-mineral exchange process). Theoretical studies have already anticipated the principle of the three oxygen isotope exchanges, but experimental data from high precision analysis including both $^{17}O/^{16}O$ and $^{18}O/^{16}O$ are still in great demand.

APPENDICES

A2.1. Summary for sensitivity test results of all parameters.

Table A2.1 Variations for all parameters in the model within realistic ranges of each parameter. *(see supplemental Excel files)*

A2.2 Sample information of data from Passey et al. (2014)

Table A2.2 Sample information and relative humidity data of samples from Passey et al. (2014)

Sample ID	Species/taxon/description	Location/Formation	Latitude	Longitude	Elevation	T (°C)[a]	Rh (%)[a]
Australian emu eggshell							
USA2013-Balbird-001	Unknown	Baltimore, USA	39.3	-76.6	50	12.2	61.9
USA2013-BALstarling-001	Starling, *Sturnus*	Baltimore, USA	39.3	-76.6	50	12.2	61.9
GON04-22-1.1	Ostrich, *Struthio camelus*	Gona, Ethiopia	11.1	40.3	775	26.2	66.6
ET05-AWSH-23	Ostrich, *Struthio camelus*	Aledege WP, Ethiopia	9.2	40.4	845	24.7	63.9
SA13M-007	Ostrich, *Struthio camelus*	Elandsfontein, South Africa	-33.1	18.2	80	16.8	72.2
OLGO4M-11	Ostrich, *Struthio camelus*	Olorgesaile, Kenya	-1.6	36.4	970	22.9	62.3
JHU-EGG-001	Chicken, *Gallus gallus*	Baltimore, USA	39.3	-76.6	50	12.2	61.9
JHU-EGG-002	Chicken, *Gallus gallus*	Baltimore, USA	39.3	-76.6	50	12.2	61.9
USA2013-BALchicken-003	Chicken, *Gallus gallus*	Baltimore, USA	39.3	-76.6	50	12.2	61.9
USA2013-BALchicken-004	Chicken, *Gallus gallus*	Baltimore, USA	39.3	-76.6	50	12.2	61.9
CHA2013-ZCChicken-001	Chicken, *Gallus gallus*	Zhucheng, China	36	119.4	79	12.4	67.4
JPN2013-OSChicken-001	Chicken, *Gallus gallus*	Osaka, Japan (?)	34.7	135.5	10	16.1	68.0
JHU-EGG-007	Duck, *Anas*	Baltimore, USA	41	-74.5	50	14.2	63.8
CHA2013-LYOstrich-001	Ostrich, *Struthio camelus*	Linyi, China	35.1	118.3	74	13.7	67.9
NJ-Ostrich-1	Ostrich, *Struthio camelus*	Northeastern USA	41	-74.5	160	9.1	66.2
USA2013-Njemu-001	Emu, *Dromaeus*	Northeastern USA	41	-74.5	160	9.1	66.2
K00-AB-303p4	Black rhino, Diceros bicornis	Aberdare NP, Kenya	-0.4	36.7	3350	10.9	72.2
K00-TSV-226	Hippopotamus, *H. amphibius*	Tsavo West NP, Kenya	-2.8	38.8	350	26.0	63.3

a. Climate data are from the CRU 2.0 gridded climate dataset (New et al., 2002). For Australian localities, temperature (T) and relative humidity (Rh) values are averages for the coolest four months of the year, which is the typical egg-laying season for Emu. For Baltimore localities, T and Rh are averages for March through May, the spring egg-laying season during which these samples were collected. For the Utah and Kenya localities (mammal samples), we use mean annual averages of T and Rh, in light of the long duration of tooth enamel mineralization and hence time-averaging of isotopic signals.

A2.3. Triple oxygen isotope data from Passey et al. (2014) and Pack et al. (2013)

Table A2.3. Triple oxygen isotope compositions eggshell carbonates, mammal tooth enamel apatite and diagenetic carbonates from Pack et al. (2013).

Sample ID	Species	N	Measured values				Body T[d]	$^{18}\alpha$[e]	Calculated values			
			$\delta^{18}O_c$[b]	±[c]	$\Delta'^{17}O_c$[b]	±[c]	°C	($CaCO_3$–H_2O)	$\delta^{18}O_w$[b]	±[f]	$\Delta'^{17}O_w$[b,g]	±[f]
Wild birdss eggshell from Passey et al. (2014)												
USA2013-Balbird-001	Unknown	2	38.993	1.1	-0.213	0.014	39	1.0380	1.742	1.2	-0.087	0.017
USA2013-BALstarling-001	Starling	2	35.643	0.6	-0.162	0.003	39	1.0380	-1.609	1.2	-0.036	0.017
GON04-22-1.1	Ostrich	3	44.948	0.7	-0.220	0.004	39	1.0380	7.696	1.0	-0.094	0.015
ET05-AWSH-23	Ostrich	3	46.002	1.3	-0.239	0.010	39	1.0380	8.751	1.5	-0.113	0.015
SA13M-007	Ostrich	2	47.131	0.9	-0.229	0.001	39	1.0380	9.880	1.2	-0.103	0.017
OLGO4M-11	Ostrich	2	44.089	0.9	-0.257	0.002	39	1.0380	6.838	1.1	-0.131	0.017
Captive bird eggshell from Passey et al. (2014)												
JHU-EGG-001	Chicken	3	34.001	0.7	-0.168	0.002	39	1.0380	-3.251	1.0	-0.041	0.015
JHU-EGG-002	Chicken	2	31.593	0.4	-0.160	0.012	39	1.0380	-5.659	1.1	-0.028	0.015
USA2013-BALchicken-003	Chicken	2	34.690	0.1	-0.160	0.005	39	1.0380	-2.561	1.1	-0.034	0.017
USA2013-BALchicken-004	Chicken	2	33.047	0.8	-0.139	0.005	39	1.0380	-4.205	1.1	-0.013	0.017
CHA2013-ZCChicken-001	Chicken	2	33.673	1.1	-0.174	0.011	39	1.0380	-3.578	1.3	-0.048	0.017
JPN2013-OSChicken-001	Chicken	2	32.213	0.2	-0.149	0.003	39	1.0380	-5.038	1.1	-0.023	0.017
JHU-EGG-007	Duck	2	31.093	0.2	-0.134	0.002	39	1.0380	-6.159	1.1	-0.008	0.017
CHA2013-LYOstrich-001	Ostrich	2	32.567	0.0	-0.130	0.003	39	1.0380	-4.685	1.1	-0.004	0.017
NJ-Ostrich-1	Ostrich	3	33.883	0.2	-0.142	0.006	39	1.0380	-3.368	1.0	-0.015	0.015
USA2013-Njemu-001	Emu	1	31.160	-	-0.122	-	39	1.0380	-6.091	1.4	0.004	0.022

Table A2.3 (continued)

Sample ID	Species	N	Measured values				Body T[d]	$^{18}\alpha$[e]	Calculated values			
			$\delta^{18}O_c$[b]	±[c]	$\Delta'^{17}O_c$[b]	±[c]	°C	($CaCO_3$–H_2O)	$\delta^{18}O_w$[b]	±[f]	$\Delta'^{17}O_w$[b,g]	±[f]
Wild mammal tooth enamel from Passey et al. (2014)												
K00-AB-303p4	Black rhino	2	38.742	0.6	-0.164	0.005	38	1.0332	6.385	1.2	-0.052	0.016
K00-TSV-226	Hippopotamus	2	36.203	0.1	-0.137	0.006	38	1.0332	3.846	1.2	-0.025	0.016
Late Cretaceous dinosaur eggshell from Passey et al. (2014)												
Ukhaa Tolgod A7 1.1	Oviraptorid	3	25.606	0.4	-0.157	0.003	39	1.0380	-11.646	1.0	-0.031	0.015
A5-1.1 Ukhaa Tolgod Eggshell	Oviraptorid	3	33.049	1.0	-0.258	0.001	39	1.0380	-4.202	1.1	-0.132	0.015
Ukhaa Tolgod JH1	Oviraptorid	3	34.27	0.5	-0.258	0.006	39	1.0380	-2.981	1.0	-0.132	0.015
Ukhaa Tolgod 1GM100/975 egg	Oviraptorid	2	28.416	1.0	-0.211	0.019	39	1.0380	-8.835	1.1	-0.085	0.017
Late Cretaceous dinosaur eggshell-associated carbonates from Passey et al. (2014)												
A5-1.2 UT	Soil/diagenetic carbonates	2	26.768	1.9	-0.149	0.021	25	1.0368	-10.777	1.2	-0.020	0.017
A5-1.3 UT	Soil/diagenetic carbonates	2	26.676	2.3	-0.121	0.006	25	1.0368	-10.865	1.2	0.008	0.017
Ukhaa Tolgod JH2	Soil/diagenetic carbonates	1	29.749	–	-0.140	–	25	1.0368	-7.905	1.5	-0.011	0.022
Ukhaa Tolgod Calcite JH3	Soil/diagenetic carbonates	2	28.096	0.0	-0.150	0.005	25	1.0368	-9.498	1.2	-0.021	0.017
Ukhaa Tolgod Calcite JH4	Soil/diagenetic carbonates	1	27.289	–	-0.133	–	25	1.0368	-10.275	1.5	-0.004	0.022
Mammal tooth enamel data from Pack et al. (2013)												
Capreolus capreolus (male)	Artiodactyla	5	15.600	0.2	-0.113	0.02	38	1.0332	-1.700	0.4	-0.027	0.026
Cervus elaphus (male)	Artiodactyla	4	14.700	0.5	-0.150	0.02	38	1.0332	-2.600	0.7	-0.065	0.029
Dama dama (male)	Artiodactyla	6	16.800	0.3	-0.076	0.01	38	1.0332	-0.500	0.5	0.009	0.024
Sus scofa (male)	Artiodactyla	4	16.000	0.3	-0.054	0.02	38	1.0332	-1.300	0.5	0.031	0.029
Phococena phocoena	Cetacea	4	17.100	0.3	-0.087	0.01	38	1.0332	-0.200	0.5	-0.002	0.029
Crocidura leucodon	Eulipotyphla	5	18.000	0.3	-0.160	0.01	38	1.0332	0.700	0.5	-0.074	0.026
Suncus etruscus	Eulipotyphla	3	17.200	0.9	-0.217	0.02	38	1.0332	-0.100	1.1	-0.132	0.034
Oryctolagus cuniculus	Lagomorpha	4	19.800	0.2	-0.085	0.01	38	1.0332	2.500	0.4	0.001	0.029
Homo sapiens (male)	Primates	4	15.700	0.2	-0.113	0.02	38	1.0332	-1.600	0.4	-0.028	0.029
Elephas maximus (male, subadult)	Proboscidea	5	17.900	0.1	-0.109	0.01	38	1.0332	0.600	0.3	-0.024	0.026
Loxodonta africana	Proboscidea	13	19.700	0.1	-0.075	0.01	38	1.0332	2.400	0.3	0.011	0.016

Table A2.3 (continued)

Sample ID	Species	N	Measured values				Body T[d]	$^{18}\alpha$[e]	Calculated values			
			$\delta^{18}O_c$[b]	±[c]	$\Delta'^{17}O_c$[b]	±[c]	°C	($CaCO_3$–H_2O)	$\delta^{18}O_w$[b]	±[f]	$\Delta'^{17}O_w$[b,g]	±[f]
Apodemus flavicollis	Rodentia	3	17.300	0.4	-0.208	0.03	38	1.0332	0.000	0.6	-0.122	0.034
Apodemus sylvaticus (1)	Rodentia	4	18.000	0.4	-0.250	0.01	38	1.0332	0.700	0.6	-0.164	0.029
Apodemus sylvaticus (2)	Rodentia	2	17.100	0.4	-0.187	0.04	38	1.0332	-0.200	0.6	-0.102	0.042
Cricetus cricetus	Rodentia	4	17.100	0.2	-0.147	0.02	38	1.0332	-0.200	0.4	-0.062	0.029
Dipodomys sp.	Rodentia	3	20.300	0.4	-0.216	0.03	38	1.0332	3.000	0.6	-0.131	0.034
Mus musculus domesticus	Rodentia	3	15.500	0.5	-0.213	0.02	38	1.0332	-1.800	0.7	-0.127	0.034
Rattus norvegicus (juvenile)	Rodentia	4	19.400	0.2	-0.224	0.02	38	1.0332	2.100	0.4	-0.138	0.029
Sciurus vulgaris (1)	Rodentia	5	12.000	0.2	-0.223	0.02	38	1.0332	-5.300	0.4	-0.137	0.026
Sciurus vulgaris (2)	Rodentia	1	17.600	0.5	-0.199	0.05	38	1.0332	0.300	0.7	-0.113	0.059

a. Number of analyses, where each analysis involves acid digestion of carbonate to produce CO_2, reduction of CO_2 by H_2 to produce H_2O, fluorination of H_2O to produce O_2, and analysis of the gas on a Thermo MAT 253 mass spectrometer, as described in Section 2.2.

b. $\delta^{18}O_c$ and $\Delta^{17}O_c$ are isotopic compositions of O_2 generated from carbonates samples; $\delta^{18}O_w$ and $\Delta^{17}O_w$ are calculated parent water oxygen isotope compositions.

c. Values are the absolute difference between pairs of analyses.

d. Temperatures are based on the following: Birds and mammals: generic body temperature estimates.

e. Fractionation factor for eggshell carbonates is 1.0380, a combined mineral-water and acid digestion fractionation as determined by (Passey et al., 2014). For diagenetic carbonates, follow calculations in Kim and O'niel (1977) and multiply by a fractionation factor of 1.0081 (Kim et al., 2007).

f. Values are based on standard error propagation using the 95% confidence intervals error reported in Passey et al. (2014) for $^{18}\alpha_{CaCO_3-H_2O} = 1.0380 \pm 0.0008$ and $\lambda_{CaCO_3-H_2O} = 0.5245 \pm 0.0003$. Average external precision for $\delta^{18}O_c$ and $\Delta'^{17}O_c$ measurements are 0.7‰ (1σ) and 0.01‰ (1σ) (Passey et al., 2014). Then, errors used in the propagations are 1.96 × S.E.M, where S.E.M. are generic errors. S.E.M. = average external precision$/\sqrt{N}$ (N is number of analyses).

g. Calculated using $\Delta'^{17}O_w = \Delta'^{17}O_c + 10^3 \ln^{18}\alpha_{CaCO3-H2O} \times (0.528 - \lambda_{CaCO3-H2O})$, where $\lambda_{CaCO3-H2O}$ is 0.5245 for all samples.

A2.4. Matlab scripts for body water model

A2.3.1. Function: alpha1 *(see supplemental files)*

A2.3.2. Function: alpha2 *(see supplemental files)*

A2.3.3 Script for standard emu body water model *(see supplemental files)*

A3.1 $\delta^{13}C$, $\delta^{18}O$, and clumped isotope data

Table A3.1 Measured $\delta^{13}C$, $\delta^{18}O$, clumped isotope data and calculated clumped temperatures using Defliese et al. (2015) calibrations.

Time	Sample ID	N[a]	$\delta^{13}C_{cc}$ [b] /VPDB	$\delta^{18}O_{cc}$ [b] /VPDB	Δ_{47} [c]	±[d]	T [e] / °C
Late Cretaceous							
Mastrichtian	*Shanyang Formation*						
	S140519-1	1	-7.70	-10.89	0.670	0.029	34 ± 12
	S140515-19		-8.50	-3.87			
	S140515-16	1	-9.07	-4.96	0.656	0.029	40 ± 12
	S140517-4		-9.37	-1.09			
	S140514-7		-8.03	-6.00			
Maastrichtian /Campanian	*Nemegt Formation*						
	Bugin Tsav 1.1		-4.83	-9.26			
	BB06 Bugin Tsav	2	-6.77	-7.69	0.679	0.021	31 ± 8
	BB08 Bugin Tsav		-5.29	-8.85			
	Bugin Tsav eggshell BT1	1	-4.96	-10.11	0.702	0.029	23 ± 10
	Bugin Tsav eggshell BT2	1	-5.43	-9.76	0.692	0.029	26 ± 11
	Bugin Tsav eggshell BT3		-4.38	-8.90			
	Bugin Tsav 1GM100/1189	1	-6.14	-10.67	0.679	0.029	31 ± 11
	Bugin Tsav BT4		-5.20	-9.15			
Campanian	*Djadokhta Formation*						
	Ukhaa Tolgod JH1	1	-5.27	-2.81	0.662	0.029	37 ± 12
	Ukhaa Tolgod 1GM100/975	1	-4.28	-9.31	0.702	0.029	22 ± 10
	A5-1.1 Ukhaa Tolgod		-7.10	-4.99			
	Ukhaa Tolgod A7 1.1	3	-5.42	-12.09	0.692	0.017	26 ± 6
	Djadokhta Formation dinosaur-associated carbonates						
	A5-1.2 UT		–	–			
	A5-1.3 UT		-5.59	-12.22			
	Ukhaa Tolgod JH2	1	-2.42	-10.19	0.690	0.029	27 ± 11
	Ukhaa Tolgod Calcite JH3	1	-3.00	-11.41	0.679	0.029	31 ± 11
	Ukhaa Tolgod Calcite JH4	1	-4.91	-12.00	0.702	0.029	23 ± 10

Table A3.1 (continuted)

Time	Sample ID	N[a]	$d^{13}C_{cc}$ [b] /VPDB	$d^{18}O_{cc}$ [b] /VPDB	D_{47} [c]	±[d]	T [e] / °C
Campanian	*Djadokhta Formation*						
(continued)	A26-Bayn-Dzak	1	-4.47	-9.98	0.691	0.029	26 ± 11
	Bayn Dzak 1GM100/1150	3	-4.41	-11.19	0.694	0.017	25 ± 6
	Bayn Dzak 16M 100/1154	4	-7.21	-8.05	0.691	0.015	26 ± 5
	Bayn Dzak 1GM100/1154-2		–	–			
	Two Medicine Formation						
	UCM-377-1	2	-11.30	-15.07	0.580	0.021	77 ± 12
	UCM-377-2		-10.46	-15.50			
	UCM-377-3		-11.19	-14.82			
	UCM-948-1		-11.52	-12.06			
	UCM-948-2		-11.53	-11.37			
	UCM-948-3		-10.57	-10.88			
	UCM-949-1		-13.35	-16.23			
	UCM-949-2	2	-13.82	-11.85	0.609	0.021	61 ± 11
	UCM-949-3		-13.52	-13.77			
	UCM-378-1		-9.27	-12.50			
	UCM-378-2	2	-10.73	-10.12	0.622	0.021	55 ± 10
	UCM-378-3		-9.62	-10.89			
	UCM-952-1	1	-9.16	-12.10	0.580	0.029	77 ± 17
	UCM-952-2		-9.39	-11.06			
	UCM-952-3		-10.48	-9.71			
	Jingangkou Formation						
	S090723-D2#	1	-7.48	-3.61	0.653	0.029	41 ± 12
	Jingangkou Formation						
	L110813-D2#		-8.95	-6.97			
	L120625-D3	1	-8.75	-2.47	0.611	0.029	60 ± 15
	L120722-D3	1	-7.45	-7.86	0.603	0.029	64 ± 15
	L101209-D2		-6.28	-8.63			
	L100525-D2-1		-9.24	-6.23			
	L110712-D2	1	-9.04	-10.20	0.655	0.029	40 ± 12
	L100510-D6#		-7.94	-7.60			
	L100601-D5		-8.16	-6.88			
	L100525-D2-2	1	-9.24	-4.84	0.604	0.029	64 ± 15
	L100509-D2C		-8.00	-3.73			
	L110816-D1	1	-10.06	-6.10	0.596	0.029	68 ± 16
Santonian	*Jiangjunding Formation*						
	L120630-D1#	1	-8.19	-6.58	0.603	0.029	65 ± 15
	L130605-D1	1	-7.51	-8.42	0.616	0.029	58 ± 14

Table A3.1 (continuted)

Time	Sample ID	N[a]	$d^{13}C_{cc}$ [b] /VPDB	$d^{18}O_{cc}$ [b] /VPDB	D_{47} [c]	±[d]	T [e] / °C
Early Cretaceous							
Albian	*Cedar Mountain Formation*						
	UCM-264-6-1	2	-11.73	-4.55	0.578	0.021	78 ± 12
	UCM-264-6-2		-12.55	-5.99			
	UCM-264-6-3		-11.51	-4.50			
	UCM-861-1	2	-12.82	-9.25	0.599	0.021	67 ± 11
	UCM-861-2		-11.27	-4.14			
	UCM-861-3		-12.81	-6.35			
	UCM-157-1	1	-11.47	-7.20	0.597	0.029	68 ± 16
	UCM-157-2		-12.00	-6.78			
	UCM-157-3		-9.90	-6.18			
	Xinminpu Group						
	G140616-A	1	-6.97	-10.18	0.685	0.029	29 ± 11
Late Jurassic							
Oxfordian	*Morrison Formation*						
	UCM-418-1	2	-8.91	-5.00	0.531	0.021	110 ± 16
	UCM-418-2		-11.09	-6.60			
	UCM-418-3	1	-9.12	-5.12	0.591	0.029	71 ± 16
	UCM-418-4	2	-8.98	-5.10	0.531	0.021	110 ± 16
	UCM-532-1-1	2	-9.50	-5.09	0.597	0.021	67 ± 11
	UCM-532-1-2	1	-8.40	-8.79	0.615	0.029	59 ± 15
	UCM-532-1-3	1	-8.53	-7.71	0.506	0.029	130 ± 26
	UCM-532-1-4		-8.82	-4.80			
	UCM-656-1	2	-9.18	-3.68	0.596	0.021	68 ± 11
	UCM-656-2		-7.25	-5.93			
	UCM-656-3	1	-8.84	-4.16	0.488	0.029	146 ± 30

a. Number of clumped isotope analysis.
b. $\delta^{13}C_{cc}$ and $\delta^{18}O_{cc}$ are stable isotope values of carbonates reported in VPDB scale. These analyses were directly made on the CO_2 generated from carbonates samples. We report high precision $\delta^{13}C_{cc}$ and $\delta^{18}O_{cc}$ values for samples that have been analyzed for clumped isotopes. Other $\delta^{13}C_{cc}$ and $\delta^{18}O_{cc}$ values are from traditional stable isotope analysis using an automated extraction system. Notice that, $\delta^{18}O_{cc}$/VPDB and $\delta^{18}O_c$/VSMOW can be related through: $\delta^{18}O_c$/VSMOW = 1.0082 × [(1.03086 × $\delta^{18}O_{cc}$ /VPDB + 30.86) + 1000] - 1000.
c. Values relative to the 'carbon dioxide equilibrium scale' or CDES. An acid correction factor of 0.082‰ was applied to normalize these data to the 25 °C phosphoric acid reaction scale.
d. Average external precision for Δ_{47} measurements is 0.015‰ (σ). Then, errors used in the propagations are 1.96 × S.E.M, where S.E.M. are generic errors = average external precision/$\sqrt{N}$ (N is number of clumped analysis).
e. Paleotemperatures calculated using linear regressions through the theoretical Δ_{47}-temperature calibration from DeFliese et al. (2015): $\Delta_{47} = 37120/T^2 + 0.2784$.

A3.2 EBSD and EDS images of selective samples

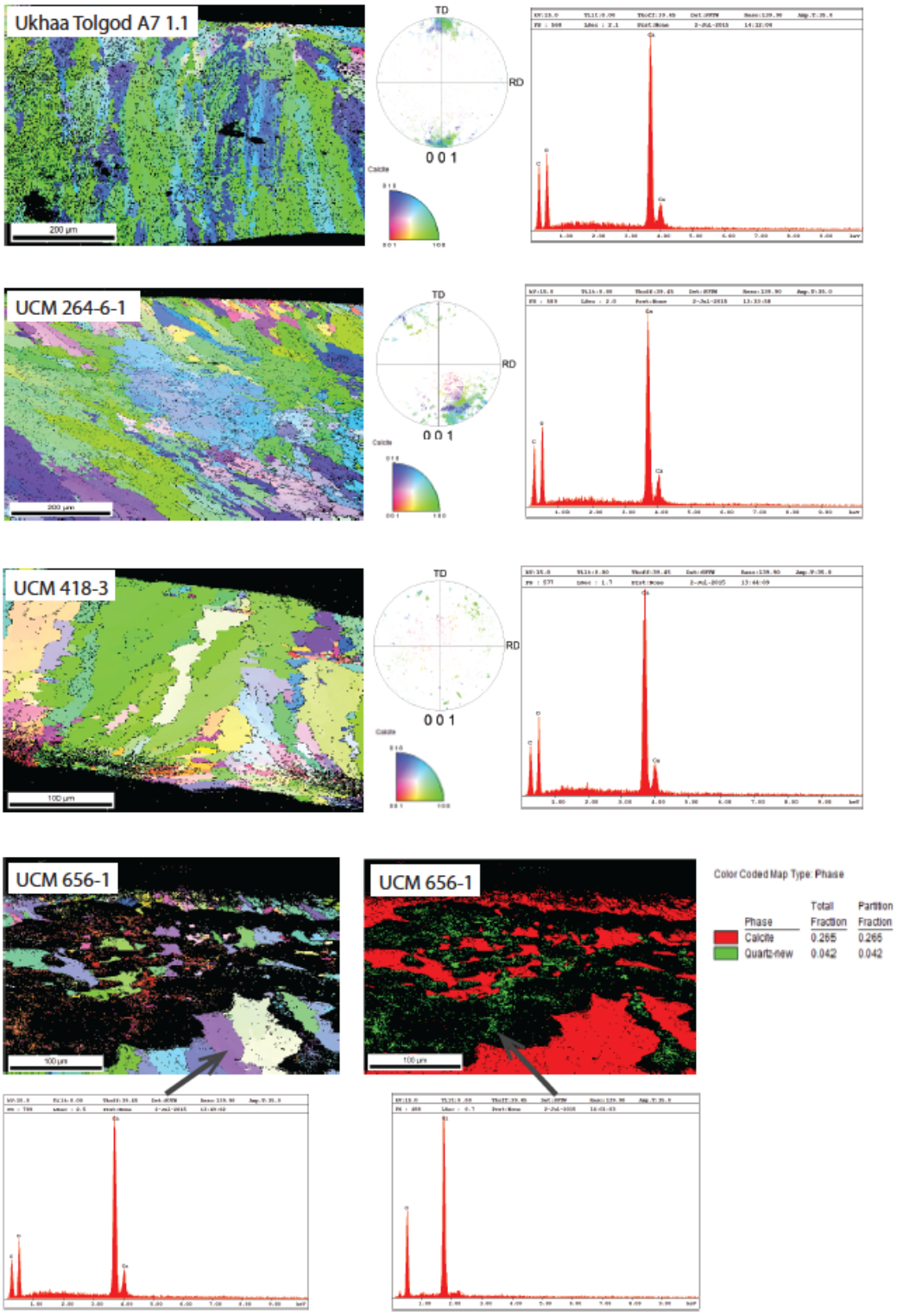

Figure A3.2. EBSD results (colored images) and EDS results (red curves) of selective dinosaur samples. Silification is observed in sample UCM 656-1.

A3.3 Influences of diagenesis on $\Delta'^{17}O$ and Δ_{47} temperatures

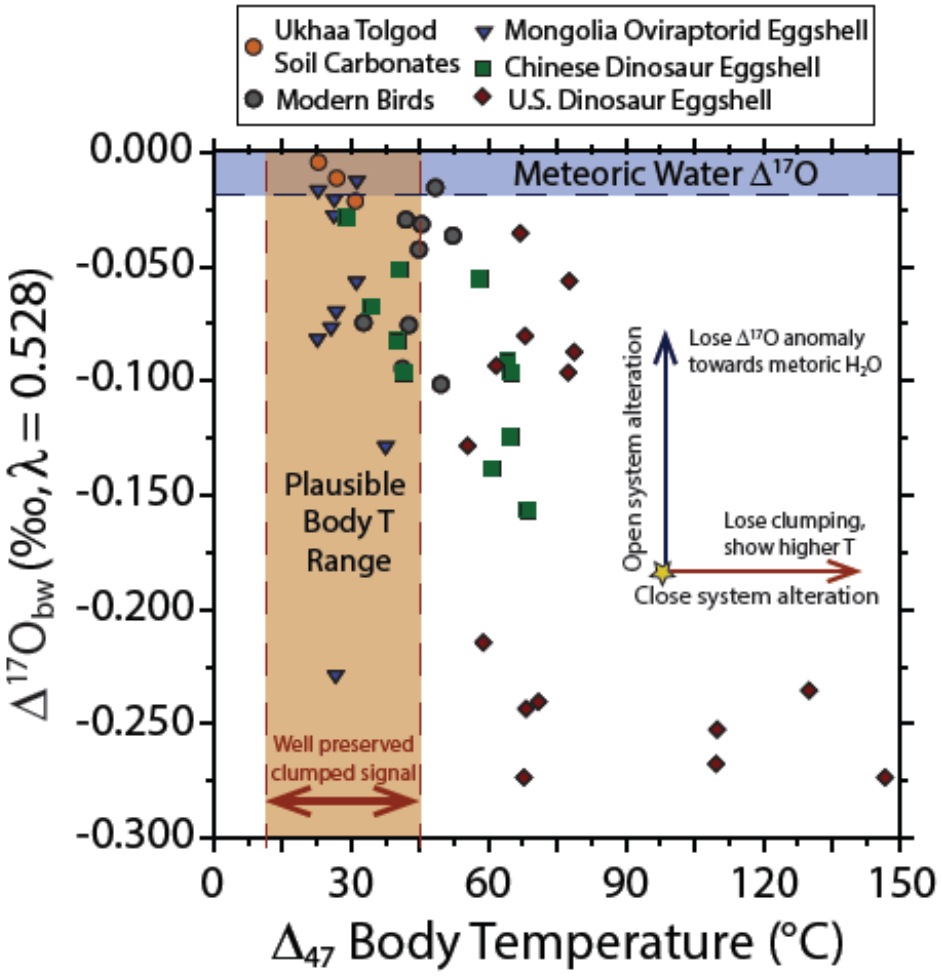

Figure A3.3 $\Delta'^{17}O - \Delta_{47}$ map for identifying possible alteration in samples. Blue shadowed range shows the lower $\Delta'^{17}O$ range of meteoric waters. Sample of lower $\Delta'^{17}O$ value than this range indicates at least partial preservation of its original $\Delta'^{17}O$ value. Orange shadowed range is the plausible body temperature of animals. Sample of higher Δ_{47} temperature than this range is possibly altered in clumped isotopes.

REFERENCES

Ahn, J., Brook, E.J., Mitchell, L., Rosen, J., McConnell, J.R., Taylor, K., Etheridge, D. and Rubino, M. (2012) Atmospheric CO_2 over the last 1000 years: A high-resolution record from the West Antarctic Ice Sheet (WAIS) Divide ice core. *Global Biogeochem. Cycles* **26**.

Angert, A., Cappa, C.D. and DePaolo, D.J. (2004) Kinetic ^{17}O effects in the hydrologic cycle: Indirect evidence and implications. *Geochim. Cosmochim. Acta* **68**, 3487-3495.

Arrhenius, S. (1896) XXXI. On the influence of carbonic acid in the air upon the temperature of the ground. *The London, Edinburgh, and Dublin Philosophical Magazine and Journal of Science* **41**, 237-276.

Assonov, S. and Brenninkmeijer, C. (2001) A new method to determine the ^{17}O isotopic abundance in CO_2 using oxygen isotope exchange with a solid oxide. *Rapid Commun. Mass Spectrom.* **15**, 2426-2437.

Ayliffe, L., Lister, A. and Chivas, A. (1992) The preservation of glacial-interglacial climatic signatures in the oxygen isotopes of elephant skeletal phosphate. *Palaeogeogr. Palaeoclim. Palaeoecol.* **99**, 179-191.

Ayliffe, L.K. and Chivas, A.R. (1990) Oxygen isotope composition of the bone phosphate of Australian kangaroos: potential as a palaeoenvironmental recorder. *Geochim. Cosmochim. Acta* **54**, 2603-2609.

Bakker, R.T. (1971) Dinosaur physiology and the origin of mammals. *Evolution*, 636-658.

Bao, H., Lyons, J. and Zhou, C. (2008) Triple oxygen isotope evidence for elevated CO_2 levels after a Neoproterozoic glaciation. *Nature* **453**, 504-506.

Barkan, E. and Luz, B. (2005) High precision measurements of $^{17}O/^{16}O$ and $^{18}O/^{16}O$ ratios in H_2O. *Rapid Commun. Mass Spectrom.* **19**, 3737-3742.

Barkan, E. and Luz, B. (2007) Diffusivity fractionations of $H_2{}^{16}O/H_2{}^{17}O$ and $H_2{}^{16}O/H_2{}^{18}O$ in air and their implications for isotope hydrology. *Rapid Commun. Mass Spectrom.* **21**, 2999-3005.

Barkan, E. and Luz, B. (2011) The relationships among the three stable isotopes of oxygen in air, seawater and marine photosynthesis. *Rapid Commun. Mass Spectrom.* **25**, 2367-2369.

Barkan, E. and Luz, B. (2012) High-precision measurements of $^{17}O/^{16}O$ and $^{18}O/^{16}O$ ratios in CO_2. *Rapid Commun. Mass Spectrom.* **26**, 2733-2738.

Barkan, E., Musan, I. and Luz, B. (2015) High-precision measurements of $\delta^{17}O$ and $^{17}O_{excess}$ of NBS19 and NBS18. *Rapid Commun. Mass Spectrom.* **29**, 2219-2224.

Barnola, J., Raynaud, D., Korotkevich, Y. and Lorius, C. (1987) *Vostok ice core provides 160,000-year record of atmospheric CO_2.*

Barras, V. and Simmonds, I. (2009) Observation and modeling of stable water isotopes as diagnostics of rainfall dynamics over southeastern Australia. *J. Geophys. Res. [Atmos.]* **114**.

Barrick, R.E., Showers, W.J. and Fischer, A.G. (1996) Comparison of thermoregulation of four ornithischian dinosaurs and a varanid lizard from the Cretaceous Two Medicine Formation: evidence from oxygen isotopes. *Palaios*, 295-305.

Beerling, D. (1999) Quantitative estimates of changes in marine and terrestrial primary productivity over the past 300 million years. *Proceedings of the Royal Society of London B: Biological Sciences* **266**, 1821-1827.

Beerling, D.J. and Royer, D.L. (2011) Convergent cenozoic CO_2 history. *Nat. Geosci.* **4**, 418-420.

Bender, M., Sowers, T. and Labeyrie, L. (1994) The Dole effect and its variations during the last 130,000 years as measured in the Vostok ice core. *Global Biogeochem. Cycles* **8**, 363-376.

Berner, R.A. (1999) Atmospheric oxygen over Phanerozoic time. *Proceedings of the National Academy of Sciences* **96**, 10955-10957.

Berner, R.A. (2006) GEOCARBSULF: a combined model for Phanerozoic atmospheric O_2 and CO_2. *Geochim. Cosmochim. Acta* **70**, 5653-5664.

Blunier, T., Barnett, B., Bender, M.L. and Hendricks, M.B. (2002) Biological oxygen productivity during the last 60,000 years from triple oxygen isotope measurements. *Global Biogeochem. Cycles* **16**.

Blunier, T., Bender, M., Barnett, B. and von Fischer, J. (2012) Planetary fertility during the past 400 ka based on the triple isotope composition of O_2 in trapped gases from the Vostok ice core. *Climate of the Past* **8**, 1509-1526.

Bowen, G.J. and Revenaugh, J. (2003) Interpolating the isotopic composition of modern meteoric precipitation. *Water Resour. Res.* **39**, 9-1-9-13.

Brenninkmeijer, C.A. and Röckmann, T. (1998) A rapid method for the preparation of O_2 from CO_2 for mass spectrometric measurement of $^{17}O/^{16}O$ ratios. *Rapid Commun. Mass Spectrom.* **12**, 479-483.

Bryant, J.D. and Froelich, P.N. (1995) A model of oxygen isotope fractionation in body water of large mammals. *Geochim. Cosmochim. Acta* **59**, 4523-4537.

Cao, X. and Liu, Y. (2011) Equilibrium mass-dependent fractionation relationships for triple oxygen isotopes. *Geochim. Cosmochim. Acta* **75**, 7435-7445.

Cao, X. and Bao, H. (2013) Dynamic model constraints on oxygen-17 depletion in atmospheric O_2 after a snowball Earth. *Proc. Nat. Acad. Sci. U.S.A.* **110**, 14546-14550.

Cerling, T.E. (1991) Carbon dioxide in the atmosphere. *Am. J. Sci.* **291**, 377-400.

Chaboureau, A.-C., Sepulchre, P., Donnadieu, Y. and Franc, A. (2014) Tectonic-driven climate change and the diversification of angiosperms. *Proceedings of the National Academy of Sciences* **111**, 14066-14070.

Chenery, C., Mueldner, G., Evans, J., Eckardt, H. and Lewis, M. (2010) Strontium and stable isotope evidence for diet and mobility in Roman Gloucester, UK. *J. Archaeol. Sci.* **37**, 150-163.

Chin, K. (2007) The paleobiological implications of herbivorous dinosaur coprolites from the Upper Cretaceous Two Medicine Formation of Montana: why eat wood? *Palaios* **22**, 554-566.

Clayton, R.N. and Mayeda, T.K. (1996) Oxygen isotope studies of achondrites. *Geochim. Cosmochim. Acta* **60**, 1999-2017.

Clementz, M.T., Holroyd, P.A. and Koch, P.L. (2008) Identifying aquatic habits of herbivorous mammals through stable isotope analysis. *Palaios* **23**, 574-585.

Coddington, C.L. and Cockburn, A. (1995) The mating system of free-living emus. *Aust J Zool* **43**, 365-372.

Coplen, T.B., Kendall, C. and Hopple, J. (1983) Comparison of stable isotope reference samples.

Costelloe, J.F., Grayson, R.B. and McMohan, T.A. (2003), Loss characteristics of arid zone river waterholes. *Proceedings of the 28th International Hydrology and Water Resources Symposium, Wollongong*. November 2003.

Craig, H. (1957) Isotopic standards for carbon and oxygen and correction factors for mass-spectrometric analysis of carbon dioxide. *Geochim. Cosmochim. Acta* **12**, 133-149.

Cramer, W., Bondeau, A., Woodward, F.I., Prentice, I.C., Betts, R.A., Brovkin, V., Cox, P.M., Fisher, V., Foley, J.A. and Friend, A.D. (2001) Global response of terrestrial ecosystem structure and function to CO_2 and climate change: results from six dynamic global vegetation models. *Global change biology* **7**, 357-373.

Criss, R.E. (1999) *Principles of stable isotope distribution*. Oxford University Press.

Croke, J., Magee, J. and Price, D. (1996) Major episodes of Quaternary activity in the lower Neales River, northwest of Lake Eyre, central Australia. *Palaeogeogr. Palaeoclim. Palaeoecol.* **124**, 1-15.

Curtis, P.S. and Wang, X. (1998) A meta-analysis of elevated CO_2 effects on woody plant mass, form, and physiology. *Oecologia* **113**, 299-313.

Cusack, M., Dauphin, Y., Chung, P., Pérez-Huerta, A. and Cuif, J.-P. (2008) Multiscale structure of calcite fibres of the shell of the brachiopod Terebratulina retusa. *Journal of structural biology* **164**, 96-100.

Daux, V., Lécuyer, C., Héran, M.-A., Amiot, R., Simon, L., Fourel, F., Martineau, F., Lynnerup, N., Reychler, H. and Escarguel, G. (2008) Oxygen isotope

fractionation between human phosphate and water revisited. *J. Hum. Evol.* **55**, 1138-1147.

Dawson, T., Herd, R. and Skadhauge, E. (1983) Water turnover and body water distribution during dehydration in a large arid-zone bird, the emu, *Dromaius novaehollandiae*. *J Comp. Physiol.* **153**, 235-240.

Defliese, W.F., Hren, M.T. and Lohmann, K.C. (2015) Compositional and temperature effects of phosphoric acid fractionation on Δ_{47} analysis and implications for discrepant calibrations. *Chem. Geol.* **396**, 51-60.

Dettman, D.L., Kohn, M.J., Quade, J., Ryerson, F., Ojha, T.P. and Hamidullah, S. (2001) Seasonal stable isotope evidence for a strong Asian monsoon throughout the past 10.7 my. *Geology* **29**, 31-34.

Dole, M. (1935) The relative atomic weight of oxygen in water and in air. *Journal of the American Chemical Society* **57**, 2731-2731.

Eagle, R.A., Tütken, T., Martin, T.S., Tripati, A.K., Fricke, H.C., Connely, M., Cifelli, R.L. and Eiler, J.M. (2011) Dinosaur body temperatures determined from isotopic (^{13}C-^{18}O) ordering in fossil biominerals. *Science* **333**, 443-445.

Eagle, R.A., Enriquez, M., Grellet-Tinner, G., Pérez-Huerta, A., Hu, D., Tütken, T., Montanari, S., Loyd, S.J., Ramirez, P. and Tripati, A.K. (2015) Isotopic ordering in eggshells reflects body temperatures and suggests differing thermophysiology in two Cretaceous dinosaurs. *Nature communications* **6**.

Ekart, D.D., Cerling, T.E., Montanez, I.P. and Tabor, N.J. (1999) A 400 million year carbon isotope record of pedogenic carbonate: implications for paleoatmospheric carbon dioxide. *Am. J. Sci.* **299**, 805-827.

Epstein, S. and Zeiri, L. (1988) Oxygen and carbon isotopic compositions of gases respired by humans. *Proc. Nat. Acad. Sci. U.S.A.* **85**, 1727-1731.

Essenhigh, R.H. (2009) Potential dependence of global warming on the residence time (RT) in the atmosphere of anthropogenically sourced carbon dioxide. *Energy Fuel.* **23**, 2773-2784.

Falkowski, P.G., Katz, M.E., Milligan, A.J., Fennel, K., Cramer, B.S., Aubry, M.P., Berner, R.A., Novacek, M.J. and Zapol, W.M. (2005) The rise of oxygen over the past 205 million years and the evolution of large placental mammals. *Science* **309**, 2202-2204.

Ferry, J.M., Passey, B.H., Vasconcelos, C. and Eiler, J.M. (2011) Formation of dolomite at 40–80° C in the Latemar carbonate buildup, Dolomites, Italy, from clumped isotope thermometry. *Geology* **39**, 571-574.

Francey, R.J. and Tans, P.P. (1987) Latitudinal variation in oxygen-18 of atmospheric CO_2.

Franks, P.J., Royer, D.L., Beerling, D.J., Van de Water, P.K., Cantrill, D.J., Barbour, M.M. and Berry, J.A. (2014) New constraints on atmospheric CO_2 concentration for the Phanerozoic. *Geophys. Res. Lett.* **41**, 4685-4694.

Fricke, H.C. and O'Neil, J.R. (1996) Inter-and intra-tooth variation in the oxygen isotope composition of mammalian tooth enamel phosphate: implications for palaeoclimatological and palaeobiological research. *Palaeogeography, Palaeoclimatology, Palaeoecology* **126**, 91-99.

Fricke, H.C., Clyde, W.C., O'Neil, J.R. and Gingerich, P.D. (1998a) Evidence for rapid climate change in North America during the latest Paleocene thermal maximum:

oxygen isotope compositions of biogenic phosphate from the Bighorn Basin (Wyoming). *Earth Planet. Sci. Lett.* **160**, 193-208.

Fricke, H.C., Clyde, W.C. and O'Neil, J.R. (1998b) Intra-tooth variations in $\delta^{18}O$ (PO_4) of mammalian tooth enamel as a record of seasonal variations in continental climate variables. *Geochim. Cosmochim. Acta* **62**, 1839-1850.

Fricke, H.C. and Wing, S.L. (2004) Oxygen isotope and paleobotanical estimates of temperature and $\delta^{18}O$–latitude gradients over North America during the early Eocene. *Am. J. Sci.* **304**, 612-635.

Friedman, I. and O'Neil, J.R. (1977) *Compilation of stable isotope fractionation factors of geochemical interest*. US Government Printing Office. **440**.

Gat, J.R. (1996) Oxygen and hydrogen isotopes in the hydrologic cycle. *Annual Review of Earth and Planetary Sciences* **24**, 225-262.

Gehler, A., Tütken, T. and Pack, A. (2012) Oxygen and carbon isotope variations in a modern rodent community–implications for palaeoenvironmental reconstructions. *PLoS One* **7**, e49531.

Gehler, A., Gingerich, P.D. and Pack, A. (2016) Temperature and atmospheric CO_2 concentration estimates through the PETM using triple oxygen isotope analysis of mammalian bioapatite. *Proceedings of the National Academy of Sciences* **113**, 7739-7744.

Hamilton, S.K., Bunn, S.E., Thoms, M.C. and Marshall, J.C. (2005) Persistence of aquatic refugia between flow pulses in a dryland river system (Cooper Creek, Australia). *Limnol. Oceanogr.* **50**, 743-754.

Haworth, M., Hesselbo, S.P., McElwain, J.C., Robinson, S.A. and Brunt, J.W. (2005) Mid-Cretaceous pCO_2 based on stomata of the extinct conifer Pseudofrenelopsis (Cheirolepidiaceae). *Geology* **33**, 749-752.

Helliker, B.R. and Ehleringer, J.R. (2000) Establishing a grassland signature in veins: ^{18}O in the leaf water of C_3 and C_4 grasses. *Proc. Nat. Acad. Sci. U.S.A.* **97**, 7894-7898.

Henehan, M.J., Rae, J.W., Foster, G.L., Erez, J., Prentice, K.C., Kucera, M., Bostock, H.C., Martínez-Botí, M.A., Milton, J.A. and Wilson, P.A. (2013) Calibration of the boron isotope proxy in the planktonic foraminifera Globigerinoides ruber for use in palaeo-CO_2 reconstruction. *Earth Planet. Sci. Lett.* **364**, 111-122.

Henkes, G.A., Passey, B.H., Grossman, E.L., Shenton, B.J., Pérez-Huerta, A. and Yancey, T.E. (2014) Temperature limits for preservation of primary calcite clumped isotope paleotemperatures. *Geochim. Cosmochim. Acta* **139**, 362-382.

Hofmann, M.E. and Pack, A. (2010) Technique for high-precision analysis of triple oxygen isotope ratios in carbon dioxide. *Analytical chemistry* **82**, 4357-4361.

Hofmann, M.E., Horváth, B. and Pack, A. (2012) Triple oxygen isotope equilibrium fractionation between carbon dioxide and water. *Earth Planet. Sci. Lett.* **319**, 159-164.

Holtz Jr, T.R., Brinkman, D.L. and Chandler, C.L. (1998) Denticle morphometrics and a possibly omnivorous feeding habit for the theropod dinosaur Troodon. *Gaia* **15**, 159-166.

Hulston, J. and Thode, H. (1965) Variations in the S33, S34, and S36 contents of meteorites and their relation to chemical and nuclear effects. *J. Geophys. Res.* **70**, 3475-3484.

Huntington, K.W., Budd, D.A., Wernicke, B.P. and Eiler, J.M. (2011) Use of clumped-isotope thermometry to constrain the crystallization temperature of diagenetic calcite. *J. Sediment. Res.* **81**, 656-669; doi: 610.2110/jsr.2011.2151.

Jerzykiewicz, T., Currie, P., Eberth, D., Johnston, P., Koster, E. and Zheng, J.-J. (1993) Djadokhta Formation correlative strata in Chinese Inner Mongolia: an overview of the stratigraphy, sedimentary geology, and paleontology and comparisons with the type locality in the pre-Altai Gobi. *Can. J. Earth Sci.* **30**, 2180-2195.

Johnson, B., Miller, G., Fogel, M., Magee, J., Gagan, M. and Chivas, A. (1999) 65,000 years of vegetation change in central Australia and the Australian summer monsoon. *Science* **284**, 1150-1152.

Kim, S.-T. and O'Neil, J.R. (1997) Equilibrium and nonequilibrium oxygen isotope effects in synthetic carbonates. *Geochim. Cosmochim. Acta* **61**, 3461-3475.

Kohn, M.J. (1996) Predicting animal $\delta^{18}O$: accounting for diet and physiological adaptation. *Geochim. Cosmochim. Acta* **60**, 4811-4829.

Kohn, M.J. and Cerling, T.E. (2002) Stable isotope compositions of biological apatite. *Rev. Mineral. Geochem.* **48**, 455-488.

Landais, A., Barkan, E., Yakir, D. and Luz, B. (2006) The triple isotopic composition of oxygen in leaf water. *Geochim. Cosmochim. Acta* **70**, 4105-4115.

Landais, A., Barkan, E. and Luz, B. (2008) Record of $\delta^{18}O$ and ^{17}O-excess in ice from Vostok Antarctica during the last 150,000 years. *Geophys. Res. Lett.* **35**, L02709.

Landais, A., Risi, C., Bony, S., Vimeux, F., Descroix, L., Falourd, S. and Bouygues, A. (2010) Combined measurements of ^{17}O-excess and d-excess in African monsoon

precipitation: Implications for evaluating convective parameterizations. *Earth Planet. Sci. Lett.* **298**, 104-112.

Landais, A., Ekaykin, A., Barkan, E., Winkler, R. and Luz, B. (2012a) Seasonal variations of ^{17}O-excess and d-excess in snow precipitation at Vostok station, East Antarctica. *J. Glaciol.* **58**, 725-733.

Landais, A., Steen-Larsen, H.C., Guillevic, M., Masson-Delmotte, V., Vinther, B. and Winkler, R. (2012b) Triple isotopic composition of oxygen in surface snow and water vapor at NEEM (Greenland). *Geochim. Cosmochim. Acta* **77**, 304-316.

Lécuyer, C., Grandjean, P. and Emig, C. (1996) Determination of oxygen isotope fractionation between water and phosphate from living lingulids: potential application to palaeoenvironmental studies. *Palaeogeogr. Palaeoclim. Palaeoecol.* **126**, 101-108.

Lécuyer, C., Balter, V., Martineau, F., Fourel, F., Bernard, A., Amiot, R., Gardien, V., Otero, O., Legendre, S. and Panczer, G. (2010) Oxygen isotope fractionation between apatite-bound carbonate and water determined from controlled experiments with synthetic apatites precipitated at 10–37 °C. *Geochim. Cosmochim. Acta* **74**, 2072-2081.

Levin, N.E., Cerling, T.E., Passey, B.H., Harris, J.M. and Ehleringer, J.R. (2006) A stable isotope aridity index for terrestrial environments. *Proc. Nat. Acad. Sci. U.S.A.* **103**, 11201-11205.

Levin, N.E., Raub, T.D., Dauphas, N. and Eiler, J.M. (2014) Triple oxygen isotope variations in sedimentary rocks. *Geochim. Cosmochim. Acta* **139**, 173-189.

Li, S., Levin, N.E. and Chesson, L.A. (2015) Continental Scale Variation in ^{17}O-excess of Meteoric Waters in the United States. *Geochim. Cosmochim. Acta* **164**, 110-126.

Liu, J., Fu, G., Song, X., Charles, S.P., Zhang, Y., Han, D. and Wang, S. (2010) Stable isotopic compositions in Australian precipitation. *J. Geophys. Res. [Atmos.]* **115**, D23.

Long, S. (1991) Modification of the response of photosynthetic productivity to rising temperature by atmospheric CO_2 concentrations: has its importance been underestimated? *Plant Cell Environ.* **14**, 729-739.

Longinelli, A. (1984) Oxygen isotopes in mammal bone phosphate: a new tool for paleohydrological and paleoclimatological research? *Geochim. Cosmochim. Acta* **48**, 385-390.

Lüthi, D., Le Floch, M., Bereiter, B., Blunier, T., Barnola, J.-M., Siegenthaler, U., Raynaud, D., Jouzel, J., Fischer, H. and Kawamura, K. (2008) High-resolution carbon dioxide concentration record 650,000–800,000 years before present. *Nature* **453**, 379-382.

Luz, B., Kolodny, Y. and Horowitz, M. (1984) Fractionation of oxygen isotopes between mammalian bone-phosphate and environmental drinking water. *Geochim. Cosmochim. Acta* **48**, 1689-1693.

Luz, B. and Kolodny, Y. (1985) Oxygen isotope variations in phosphate of biogenic apatites, IV. Mammal teeth and bones. *Earth Planet. Sci. Lett.* **75**, 29-36.

Luz, B., Cormie, A.B. and Schwarcz, H.P. (1990) Oxygen isotope variations in phosphate of deer bones. *Geochim. Cosmochim. Acta* **54**, 1723-1728.

Luz, B., Barkan, E., Bender, M.L., Thiemens, M.H. and Boering, K.A. (1999) Triple-isotope composition of atmospheric oxygen as a tracer of biosphere productivity. *Nature* **400**, 547-550.

Luz, B. and Barkan, E. (2005) The isotopic ratios $^{17}O/^{16}O$ and $^{18}O/^{16}O$ in molecular oxygen and their significance in biogeochemistry. *Geochim. Cosmochim. Acta* **69**, 1099-1110.

Luz, B. and Barkan, E. (2010) Variations of $^{17}O/^{16}O$ and $^{18}O/^{16}O$ in meteoric waters. *Geochim. Cosmochim. Acta* **74**, 6276-6286.

Mahata, S., Bhattacharya, S.K., Wang, C.H. and Liang, M.C. (2012) An improved CeO_2 method for high-precision measurements of $^{17}O/^{16}O$ ratios for atmospheric carbon dioxide. *Rapid Commun. Mass Spectrom.* **26**, 1909-1922.

Mahata, S., Bhattacharya, S. and Liang, M.C. (2016) An improved method of high-precision determination of $\Delta^{17}O$ of CO_2 by catalyzed exchange with O_2 using hot platinum. *Rapid Commun. Mass Spectrom.* **30**, 119-131.

Majoube, M. (1971) Oxygen-18 and deuterium fractionation between water and steam. *J Chim. Phys. PCB.* **68**, 1423.

Maloney, S. and Dawson, T. (1993) Sexual dimorphism in basal metabolism and body temperature of a large bird, the emu. *Condor* **95**, 1034-1037.

Matsuhisa, Y., Goldsmith, J.R. and Clayton, R.N. (1978) Mechanisms of hydrothermal crystallization of quartz at 250 °C and 15 kbar. *Geochim. Cosmochim. Acta* **42**, 173-182.

McMahon, T.A. and Merz, S.K. (2005) *Hydrology of Lake Eyre Basin*. Sinclair Knight Merz.

Meijer, H. and Li, W. (1998) The use of electrolysis for accurate $\delta^{17}O$ and $\delta^{18}O$ isotope measurements in water. *Isot. Environ. Health Stud.* **34**, 349-369.

Miller, M.F. (2002) Isotopic fractionation and the quantification of ^{17}O anomalies in the oxygen three-isotope system: an appraisal and geochemical significance. *Geochim. Cosmochim. Acta* **66**, 1881-1889.

Montanari, S., Higgins, P. and Norell, M.A. (2013) Dinosaur eggshell and tooth enamel geochemistry as an indicator of Mongolian Late Cretaceous paleoenvironments. *Palaeogeogr. Palaeoclim. Palaeoecol.* **370**, 158-166.

Montañez, I.P., Tabor, N.J., Niemeier, D., DiMichele, W.A., Frank, T.D., Fielding, C.R., Isbell, J.L., Birgenheier, L.P. and Rygel, M.C. (2007) CO_2-forced climate and vegetation instability during Late Paleozoic deglaciation. *Science* **315**, 87-91.

Mook, W. and Rozanski, K. (2000) Environmental isotopes in the hydrological cycle. *IAEA Publish* **39**.

Mook, W.G. (2000) *Environmental isotopes in the hydrological cycle: principles and applications*. Unesco.

Nagy, K.A. (2004), Water economy of free-living desert animals. *Int. Congr. Ser.* **1275**, pp. 291-297.

Nagy, K.A.P. (1988) Scaling of water flux rate in animals. *Univ. Calif. Publ. Zool.* **120**, 1-172.

New, M., Lister, D., Hulme, M. and Makin, I. (2002) A high-resolution data set of surface climate over global land areas. *Clim. Res.* **21**, 1-25.

O'Neil, J.R. and Adami, L.H. (1969) Oxygen isotope partition function ratio of water and the structure of liquid water. *J. Phys. Chem.* **73**, 1553-1558.

O'Neil, J.R., Clayton, R.N. and Mayeda, T.K. (1969) *Oxygen isotope fractionation in divalent metal carbonates*. Univ. of Chicago.

Pack, A., Gehler, A. and Süssenberger, A. (2013) Exploring the usability of isotopically anomalous oxygen in bones and teeth as paleo-CO_2-barometer. *Geochim. Cosmochim. Acta* **102**, 306-317.

Pack, A. and Herwartz, D. (2014) The triple oxygen isotope composition of the Earth mantle and understanding variations in terrestrial rocks and minerals. *Earth Planet. Sci. Lett.* **390**, 138-145.

Paladino, F.V., O'Connor, M.P. and Spotila, J.R. (1990) Metabolism of leatherback turtles, gigantothermy, and thermoregulation of dinosaurs. *Nature* **344**, 858-860.

Passalia, M.G. (2009) Cretaceous pCO_2 estimation from stomatal frequency analysis of gymnosperm leaves of Patagonia, Argentina. *Palaeogeography, Palaeoclimatology, Palaeoecology* **273**, 17-24.

Passey, B.H., Cerling, T.E. and Levin, N.E. (2007) Temperature dependence of oxygen isotope acid fractionation for modern and fossil tooth enamels. *Rapid Commun. Mass Spectrom.* **21**, 2853-2859.

Passey, B.H., Levin, N.E., Cerling, T.E., Brown, F.H. and Eiler, J.M. (2010) High-temperature environments of human evolution in East Africa based on bond ordering in paleosol carbonates. *Proc. Nat. Acad. Sci. U.S.A.* **107**, 11245-11249.

Passey, B.H., Hu, H.T., Ji, H.Y., Montanari, S., Li, S.N., Henkes, G.A. and Levin, N.E. (2014) Triple oxygen isotopes in biogenic and sedimentary carbonates. *Geochim. Cosmochim. Acta* **141**, 1-25.

Patodkar, V., Rahane, S., Shejal, M. and Belhekar, D. (2009) Behavior of Emu bird (*Dromaius novaehollandiae*). *Vet. World* **2**, 439-440.

Pearson, P.N., Foster, G.L. and Wade, B.S. (2009) Atmospheric carbon dioxide through the Eocene–Oligocene climate transition. *Nature* **461**, 1110-1113.

Pérez-Huerta, A., Cusack, M. and England, J. (2007) Crystallography and diagenesis in fossil craniid brachiopods. *Palaeontology* **50**, 757-763.

Pérez-Huerta, A., Cusack, M. and Mendez, C.A. (2012) Preliminary assessment of the use of electron backscatter diffraction (EBSD) in conodonts. *Lethaia* **45**, 253-258.

Petit, J.-R., Jouzel, J., Raynaud, D., Barkov, N.I., Barnola, J.-M., Basile, I., Bender, M., Chappellaz, J., Davis, M. and Delaygue, G. (1999) Climate and atmospheric history of the past 420,000 years from the Vostok ice core, Antarctica. *Nature* **399**, 429-436.

Picard, S., Garcia, J.-P., Lécuyer, C., Sheppard, S.M., Cappetta, H. and Emig, C.C. (1998) $\delta^{18}O$ values of coexisting brachiopods and fish: Temperature differences and estimates of paleo–water depths. *Geology* **26**, 975-978.

Podlesak, D.W., Torregrossa, A.-M., Ehleringer, J.R., Dearing, M.D., Passey, B.H. and Cerling, T.E. (2008) Turnover of oxygen and hydrogen isotopes in the body water, CO_2, hair, and enamel of a small mammal. *Geochim. Cosmochim. Acta* **72**, 19-35.

Roden, J.S. and Ehleringer, J.R. (1999) Observations of hydrogen and oxygen isotopes in leaf water confirm the Craig-Gordon model under wide-ranging environmental conditions. *Plant Physiol.* **120**, 1165-1174.

Roden, J.S., Lin, G. and Ehleringer, J.R. (2000) A mechanistic model for interpretation of hydrogen and oxygen isotope ratios in tree-ring cellulose. *Geochim. Cosmochim. Acta* **64**, 21-35.

Royer, D. (2001) Stomatal density and stomatal index as indicators of paleoatmospheric CO_2 concentration. *Review of Palaeobotany and Palynology* **114**, 1-28.

Royer, D.L., Berner, R.A. and Beerling, D.J. (2001a) Phanerozoic atmospheric CO_2 change: evaluating geochemical and paleobiological approaches. *Earth-Science Reviews* **54**, 349-392.

Royer, D.L., Wing, S.L., Beerling, D.J., Jolley, D.W., Koch, P.L., Hickey, L.J. and Berner, R.A. (2001b) Paleobotanical evidence for near present-day levels of atmospheric CO2 during part of the Tertiary. *Science* **292**, 2310-2313.

Royer, D.L., Berner, R.A. and Park, J. (2007) Climate sensitivity constrained by CO_2 concentrations over the past 420 million years. *Nature* **446**, 530-532.

Rumble, D., Miller, M.F., Franchi, I. and Greenwood, R. (2007) Oxygen three-isotope fractionation lines in terrestrial silicate minerals: An inter-laboratory comparison of hydrothermal quartz and eclogitic garnet. *Geochim. Cosmochim. Acta* **71**, 3592-3600.

Schoeller, D.A., Leitch, C.A. and Brown, C. (1986) Doubly labeled water method: in vivo oxygen and hydrogen isotope fractionation. *American Journal of Physiology-Regulatory, Integrative and Comparative Physiology* **251**, R1137-R1143.

Schoenemann, S.W., Schauer, A.J. and Steig, E.J. (2013) Measurement of SLAP2 and GISP $\delta^{17}O$ and proposed VSMOW-SLAP normalization for $\delta^{17}O$ and $^{17}O_{excess}$. *Rapid Commun. Mass Spectrom.* **27**, 582-590.

Schoenemann, S.W., Steig, E.J., Ding, Q., Markle, B.R. and Schauer, A.J. (2014) Triple water-isotopologue record from WAIS Divide, Antarctica: Controls on glacial-interglacial changes in $^{17}O_{excess}$ of precipitation. *J. Geophys. Res. [Atmos.]* **119**, 8741-8763.

Shaheen, R., Janssen, C. and Röckmann, T. (2007) Investigations of the photochemical isotope equilibrium between O_2, CO_2 and O_3. *Atmos. Chem. Phys.* **7**, 495-509.

Steig, E., Gkinis, V., Schauer, A., Schoenemann, S., Samek, K., Hoffnagle, J., Dennis, K. and Tan, S. (2013) Calibrated high-precision $^{17}O_{excess}$ measurements using laser-current tuned cavity ring-down spectroscopy. *Atmos. Meas. Tech. Discuss* **6**, 10191-10229.

Sundquist, E.T. and Broecker, W.S. (1985) The carbon cycle and atmospheric CO_2: Natural variations Archean to present. *Washington DC American Geophysical Union Geophysical Monograph Series* **32**.

Surma, J., Assonov, S., Bolourchi, M. and Staubwasser, M. (2015) Triple oxygen isotope signatures in evaporated water bodies from the Sistan Oasis, Iran. *Geophys. Res. Lett.* **42**, 8456-8462.

Tapper, N. and Hurry, L. (1993). Australia's weather patterns: an introductory guide. *Dellasta Pty. Ltd.*, pp. 130.

Tappert, R., McKellar, R.C., Wolfe, A.P., Tappert, M.C., Ortega-Blanco, J. and Muehlenbachs, K. (2013) Stable carbon isotopes of C3 plant resins and ambers record changes in atmospheric oxygen since the Triassic. *Geochim. Cosmochim. Acta* **121**, 240-262.

Thiemens, M.H. and Heidenreich, J.E. (1983) The mass-independent fractionation of oxygen: A novel isotope effect and its possible cosmochemical implications. *Science* **219**, 1073-1075.

Thiemens, M.H., Jackson, T., Zipf, E.C., Erdman, P.W. and van Egmond, C. (1995) Carbon dioxide and oxygen isotope anomalies in the mesosphere and stratosphere. *Science* **270**, 969-972.

Uemura, R., Barkan, E., Abe, O. and Luz, B. (2010) Triple isotope composition of oxygen in atmospheric water vapor. *Geophys. Res. Lett.* **37**.

Urey, H.C. (1952) On the early chemical history of the earth and the origin of life. *Proceedings of the National Academy of Sciences* **38**, 351-363.

Weishampel, D.B., Dodson, P. and Osmólska, H. (1990) *The dinosauria*. Univ of California Press.

Wenzel, B., Lécuyer, C. and Joachimski, M.M. (2000) Comparing oxygen isotope records of Silurian calcite and phosphate—$\delta^{18}O$ compositions of brachiopods and conodonts. *Geochim. Cosmochim. Acta* **64**, 1859-1872.

Williams, J.B., Siegfried, W.R., Milton, S.J., Adams, N.J., Dean, W., du Plessis, M.A. and Jackson, S. (1993) Field metabolism, water requirements, and foraging behavior of wild ostriches in the Namib. *Ecology* **74**, 390-404.

Woodward, F.I. (1987) Stomatal numbers are sensitive to increases in CO_2 from pre-industrial levels. *Nature* **327**, 617-618.

Yakir, D., DeNiro, M. and Gat, J. (1990) Natural deuterium and oxygen-18 enrichment in leaf water of cotton plants grown under wet and dry conditions: evidence for water compartmentation and its dynamics. *Plant Cell Environ.* **13**, 49-56.

Yakir, D. (1992) *Water compartmentation in plant tissue: isotopic evidence*, Water and Life. Springer, pp. 205-222.

Yakir, D. (1998) Oxygen-18 of leaf water: a crossroad for plant-associated isotopic signals. *Stable isotopes: integration of biological, ecological and geochemical processes* (ed. H. Griffiths), BIOS Scientific Publishers Ltd. pp. 147-168

Young, E.D., Galy, A. and Nagahara, H. (2002) Kinetic and equilibrium mass-dependent isotope fractionation laws in nature and their geochemical and cosmochemical significance. *Geochim. Cosmochim. Acta* **66**, 1095-1104.

Young, E.D., Yeung, L.Y. and Kohl, I.E. (2014) On the $\Delta^{17}O$ budget of atmospheric O_2. *Geochim. Cosmochim. Acta* **135**, 102-125.

Yung, Y.L., DeMore, W. and Pinto, J.P. (1991) Isotopic exchange between carbon dioxide and ozone via O (^1D) in the stratosphere. *Geophys. Res. Lett.* **18**, 13-16.

Yung, Y.L., Lee, A.Y., Irion, F.W., DeMore, W.B. and Wen, J. (1997) Carbon dioxide in the atmosphere: Isotopic exchange with ozone and its use as a tracer in the middle atmosphere. *Journal of Geophysical Research: Atmospheres* **102**, 10857-10866.

Zachos, J., Pagani, M., Sloan, L., Thomas, E. and Billups, K. (2001) Trends, rhythms, and aberrations in global climate 65 Ma to present. *Science* **292**, 686-693.

CURRICULUM VITAE

Huanting Hu

Department of Earth and Planetary Sciences
The Johns Hopkins University, 301 Olin Hall, 3400 N.
Charles St. Baltimore, MD 21218
Phone: (410) 209-0399, Email: huhuanting1988@gmail.com
Website: http://huantinghu.weebly.com

Research Interest

Stable isotope geochemistry: *e.g.* clumped isotopes and triple oxygen isotopes.
Modeling: Earth system modeling, biogeochemistry, theoretical isotope modeling
Evaluation of paleoclimate and paleovegetation using a multiproxy approach.
Methods development in isotopic geochemistry to address questions about Earth.

Education

2011 - Present
Ph.D. candidate, The Department of Earth & Planetary Sciences **(EPS)**, **Johns Hopkins University (JHU)**, Expected graduation: September 2016
Proposed Dissertation: Triple oxygen isotopes in biogenic carbonates and applications to Mesozoic carbon cycle dynamics and animal physiology.
Advisor: Benjamin H. Passey

2007 - 2011
Bachelor of Science in Geochemistry, Department of Earth and Space Sciences,
University of Science and Technology of China (USTC)
Senior Thesis: Sr-Nd-Pb isotopic composition of the Cenozoic lamprophyre in the northwest Vietnam and the origin of rocks
Advisor: Fukun Chen

Laboratory Experience

2012 - Present
Research Assistant, Stable Isotope Lab, **JHU**
Triple oxygen isotope analysis of carbonates and waters,
Clumped isotope analysis, conventional $\delta^{13}C$ and $\delta^{18}O$ analysis of carbonates, Laser ablation GC/IRMS system, EDS, XRD analysis.
Constructed a custom CO_2-H_2O reduction line, operation and improvement of a ^{17}O H_2O fluorination line.

2010 - 2011
Research Assistant, **USTC**
Clean room sample preparation and TIMS operation for Sr-Nd-Pb isotopes, X-ray fluorescence analysis and ICP-MS trace element analysis.

Teaching Experience

Spring 2015	Attendance at an introductory teaching course "*Introduction to Teaching at the College Level*", JHU
2012-2013	Teaching Assistant, Dept. of EPS, JHU "*Introduction to Global Environmental Change*" Fall 2012, Fall 2013 "*Guided Tour: The Planets*" Spring 2013, Spring 2015

Awards and Fellowships

2014	Urbino Summer School in Paleoclimatology Best Poster Award
2014	Urbino Summer School in Paleoclimatology NSF Scholarship
2014	Palmer Field Fund, field and lab work in Italy, JHU
2011 - 2012	The Dean's Fellowship Dept. of Earth and Planetary Sciences, JHU
2011	Outstanding Undergraduate Research Project at USTC
2010	Outstanding Student Scholarship (Grade 1) at USTC
2009	Outstanding Student Scholarship (Grade 2) at USTC
2008	Outstanding Student Scholarship (Grade 3) at USTC

Field Experience

2011	Western Maryland, US, fieldwork for Sedimentary Geology course
2010	Dabie Mountain, Anhui, China, field course of Physical Geology
2009	Zhoukoudian, Beijing, China, field course of Structural Geology
2008	Chao Lake, Anhui, China, field course of Sedimentary Geology

Computer Skills

Proficient in:	
	Matlab, R, and C

Publications

Passey BH, **Hu H**, Ji H, Montanari S, Li S, Henkes GA, Levin N, 2014. Triple oxygen isotopes in biogenic and sedimentary carbonates. *Geochimica et Cosmochimica Acta.* 141, 1-25.

Yang YZ, Long Q, **Hu HT**, Hieu PT, Nguyen TBT and Chen FK. 2013. Geochemical characteristics and origin of lamprophyre in the Laichau area, northwestern Vietnam. *Acta Petrologica Sinica*, 29 (3): 899-911

Publications – *in preparation*

Hu H, Passey BH, Lehmann SB, Levin NE, Johnson BJ, (*to be submitted to GCA, 2016*). Modeling and interpreting triple oxygen isotope variations in animal body water.

Hu H, Passey BH, Chin K, Wang Q, Montanari S, Pérez-Huertaa A, Wang XL, (*in prep*). Mesozoic carbon cycling reconstructions using triple oxygen isotope compositions of dinosaurian eggshell carbonates.

Hu H, Passey BH, (*in prep*). Triple oxygen isotope equilibrium fractionation of CO_2-H_2O system.

Presentations – *first author only*

Hu H, Passey BH, Lehmann SB, Levin NE, Montanari S, Chin K, Johnson BJ, Wang Q, Wang XL, 2015. Triple oxygen isotopes and clumped isotopes in modern vertebrate and dinosaur biominerals: Records of paleoecology, paleoaridity, and paleo-carbon-cycling. *Annual Meeting of the American Geophysical Union, San Francisco CA, December 2015.*

Hu H, Passey BH, Montanari S, Chin K, 2014. Constraints on Late Jurassic and Cretaceous atmospheric pCO_2 and primary productivity using animal body water model and triple oxygen isotopes in dinosaur eggshells. *Geological Society of America Annual Meeting, Baltimore, Maryland, USA, November 2015.*

Hu H, Passey BH, Montanari S, Naomi NE, Li S, 2013. A deep-time CO_2 barometer based on triple oxygen isotope compositions of dinosaurian eggshell carbonate. *Annual Meeting of the American Geophysical Union, San Francisco CA, December 2013.*